Integrated Battery Charger Topologies for Traction Inverters in Electrified Vehicles

INTEGRATED BATTERY CHARGER TOPOLOGIES FOR TRACTION INVERTERS IN ELECTRIFIED VEHICLES

BY

JOHN REIMERS, B.Eng.

A THESIS

SUBMITTED TO THE DEPARTMENT OF ELECTRICAL & COMPUTER ENGINEERING

AND THE SCHOOL OF GRADUATE STUDIES

OF MCMASTER UNIVERSITY

IN PARTIAL FULFILLMENT OF THE REQUIREMENTS

FOR THE DEGREE OF

DOCTOR OF PHILOSOPHY

Doctor of Philosophy (2020) McMaster University

(Electrical & Computer Engineering) Hamilton, Ontario, Canada

TITLE:	Integrated Battery Charger Topologies for Traction Inverters in Electrified Vehicles
AUTHOR:	John Reimers B.Eng., Electrical Engineering McMaster University, Hamilton, Canada
SUPERVISOR:	Dr. Ali Emadi
NUMBER OF PAGES:	xxi, 214

Abstract

Electric vehicles today include several power electronics modules which are critical to their operation. The traction inverter converts direct current from the battery pack into alternating current suitable for powering the electric motor, allowing the vehicle to drive. When the vehicle is parked, the onboard charger enables conversion of alternating current from a standard outlet to direct current suitable for charging the battery pack. The traction inverter and onboard charger typically represent the majority of the power electronics cost, weight and volume in an electric vehicle. The temporal exclusivity and functional similarities of the inverter and charger present a basis for investigating how they may be combined into a single system which can achieve both functions. To that end, a novel approach to developing integrated traction inverter and battery charging systems, along with subsequent implementations, is considered.

To establish context for the development of integrated battery chargers, a detailed review of traction inverters is conducted, including analysis of inverters from several production electric vehicles. Future trends are identified including the need for further increases in power density and the potential impact new machine types like switched reluctance motors may have on the traction inverter implementation. Additionally,

preliminary efforts by manufacturers to integrate the vehicle power electronics at a mechanical level are discussed and analyzed. Based on these trends, integration of the traction inverter and onboard battery charger at the electrical level is considered as a means to increase power density at the system level, while reducing cost and improving functionality.

A conceptual foundation for integrated converter topologies is proposed. Based on the idea of a fundamental three-terminal cell, a traction inverter can be decomposed and reconfigured to achieve additional converter functionality. The electric machine may also be included in the reconfigured converter, functioning as an inductor. A decoupled model for a conventional interior permanent magnet synchronous machine is developed to facilitate design of the converter and predict torque production during operation.

In view of switched reluctance machines being a promising candidate for future traction applications, a new integrated charger topology for powertrains with switched reluctance motors is proposed. Charging is achieved from a three-phase grid at significantly higher power levels than a conventional OBC. Similar to the conventional permanent magnet machine, a model for the machine in the charging mode is developed from electromagnetic finite element analysis. Simulations of the converter and machine in the charging and driving modes demonstrate the converter operation.

For powertrains with conventional three-phase machines, a second new integrated charger topology is proposed based on a traction inverter constructed with multiple semiconductor switches in parallel per phase leg. The integrated converter can operate as a universal battery charger, charging from single-phase alternating current or direct current sources at any voltage within the converter component ratings. The

charging control strategies are presented and the converter operation is experimentally validated. Additionally, vehicle-to-grid capability is demonstrated, as an example of the functionality benefits of integrated chargers. Finally, practical implementation challenges are addressed and an analysis of the cost benefits of the proposed integrated converter presented.

Acknowledgements

I would first like to thank my supervisor, Dr. Ali Emadi, for his guidance, trust and support throughout my time at the McMaster Automotive Resource Center (MARC) during my undergraduate and graduate studies. I will be continually grateful to him for providing so many opportunities for me to lead and contribute to a variety of projects that expanded well beyond my dissertation research, enabling me to gain far more than just a degree. I would also like to thank Dr. Mehdi Narimani and Dr. Yinye Yang for their helpful suggestions and comments on my research work over the years.

I would like to thank all of my colleagues at MARC for their friendship, assistance, enthusiasm and interesting discussions, especially Jack Gillies, Maryam Alizadeh, Niloufar Keshmiri and Dr. Phil Kollmeyer. Special thanks to Mr. Cam Fisher for access to his machine shop facilities and his patience with our experimental setups on his dynamometers. I would also like to thank all the members of the McMaster Engineering EcoCAR 3 team, especially Mackenzie Wootton, Federico Duperly, Alex Lao, Alison Bayzat, Tyler Stiene, William Long, and the many other team members who contributed to that exceptionally ambitious project.

Finally I would like to thank my parents for inspiring my interest in science and engineering from a young age. In particular I owe my interest in electric vehicles to my father Dr. Jan Reimers, who encouraged my curiosity in electronics and provided Li-ion cells for the various projects we built together.

Nomenclature

Abbreviations

APM	Auxiliary Power Module
BEV	Battery Electric Vehicle
CM	Common Mode
EMI	Electromagnetic Interference
EV	Electric Vehicle
EVSE	Electric Vehicle Supply Equipment
GHG	Green House Gas
HEV	Hybrid Electric Vehicle
IBC	Integrated Battery Charger
ICE	Internal Combustion Engine

IGBT	Insulated Gate Bipolar Transistor
IPMSM	Interior Permanent Magnet Synchronous Machine
OBC	Onboard Charger
OSG	Orthogonal Signal Generator
PFC	Power Factor Correction
PHEV	Plug-in Hybrid Electric Vehicle
PI	Proportional Integral
PLL	Phase Locked Loop
PM	Permanent Magnet
PMSM	Permanent Magnet Synchronous Machine
PWM	Pulse Width Modulation
SOGI	Second Order Generalized Integrator
SPDT	Single Pole Double Throw
SR	Switched Reluctance
SRM	Switched Reluctance Machine
SVPWM	Space Vector Pulse Width Modulation
THD	Total Harmonic Distortion

V2G	Vehicle To Grid
VSI	Voltage Source Inverter
WBG	Wide Bandgap

Symbols

B	Magnetic flux density
C_{dc}	DC link capacitance
d	Duty cycle
f_g	Grid frequency
f_s	Switching frequency
$\mathfrak{F}$	Magnetomotive force
I_{cm}	Common mode current
$I_{L_{ac},rms}$	PFC inductor rms current
$I_{L_a,avg}$	Phase A average current
λ	Magnetic flux linkage
η	Boost ratio V_o/V_i
ω	Rotational frequency

ϕ	Stator angle relative to phase A axis
ψ_f	Permanent magnet flux
$\mathfrak{R}$	Magnetic reluctance
τ	Torque
θ	Rotor angle
θ_g	Grid voltage phase angle
V_{batt}	Battery voltage
V_{dc}	DC link voltage
V_i	Converter input voltage
V_o	Converter output voltage
v_{pwm}	PWM rectifier input voltage
χ	Saliency ratio L_q/L_d

Contents

List of Tables

List of Figures

Chapter 1

Introduction

1.1 Motivation

The automotive industry is currently experiencing a period of change larger than any it has seen since its inception over 100 years ago. Numerous paradigm shifts are occurring spanning all aspects of the automobile from the powertrain to the driver. Rapid advances in technology have enabled the beginnings of a new era of connected, autonomous and electrified vehicles. The primary motivation for transportation electrification has been to reduce greenhouse gas (GHG) emissions, since transportation accounts for approximately one quarter of global CO_2 emissions [1].

Emissions of GHGs into the atmosphere, primarily caused by burning of fossil fuels, has led to a warming of global average temperatures due to the greenhouse effect. GHGs like CO_2 and methane in the atmosphere reflect radiated heat energy back to the Earth's surface, preventing it from being dissipated into space and resulting in

further heating. The greenhouse effect is critical for sustaining life on Earth, however the significant increase in GHG emissions by humans over the last 200 years has begun to increase the intensity of the effect far beyond natural levels. In 2013, the global atmospheric concentration of CO_2 reached 400 ppm, significantly exceeding the 300 ppm maximum observed from 800 000 years of ice core data. Ongoing global warming will have drastic future consequences as polar ice caps continue to melt resulting in sea level rise, along with increased occurrences of extreme weather and other destructive phenomena [2].

It is therefore imperative that coordinated action be taken to reduce global GHG emissions. Studies have attempted to predict the future economic costs of climate change if no action is taken. By 2100 the estimated annual cost of climate change related impact in the United States alone is $1.9 trillion per year [3]. Unfortunately it has been challenging to enact durable policies that will be able to eliminate or reduce the potentially catastrophic long term costs by incurring far more moderate near term costs that reflect the unpriced externalities of GHG emissions. While effective climate policy will inevitably be required to solve what is arguably humanity's largest existential threat, technological advances still have the potential to make an immediate impact in spite of the disadvantaged economics imposed by a lack of policy.

Modern electric vehicles (EVs) are one such technology that shows significant promise in terms of potential impact on GHG emissions. In 2019, EVs made up only 1% of all vehicles world wide, however their marketshare has expanded at an average rate of 60% per year since 2014. This brings the total world wide EV fleet to approximately 7.2 million vehicles, a several order of magnitude improvement over the only 17 000 EVs on the road in 2010. These 7.2 million EVs resulted in less than half the amount

of CO_2 emissions when compared to an equivalent internal combustion engine (ICE) fleet of vehicles, including the emissions from electricity generation for charging [1]. This number will continue to improve as electricity generation improves, eventually reaching near zero with a grid powered by renewable sources.

Even with a grid powered by non-renewable or GHG emitting generation, EVs have effectively decoupled the energy source from the vehicle. This allows shifting the tail pipe emissions of individual ICE vehicles to the point of electricity generation. In addition to GHGs, tailpipe emissions contain particulates which have been shown to have adverse effects on human health when present in sufficient concentrations [4]. EVs therefore offer the immediate benefit of reducing particulate matter in populated areas, even considering the increased demand on the electrical generation system which may still emit particulates [5].

While EV market penetration is expanding, barriers remain that will prevent truly widespread adoption across all market segments. Primarily, EVs with comparable range to conventional ICE vehicles have been higher cost than an equivalent ICE vehicle. This is beginning to change in recent years with the introduction of lower cost, longer range EVs like the Chevy Bolt and Tesla Model 3. The cost of these vehicles is primarily driven by the large lithium ion (Li-ion) battery packs required to achieve the range demanded by consumers. Battery costs have been falling steadily over the last decade, with the US Department of Energy (DOE) estimating a pack level cost of \$125/kWh is required for EVs to be cost competitive with ICE vehicles [6].

A second challenge is the availability of EV charging infrastructure. DC fast chargers have begun to proliferate, with the number of publicly accessible DC fast charging stations nearly doubling to 263,000 between 2018 and 2019 [1]. However, data has

shown that 95% of vehicle trips are shorter than 30 miles [7], making recharging at home a viable solution for the vast majority of trips. Charging at home is typically done overnight with a standard AC wall outlet supply. For this reason, EVs will continue to support low power AC charging, even as high power fast charger infrastructure continues to expand.

To further accelerate the widespread adoption of EVs, it is important to take a system level approach to reducing the vehicle cost, considering the entire powertrain. To convert DC from the battery to suitable three-phase AC for the electric motor, a traction inverter is required. The efficiency of the traction inverter and electric motor has a direct effect on the size of the battery pack required to achieve a given range. Therefore at a system level, moderately increasing the cost of the inverter or motor to achieve higher efficiency may result in an overall lower system cost, as the size of the battery pack can be reduced. In addition to the DC/AC conversion capability of the traction inverter, EVs require an onboard charger (OBC) capable of AC/DC conversion to allowing battery charging from a standard AC grid supply [8]. Reducing the mass of any of these components can further the lightweighting efforts already being undertaken by many automotive manufacturers, again allowing the size of the battery pack to be reduced for a given range. Reducing the volume is also beneficial as it allows more flexibility in packaging and generally reduces the raw material required to manufacture the components, therefore reducing the cost.

Extending this system level optimization approach to the implementation of each powertrain component leads to further opportunities for cost, weight and size reductions. Identifying commonality between different system components leads to the concept of integration, in which distinct components can be combined into one unit with shared

parts. Integration has the potential to provide significant cost savings, both directly in terms of the integrated components, and at the system level through volume and weight reductions.

A promising candidate for integration is the traction inverter and OBC. At a conceptual level they perform similar electrical functions, namely DC to AC conversion and AC to DC conversion. The potential for integration has been recognized for some time [9], but has had limited success in moving beyond the research stage to commercial implementations. In many cases, this is due to the complexity of the proposed solutions, requiring major changes to the entire powertrain, thus introducing a level of risk not palatable by vehicle manufacturers. In other cases, the integrated solutions are only applicable to specific powertrain designs, such as those that include high power DC/DC converters or multiple electric motors. Therefore there is a need for additional research into solutions that can be integrated with relatively little impact on the powertrain.

This thesis focuses on the development of new electrically integrated traction inverter and OBC topologies which attempt to maximize the benefits of integration while remaining practical for conventional automotive applications. This is achieved through limiting modifications required to achieve OBC functionality to the traction inverter, leaving the remainder of the powertrain untouched. A review of production traction inverters is conducted to establish the current state of the art and provide a basis for the development of new integrated designs. A theoretical foundation for integration is established, which is used to develop two distinct new integrated topologies. Battery charging is achieved from standard AC grid supplies using a minimum number of additional components added to the traction inverter only, and no modifications to the electric machine. Consequently, the conventional OBC can be eliminated, as the

functionality is now integrated into the traction inverter. The objective of this thesis is to provide the context, conceptual development, and validation of the proposed integrated topologies.

1.2 Contributions & Publications

- A review of current state of the art automotive traction inverter designs from various manufacturers, including primary analysis of previously unpublished inverter hardware. Future trends in traction inverter design are identified and discussed. Published in [10]. The CAD models in Figures 2.2, 2.3, 2.4 and 2.6 were created by co-author C. Mak.

- Establishment of a theoretical basis for integrated converters, including modelling of electric machines in integrated converters.

- Development of a new integrated battery charger for switched reluctance machine based powertrains, capable of three-phase charging. Published in [11].

- Development and experimental validation of a new integrated battery charger for permanent magnet motor based powertrains, capable of single-phase charging. Submitted to IEEE Open Journal of Power Electronics.

1.3 Thesis Outline

The thesis is organized into seven chapters.

Chapter 1 provides the motivation for the development of integrated solutions in EVs. A need is identified for additional research into integrated solutions that impact only the traction inverter design without making any impositions on the remainder of the powertrain components.

Chapter 2 conducts a review of the state-of-the-art traction inverter designs from several production vehicles across multiple manufacturers. Future trends in inverter design are identified based on industry examples and academic research. Wide bandgap (WBG) devices and trends in device packaging are discussed along with active gate driver implementations, current and future trends in system integration, and advanced manufacturing techniques.

Chapter 3 expands upon some of the identified future trends in traction inverters with the goal of providing motivation for the remaining chapters. Fundamental limits of power density for converters are identified and discussed. The impact of promising alternative machine types for traction applications, particularly switched reluctance machines (SRMs), is presented in the context of the inverter design. Electrical integration of the traction inverter and OBC is proposed and some practical implementation challenges are identified. An analysis of the cost benefits of mechanical integration of a production OBC with the traction inverter is conducted. A literature review of existing integrated topologies is presented.

Chapter 4 develops theoretical concepts relevant to the derivation and analysis of integrated converter topologies. The technical foundations of integrated charging functionality are developed starting from a high level and expanding into the synthesis of integrated converters from fundamental converter cells. While the low level operation of the power devices are essentially unchanged regardless of integrated charging, the

role of the electric machine changes significantly. To predict the machine behaviour when used for integrated charging functionality, a decoupled model for an interior permanent magnet synchronous machine (IPMSM) is developed from first principles.

Chapter 5 presents a new integrated charger topology for SRMs, capable of charging from a three-phase grid. Torque production during charging is analyzed, and a control strategy presented for power factor corrected (PFC) charging operation.

Chapter 6 presents a new integrated charger topology for conventional three-phase machines, capable of charging from a single-phase grid or DC source at any voltage. Using the IPMSM machine model from Chapter 4, torque production during charging is analyzed and rotor positions where zero torque is produced are identified. A control strategy is presented for single-phase power factor corrected charging operation and DC/DC converter operation. Experimental results validate the proposed topology with a production EV traction motor.

Chapter 7 presents conclusions and future work.

Chapter 2

Automotive Traction Inverters

2.1 Introduction

EVs are continuing to show promise as more manufacturers announce plans to develop electrified models in order to improve fuel economy and remain competitive as consumer demands shift towards efficient, cleaner vehicles. These include hybrid electric vehicles (HEVs), plug-in hybrid electric vehicles (PHEVs), and battery electric vehicles (BEVs). At the heart of all electrified powertrains is one or more electric motors which operate either in conjunction with an ICE or replace it entirely. The electric motors found in EVs today are most commonly of the AC permanent magnet (PM) or AC induction machine type [8, 12]. To drive them, a traction inverter is required to convert the direct current available from the battery pack to variable frequency alternating current. In addition to the motoring mode, the machines can also operate as generators, requiring the inverter to act as a rectifier and return energy to the battery.

While previous reviews have either covered the entire electrified powertrain [13] or focused on theoretical aspects of the inverter [14], the goal of this chapter is to present a thorough review of the production inverter implementations across several vehicle manufacturers. In the following, a review of current production automotive traction inverters with a focus on BEVs and PHEVs is presented. BEVs and PHEVs tend to have higher power inverters and, as the industry trends towards fully electric powertrains, the majority of traction inverters in the future will be in the 100-500 kW range compared to the 30-60 kW range found in HEVs today. Finally, future trends are identified based on ongoing research and emerging industry practices.

2.2 Inverter Design

2.2.1 Topology

The vast majority of production EVs today utilize the three-phase voltage source inverter (VSI) topology shown in Figure 2.1. In traction applications, the VSI is typically implemented with insulated gate bipolar transistors (IGBTs) due to their high current and voltage capabilities. The VSI offers relatively simple, low cost implementation and control and has been used extensively for motor drive and grid connected applications alike for decades.

While the VSI is undoubtedly the dominant topology, alternatives have been proposed including the current source inverter (CSI) [15] and Z-source inverter (ZSI) [16]. The CSI can produce an AC output at a higher voltage than the input voltage, which can eliminate the need for a high power DC/DC converter in some powertrains. The DC

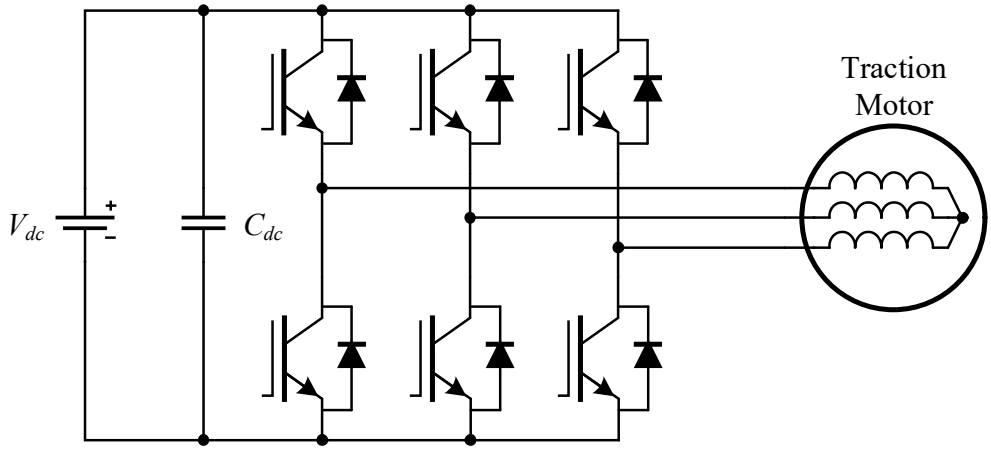

Figure 2.1: Three-phase VSI topology.

link capacitor can be reduced, however it is replaced with a DC link inductor which is typically larger and heavier. Additionally, the need for reverse blocking switches in practice usually requires series diodes with each IGBT switch, reducing the efficiency [17]. The ZSI combines characteristics of both the VSI and CSI, however the cost and volume of the required passive components over the VSI generally make it less attractive for automotive applications.

Multi-level converters are also of interest for traction inverter applications. In particular the three level neutral point clamped (NPC) and T-type NPC (TNPC) [18–20]. Multi-level converters have the benefit of multi-level voltage output, which can reduce phase current ripple or reduce the effective converter switching frequency, potentially improving efficiency. Unfortunately they require significantly more switching devices than a two level VSI, and the voltage levels for typical EV battery packs do not necessitate their higher voltage capabilities achieved by the series connection of the switching devices. Therefore the two level VSI remains the dominant choice today, though multi-level topologies may begin to see adoption as DC link voltages increase.

2.2.2 Modulation Techniques

Pulse width modulation (PWM) techniques are applied to synthesize the inverter's AC output from a DC input. The power semiconductors in the inverter are switched in a specified pattern based on feedback from current sensors measuring the phase currents.

Several well known modulation techniques for VSIs exist, including sinusoidal pulse width modulation (SPWM), space vector pulse width modulation (SVPWM) and Six-step modulation. Further techniques like discontinuous pulse width modulation (DPWM) and selective harmonic elimination PWM (SHEPWM) are also used in certain applications, though tradeoffs often exist in terms of harmonic content and efficiency. Indeed the switching action of the semiconductors produces a voltage waveform that has a sinusoidal fundamental component, but also significant harmonic content around the switching frequency. When applied to an inductive load like a motor, this results in current ripple which contribute to losses in the motor and can produce torque ripple [21]. These harmonics can also cause acoustic noise which is particularly undesirable in consumer automotive applications [22, 23]. Therefore proper selection of PWM techniques is a critical part of the inverter design process.

Sinusoidal PWM (SPWM)

SPWM is one of the simplest modulation techniques and has widely applied in industry [21] as it can be implemented with only analog electronics or low cost digital processors. For a given DC link voltage V_{dc}, the maximum amplitude of the fundamental phase

voltage is $V_{dc}/2$, resulting in a maximum fundamental line-to-line rms voltage of

$$V_{ll_1,max} = \frac{\sqrt{3}}{2\sqrt{2}} V_{dc} \approx 0.612 V_{dc} \tag{2.1}$$

Space Vector PWM (SVPWM)

The advent of low cost digital control has enabled SVPWM to achieve widespread popularity [21, 24]. Though slightly more complex in implementation than SPWM, the maximum fundamental phase voltage amplitude is increased to $V_{dc}/\sqrt{3}$, or about 15% higher than SPWM, while also maintaing lower total harmonic distortion (THD) [25, 26]. The maximum fundamental line-to-line rms voltage is therefore

$$V_{ll_1,max} = \frac{1}{\sqrt{2}} V_{dc} \approx 0.707 V_{dc} \tag{2.2}$$

The improved DC link utilization of SVPWM can be further extended with over modulation, eventually reaching six-step modulation. Though it is challenging to confirm which modulation strategy is used for the traction inverters in every EV, it is believed that SVPWM is preferred due to its performance superiority. For example, it has been reported in [27, 28] that General Motors (GM) employs SVPWM for the linear modulation region and then transitions to six-step overmodulation.

Six-step Modulation

The six-step mode, also known as square-wave modulation, is named after the six distinct steps the output phase voltages take over a fundamental cycle [29]. In the

six-step mode, the DC link voltage fundamental amplitude of the phase voltage is equal to $\frac{4}{\pi}V_{dc}$. The resultant fundamental line-to-line rms voltage is therefore fixed at

$$V_{ll_1} = \frac{2\sqrt{6}}{\pi}V_{dc} \approx 1.56V_{dc} \tag{2.3}$$

This increases the torque capability in the flux-weakening region, however this method raises some practical issues due to low-order current harmonics that make control of the torque challenging. The six-step modulation remains a complementary method combined with another PWM technique due to its lack of output voltage amplitude control.

2.2.3 Inverter Components

The power semiconductor devices are the central component of an inverter. IGBTs have been the device of choice since they began to replace bipolar junction transistors (BJTs) for high voltage and high current applications in the late 1980s [30]. EVs today typically operate with up to 400V DC links, making 650V rated IGBTs more than sufficient. Advanced power modules have been developed by several manufacturers which provide all six required IGBTs and antiparallel diodes in a single package, supporting inverters up to several hundred kilowatts. Discrete IGBT devices can also be connected in parallel to achieve higher current capabilities.

To effectively switch the power semiconductor devices, gate drivers are required. The gate driver has an influence on the overall inverter efficiency, as it determines the dynamic behaviour of the IGBTs during switching. The gate driver provides isolation between the control inputs and the power device gate, while also providing feedback

to the controller and detecting short circuit conditions [31].

A voltage source inverter, like any switching converter, processes power by semiconductor switching action. This inherently results in a discontinuous current waveform at the input of the converter. The DC link capacitor serves to provide a low impedance path for the high frequency current components which has two significant benefits:

1. Low pass filtering of the current the DC link must supply
2. Decoupling of DC link impedance, which is typically inductive, from the power modules

(1) is important for the overall system, as it reduces the rms current the DC link must supply, for the same average current. Additionally, depending on the DC link impedance, any current ripple can be converted into voltage ripple, which can have adverse effects on other components on the DC bus. (2) is important for protection of the inverter itself. As the switching action generates high di/dt, any inductance on the DC link, such as that created by long cables, will be converted to a voltage. During device turn-off (negative di/dt), this voltage is added on top of the DC link voltage. Should that voltage rise above the voltage rating of the semiconductor switches, catastrophic failure can result. From the perspective of the power switch, the DC link capacitor serves to provide a capacitive impedance which maintains stable voltage. Parasitic inductance in the interconnects between the power switches and the capacitors may still exist, but this can be controlled by the inverter designer through proper busbar design techniques.

To implement the motor control software, a microcontroller or DSP is included, typically on a dedicated control board within the inverter. Given the computational

requirements of the motor control and modulation schemes, 32-bit floating-point processors clocked at over 100 MHz are the norm for traction inverters. As control algorithms continue to increase in complexity and switching speeds rise, it has been suggested that field programmable gate array (FPGA) hardware be used to implement the modulation while the DSP handles the motor control, in order to improve timing accuracy and reduce the DSP requirements [32, 33]. A position sensor is typically used to determine the rotor angle of the electric machine. Many automotive applications use a resolver and a dedicated resolver-to-digital (R2D) chip is included on the inverter control board to provide the necessary excitation signals as well as the analog to digital conversion of the resolver signal.

Current sensors are used to measure the inverter's AC ouput current, which is fed back to the DSP which implements the closed loop control. For automotive applications, open loop Hall effect sensors are typically applied due to their relatively low cost, high bandwidth and inherent isolation.

Thermal management is critical to maintaining suitable operating temperatures for the power semiconductors which must dissipate up to several kilowatts in losses. Indeed, temperature has been identified as the primary source of failure in power converters [34, 35]. In traction inverters, thermal management is typically implemented with a liquid cooled heatsink which is placed directly under the power semiconductors.

Traction inverters are often required to supply hundreds of amps to the electric motor, and therefore require copper busbars to conduct the current efficiently. Busbars are typically used to connect the DC input to the DC link capacitors and the power devices, as well as the phase outputs to the motor phase cable connector, passing through the current sensors. On the DC side, a planar structure is adopted to minimize the

parasitic inductance [36].

2.3 Current Status

Numerous OEMs now offer electrified or fully electric models. Information on the implementations of the inverters for these vehicles is either published in technical papers by the manufacturers and their suppliers, or it is obtained through reverse engineering by private or governmental organizations. The rated power and power densities of the reviewed traction inverter implementations are summarized in Table 2.1.

2.3.1 General Motors (GM)

GM has had a long history of electrification, beginning with the EV1 in 1996. Their first generation traction inverter featured a power density of 3 kW/L [13]. Today they offer several electrified models and have published technical papers on some of the inverter designs with their Tier 1 supplier Delphi Technologies.

Chevrolet MY2016 Volt

The 2016 model year Chevrolet Volt marks the second generation of GM's first production PHEV. The traction inverter is described in detail in [37] and [38]. The inverter features dual VSIs for the traction and generator machines with power ratings of 87 kW and 48 kW respectively, as well as a smaller VSI to drive the variable speed

oil pump for the ICE. The maximum DC link voltage is 430 V and the maximum total simultaneous AC power for both inverters is reported as 180 kVA with a power density of 17.3 kVA/L. While the first generation Volt inverter was situated separately in the engine bay, the second generation is located directly on the transmission manifold to eliminate the need for phase cables. This tighter integration of the inverter with the powertrain reduces component count, harness complexity and assembly cost while improving collision robustness.

The overall layout of the inverter is shown in Fig. 2.2. The double-sided cooling (DSC) IGBT power module developed by Delphi Technologies is used for both the motor and generator inverters. Wire bonds were eliminated in favor of solderable interconnects to improve reliability and reduce inductance. The coefficient of thermal expansion (CTE) of the ceramic substrates was matched to that of the silicon to further increase reliability. The twelve modules are soldered in two rows of six to a power PCB which is connected to the DC link from above in the center. The AC output bus bar assembly connects from below to the edges of the PCB. The DC link capacitor sits below the AC bus bar and connects upwards in the center to the DC link on the power board.

Cooling of the IGBT modules is achieved with copper metal injected molded heat sinks. With the elimination of phase cables, the AC output bus bars are now connected directly to the electric machines which offers a direct path for heat flow from the electric machine windings to the inverter power modules. An additional cooling mechanism consisting of an electrically insulated thermal interface material and stamped aluminum sheet was required to divert heat flow from the bus bars to the inverter housing.

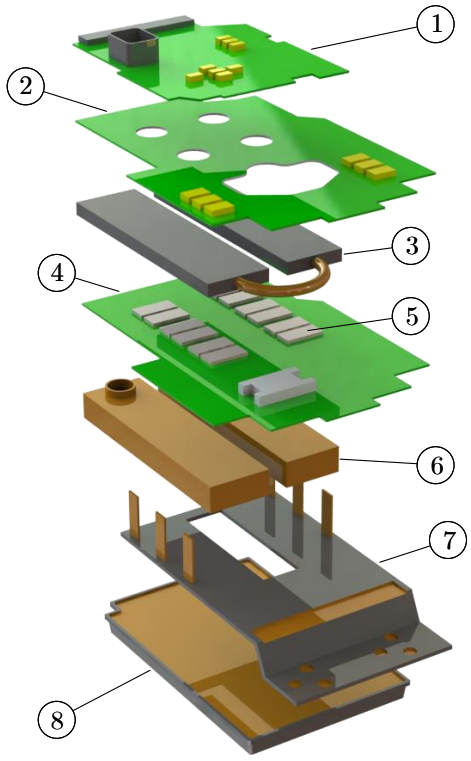

Figure 2.2: Second generation Chevrolet Volt inverter components: 1. Control board 2. Gate driver board 3. Top heat sink 4. Power board 5. DSC IGBT modules 6. Bottom heat sink 7. Phase busbars 8. DC link capacitor.

Cadillac MY2016 CT6

The Cadillac CT6 PHEV builds upon the Volt powertrain design to meet the higher performance requirements of a luxury rear wheel drive application. The traction inverter is described in [39] and [40], again featuring dual VSIs for the motor and generator, and a third smaller VSI for the engine oil pump. Despite the identical topology, the implementation is somewhat different from the Volt. AC phase cables to the motors remain, likely for packaging reasons given the larger ICE and longitudinal orientation of the hybrid transmission.

The power switches are phase leg modules developed by Hitachi which feature direct cooling. The module packaging eliminates any thermal grease, with water ethylene glycol (WEG) coolant passing directly over both sides of the module. An aluminum pin fin plate is attached to each side of the die with an electrically insulating sheet allowing the module to be immersed in coolant, resulting in a reported 35% reduction in thermal impedance from junction to coolant. The modules are directly connected via bus bars to the DC link capacitor, which is also liquid cooled. The increased efficiency and reduced thermal impedance of the IGBT modules enable a compact design which was required to meet the packaging constraints for the large hybrid powertrain.

2.3.2 Toyota MY2016 Prius

Toyota has long been at the forefront of mass market HEVs since the introduction of the Prius in 1997. They continue to focus on hybrid models with some expansion in to PHEVs with the Prius Prime in 2012. Significant reverse engineering efforts have been undertaken by Oak Ridge National Laboratory (ORNL) on the 2004 and 2010 model year Prius [41]. Toyota has also published technical papers on the development of the Prius inverter, most recently for the fourth generation model [42].

The fourth generation Prius was launched in North America in early 2016. Toyota has integrated two VSIs, a DC/DC boost converter, and a DC/DC buck converter for the auxiliary power module (APM) into one unit. The inverter housing is mounted to the transaxle to eliminate external phase cables and improve collision robustness. Due to the mounting location, additional considerations for vibration resistance were required,

including rubber mounting bushings, elastic washer PCB mounting, and vibration simulations during the design of the signal interconnects.

The module and heat exchanger stack are shown in Fig. 2.3. The power module, manufactured in house by Toyota, is a phase leg "power card" format. The modules are resin molded with an integral heat exchanger allowing DSC. In total, seven phase leg modules, including their individual heat exchangers, are stacked to form the two VSIs and the DC/DC boost converter. The major benefit of the card format is simplified scalability of the inverter for different powertrain applications through paralleling of module. Interestingly the fourth generation module reintroduces thermal grease between the IGBT and heat exchanger, which had previously been eliminated in the third generation power module design. The additional heat flux from more tightly integrating the power switches is mitigated through the increased surface area of the DSC.

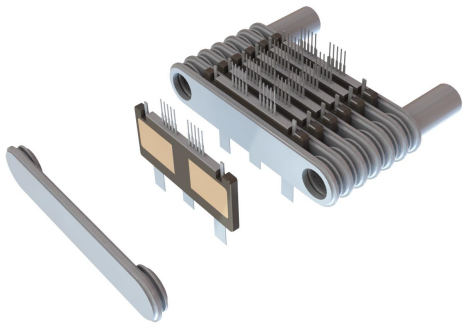

Figure 2.3: Toyota "power card" DSC IGBT module stack with heat exchanger.

Improved power density has been achieved through the tight integration of many inverter components. The DC link capacitor assembly for the inverters was designed to be connected directly to the power modules, eliminating the need for an additional busbar. The required capacitance was reduced thanks to improved control of the DC/DC boost converter while further reducing volume with new thinner polypropylene

(PP) films. Snubber circuits, commonly used to limit the surge voltage across the switches, were eliminated through reducing stray inductance in the capacitors, busbars, and power modules. The phase current sensors have been integrated into the AC output terminals, relying on a Hall effect sensors that have been integrated into an IC package, reducing part count and simplifying assembly. Further size reductions were achieved by combining all control and gate drive circuitry onto a single PCB. Fastener count was reduced by 67% by transitioning to welded joins while simultaneously reducing fastener diameters to save space and weight.

2.3.3 Nissan MY2012 LEAF

The Nissan LEAF was first introduced in 2010 with a 24 kWh battery pack as Nissan's first mass market BEV. The MY2010 LEAF inverter and electric machine designs were documented by Nissan in a technical paper [43]. ORNL has conducted a teardown of the MY2012 LEAF inverter in [44] and the National Renewable Energy Laboratory (NREL) has published a performance evaluation of the thermal systems in [45].

The Nissan LEAF inverter is a single VSI powering the vehicle's one electric motor. The inverter is situated directly on top of the motor, eliminating external phase cables. As the vehicle has only a single electric motor and no ICE, packaging size of the inverter did not appear to be a significant priority in the design, thus the power density is somewhat low.

To achieve the required 340 A rms continuous current rating, three IGBTs and diodes are paralleled internally per switch with two switches forming a phase leg power module. A separate power module is used for each phase. The power module has

a unique layer stack up in which the IGBT is soldered to an electrically conducting copper base plate with an intermediate copper molybdenum alloy buffer plate. The buffer material reduces stress caused by the CTE mismatch between the semiconductor and the copper plate. The copper plate is then bolted to the cooling plate with an electrically insulating thermal interface material. The gate drive circuitry includes dV/dt feedback through an analog differentiator coupled to the IGBT collector. During turn off events, the feedback controls the gate drive discharge to limit the turn off speed, reducing surge voltage.

The overall inverter layout is shown in Fig. 2.4. The DC link capacitor is a large planar structure with DC terminals for each of the three power modules and an integrated thermistor, manufactured by Panasonic. Three hall effect current sensors are integrated with the AC bus bar assembly. The gate driver board is located on top of the power modules while the control board is located above the DC link capacitor. The cooling plate below the power modules has serpentine cooling channels for WEG coolant. The bottom cover is bolted with a gasket for sealing.

2.3.4 BMW MY2016 i3

The i3 is BMW's first mass produced zero emissions vehicle featuring either a 22kWh or 33kWh Lithium-ion battery and a 125 kW PM motor. ORNL has conducted a benchmarking assessment of the inverter and electric machine [46].

The inverter unit also contains an APM and a 3.7 kW battery charger and the overall unit weighs 19 kg. Again external phase cables have been eliminated by directly mounting the inverter on top of the electric machine. The power stage is an Infineon

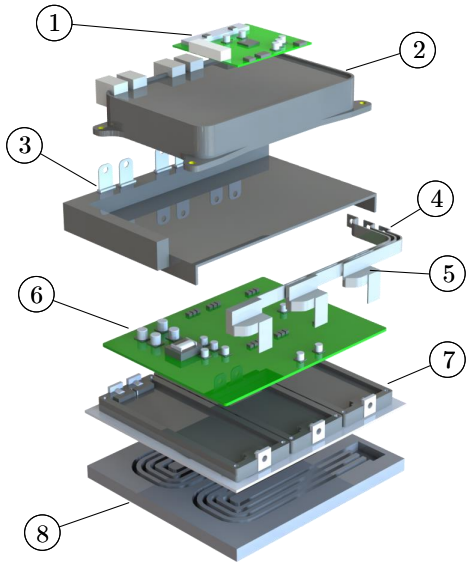

Figure 2.4: Nissan LEAF inverter components: 1. Control board 2. DC link capacitor 3. DC link busbar 4. Phase busbars 5. Current sensor 6. Gate driver board 7. IGBT power modules 8. Serpentine heat sink.

sixpack IGBT module which has a rated nominal collector current of 800A. The control board contains two DSPs as well as a complex programmable logic device (CPLD). The gate driver board also houses the three 700A LEM Hall effect current sensors for the phase outputs.

Mechanically, the inverter assembly is stacked with the DC link capacitor on the bottom, followed by a cold plate on which the IGBT module is mounted. The gate driver board is mounted to the IGBT module and the control board is on top of the entire assembly. Since the control board also handles the charger and APM, it is much larger than the inverter stack and extends over much of the internal area.

2.3.5 Audi MY2016 A3 e-Tron

Volkswagen (VW) group recently released its new electrification project, named 'Roadmap E', for 2025 and its strategic approach seems to move towards more PHEVs and BEVs [47]. So far, the brands Audi, VW and Porsche have developed a dozen versions of their models with some degree of electrification. The VW group aims to massively expand its electrified portfolio across all brands and models by 2030.

Audi introduced in 2016 its new A3 e-Tron PHEV with a battery pack of 8.8 kWh allowing for an all-electric range of about 17 miles. In this parallel hybrid powertrain, a single 75 kW electric machine is combined with an ICE and the system delivers up to 152 kW and 350 N.m of torque.

In [48], the inverter module, manufactured by Bosch, is described. In order to maximize the packaging, the traction inverter and APM are integrated in the same enclosure and share a liquid cooled heat sink. The cooling plate is die cast as two aluminium pieces and then assembled via friction stir welding (FSW). The overall inverter module weight is estimated at 10 kg with a volume of about 8 L. Three IGBT half-bridge modules from Bosch are used in the traction inverter with voltage and current ratings of 600V and 300A respectively. The control board is composed of, amongst others, a processor, a microcontroller, and current sensor ICs, while the IGBT control board includes the gate drivers. The internal housing provides electromagnetic interference (EMI) shielding for the control board. Finally, a large DC link metalized PP film capacitor is connected to the DC bus bar.

2.3.6 Tesla Model S

In 2012, Tesla introduced the Model S, a rear wheel drive full size luxury sedan with a range of up to 426 km with the 85 kWh battery pack. In 2014, Tesla announced an all wheel drive version of the Model S with an electric machine on both the front and rear axles. Relatively little engineering information is publicly available on the Tesla drive unit inverters, though several patents have been issued on the mechanical construction of the inverter. The rear drive unit from a 2015 Model S 70D, shown in Fig. 2.5, has been disassembled and the internal construction documented. The internal layout is shown in Fig. 2.6.

Figure 2.5: Tesla Model S dual motor rear drive unit inverter.

On the external cast aluminium housing, the coolant inlet and outlet ports are visible as well as a high voltage DC link connector and a low voltage control connector. The cast housing is bolted to the gearbox housing in which an access port allows the inverter phase cables to be unbolted from the motor phase leads since they are

entirely contained within the drive unit. The inverter consists of the control board which is on top of a stamped metal shield. Under the shield is a plastic cover which retains the silicone gel potting compound that encapsulates the gate driver board. Bus bars are layered beneath the gate driver board followed by the transistors and the DC link capacitor which is at the bottom of the enclosure furthest from the gearbox. Current sensing is providing by two Hall effect sensor ICs embedded in gapped soft ferromagnetic rings which surround two of the phase cables.

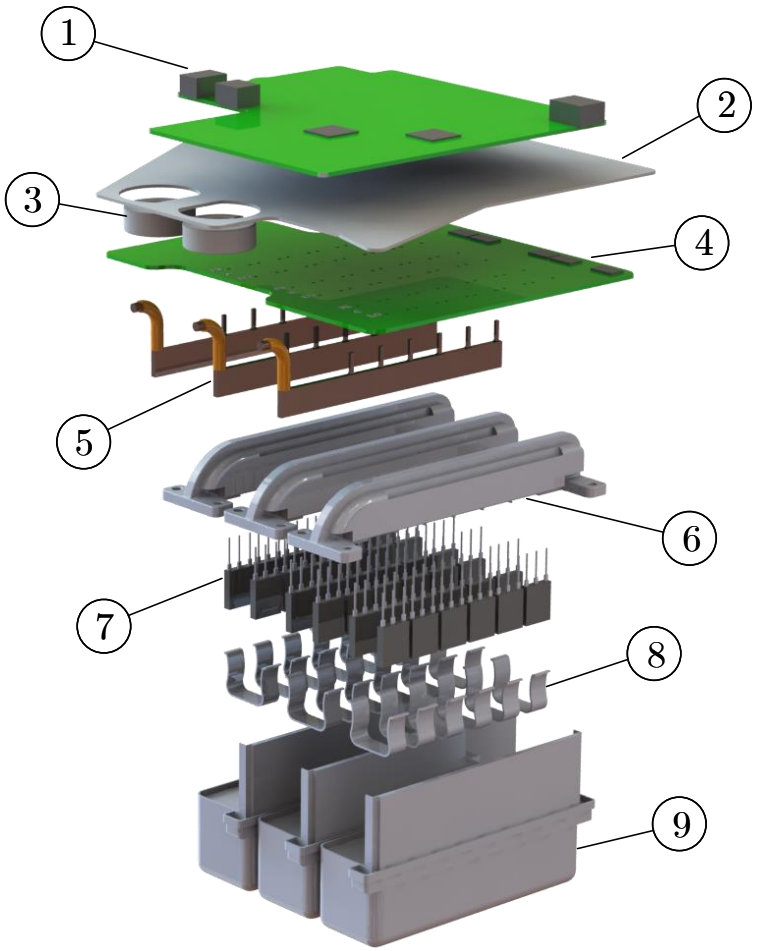

Figure 2.6: Tesla Model S inverter components 1. Control board 2. Aluminium shield 3. Phase current sensor ferrite ring 4. Gate driver board 5. Phase busbars 6. Heat sinks 7. TO-247 package IGBTs 8. IGBT clips 9. DC link capacitors.

Unlike all other inverters surveyed, Tesla has opted for paralleling TO-247 discrete package IGBTs to achieve the required current ratings rather than using power modules. Six IGBTs are paralleled per switch for a total of 36 IGBTs. The IGBT leads are welded to the bus bars and the gate and emitter leads are additionally soldered to the gate drive board. Details of the process are contained in a Tesla patent on the welding and soldering of transistor leads [49]. A second patent describe the bus bar locating component which positions the DC positive and negative bus bars perpendicular to the transistors and the AC phase outputs parallel to the transistors [50].

Coolant from the inlet port is split into three distinct heat sinks which have six transistors affixed with clips to each side. The heat sinks are a two piece casting which is detailed in a third Tesla patent, including the internal fin geometry [51]. The DC link capacitor is located below the transistor stage with a planar terminal connection to the DC bus bars, also described in a Tesla patent [52]. The DC link capacitor placement allows for some passive cooling as evidenced by the fins in the inverter housing casting, while keeping it as far as possible from the electric machine and gearbox which operate at higher temperatures.

The weight and approximate volume of the inverter section of the drive unit was measured to be 5.8 kg and 6.4 L respectively.

2.4 Future Trends

The DOE has identified several potential strategies towards achieving their 100 kW/L inverter target for 2025. Further integration of the inverter subcomponents is considered

Table 2.1: Inverter power density and specific power in recent EVs

Model	Components	Total Power Rating† (kVA)	Power Density (kVA/L)	Specific Power (kVA/kg)
Chevy Volt PHEV (2014) [37]	Dual inverter	180	17.3	21.7
Cadillac CT6 PHEV (2016) [39]	Dual inverter	215	22.6	16.0
Toyota Prius HEV (2016) [42]	Dual inverter, boost converter and APM	162	23.7	13.6
Nissan LEAF BEV (2012) [43]	Single inverter	80[a]	7.1	4.7
BMW i3 BEV (2016) [46]	Single inverter, charger and APM	125[a]	—[c]	6.6
Audi A3 e-Tron PHEV (2016) [48]	Single inverter and APM	75[a]	9.4	7.4
Tesla Model S 70D BEV (2015)	Single inverter	193[a,b]	30.1	33.3

† Total power rating is typically reported for only the inverter(s) while the mass and volume is reported for all components contained in the inverter housing, resulting in lower than actual estimates of power density and specific power. All values are peak output powers.

[a] Values are reported motor power in kW. Inverter kVA rating is likely slightly higher, resulting in lower than actual estimates of power density and specific power.

[b] Motor power as previously reported by Tesla [53]

[c] Volume not reported

necessary, requiring advanced packaging capable of electrical and thermal isolation, while enabling significantly higher switching frequencies and power density. These tightly integrated components will require advanced thermal management systems and materials [54]. Several industry and research trends have also been identified in the areas of component packaging, gate driver design, system integration, and manufacturing techniques. Replacing silicon (Si) power semiconductors with WBG devices also brings significant opportunities to overcome the challenges associated with designing the next generation of traction inverters [55].

2.4.1 Topologies

It is expected the majority of automotive traction inverters will remain conventional two level VSIs. Multiphase two level inverters have been applied where high torque is a requirement, such as in buses and other heavy equipment. TM4 has developed six and nine phase inverters and accompanying PM machines for these applications [56]. As DC link voltages increase, multilevel inverters become more attractive, however the cost of additional switching devices may make them impractical for consumer automotive applications. Research examples of multilevel traction inverters for heavy equipment have been developed [57, 58]. SRMs have also received significant attention as a potential rare-earth material free traction machine. The conventional SRM is driven with an asymmetric bridge converter topology, which while distinct from a two level VSI, has similar requirements for the inverter components. SRM drives have also been commercially applied for traction purposes in heavy equipment [59].

2.4.2 WBG Devices

The application of WBG semiconductors for power electronics including automotive traction inverters has been an area of significant research attention and the DOE has invested heavily in their commercialization through the Advanced Research Projects Agency-Energy (ARPA-E) [60]. In fact, the aggressive 2025 power density targets are reliant on replacing traditional Si power transistors with WBG devices [54]. This is due to the fact that WBG devices have demonstrated numerous advantages over Si IGBTs including higher temperature operation, higher breakdown voltages, and higher switching frequencies while reducing both losses and chip size. Currently Silicon Carbide (SiC) and Gallium Nitride (GaN) are the most promising WBG materials due to their characteristics and commercialization progress [61]. SiC in particular has been an attractive candidate for traction inverters due to its superior high temperature operation which may enable system cost reductions through the unification of the inverter, electric machine, and even ICE liquid cooling loops [62].

The maximum DC link voltage for BEVs is currently around 400 V however further increases are expected. Porsche and Fisker have both announced 800 V architectures with the goal of enabling faster charging rates [63, 64]. While Si devices are capable of 800 V operation, increased switching losses tend to reduce the efficiency making WBG devices an attractive solution for the traction inverter. In 2016, Toyota demonstrated a prototype SiC inverter for the Prius which was reported to achieve a 5% increase in fuel efficiency [65]. Mitsubishi Electric has also developed a prototype SiC traction inverter with a reported power density of 86 kVA/L [66].

Numerous research examples of WBG device based traction inverters have been

reported in [67–70] and reviews on the status and applications of WBG devices to EVs have been conducted in [71–74]. While WBG devices offer many benefits over existing Si devices, the cost premium has been the primary barrier to adoption by automotive manufacturers. This cost is expected to continue to decline as manufacturing techniques improve and the market expands [75, 76]. As an intermediate step towards full WBG utilization, some semiconductor manufacturers have introduced hybrid devices which consist of a Si IGBT and SiC diode in one package. The SiC diode has negligible reverse recovery loss compared to an Si diode which is shown to reduce the total loss by 30-40% [77, 78]. Recently, it has been revealed that the Tesla Model 3 traction inverter is fully SiC MOSFET based with devices from STMicroelectronics [79].

2.4.3 Component Packaging

Multiple approaches can be undertaken to improve the packaging of switching devices, resulting in superior thermal and electrical performance while reducing weight and size. Mitsubishi Electric launched a new IGBT module featuring a unified single layer insulated metal baseplate (IMB), providing both good insulation voltage and high thermal conductivity [80]. Conventionally, ceramic substrates are used for their low thermal resistance in combination with aluminum nitride substrates that provide the electrical insulation. By using the IMB technique, the single layer allows elimination of the bond wires between the substrates and the effective area for chip mounting can be increased by a reported 23%. The heat dissipation is also enhanced thanks to a reported 65% thermal resistance reduction.

Reliability improvements can also be realized through improved packaging and advanced

thermal design. This has been achieved through innovations in the die attach process, enhanced interconnections, and cooling methods such as DSC. Manufacturers have begun to move away from bond wires and soldered connections as they show limitations under high current and high temperature operation [81, 82]. Semikron has developed their line of SKiM modules which use diffusion sinter connections to replace the thermal interface material, solder layers, and bond wires [83]. As a result, high reliability and extended lifetime are achieved under cyclic thermal stresses. Thermal management is also improved along with the power density by extending the heat dissipation area of the module. This is achieved with the DSC method that removes heat from both the top and bottom sides of the module, which can reduce the footprint up to 45% compared to the conventional singled-sided cooling technology [84]. In combination with DSC, bond wires for the top side of the chip can be replaced by planar interconnections [85]. By doing so, the thermal resistance as well as the stray inductance and parasitic resistance are reduced by 30%, 15%, and 75% respectively. Hence, the reliability and thermal capability of the system are increased along with the power density. The DSC technique has been implemented in production inverters by GM with Hitachi and Delphi Technologies modules, as well as by Toyota [48, 86, 87].

Besides the power semiconductors, the DC link capacitors are also under the spotlight as they are typically the heaviest and most voluminous components in a traction inverter. To design their highly power dense inverter, Delphi Technologies and General Electric developed a novel polyyetherimide (PEI) capacitor dielectric film that can operate at higher temperatures [88]. Besides improvement of the capacitor technology itself, better integration of the capacitor with the DC side bus bar also enables some power density and efficiency improvements [89–91]. Indeed, by minimizing the series inductance in the DC side, the voltage overshoot across the switches can be reduced.

Hence, the IGBT modules do not need to be as over designed to ensure a voltage safety margin and the inverter power density can be increased.

2.4.4 Thermal Management

In addition to improvements in the device package, significant research has taken place investigating methods for removing heat from the devices. As device power density increases, it becomes more challenging to extract heat with a conventional liquid cold plate design. As a further improvement to the DSC design, direct cooling has been demonstrated in the Cadillac CT6 inverter in which the module package is fully immersed in the coolant, rather than bolted to a cold plate. Passive 2-phase immersion cooling has been successfully applied to large scale traction inverters for locomotives and mining equipment [92] for some time and may see future applications in automotive. Jet impingement and spray cooling have also received significant research attention [93], along with microchannel heatsinks and heatpipes.

2.4.5 Gate Driver Design

By pushing the performance of IGBT power semiconductors, gate drivers need to be more thoroughly designed and conventional passive circuits show limitations [94]. Indeed, gate drivers are usually designed based on the worst case scenario which limits the switching di/dt to prevent excessive surge voltage, increasing the switching losses. There is a trend to move towards smarter gate drivers that adapt the turn-on and turn-off slopes of the IGBT based on the operating conditions [95]. Active gate drive techniques enable more control of the switching behavior allowing the switching losses,

surge voltage, and EMI emissions to be minimized [96]. For example, Ford developed a dynamic gate driver circuit that reduces the turn-off switching losses by up to 30% while ensuring low cost and similar surge voltage to a conventional gate driver [97]. Toyota developed a gate driver combining a two-stage gate voltage control with an additional feedback circuit [98]. This method achieves a good trade-off between surge voltage and switching losses. TM4 has commercialized their closed-loop gate drive technology which limits both the surge voltage and freewheeling diode recovery current [99]. Smart gate drivers also aim to integrate more protection and monitoring options, such as current and temperature sensing techniques, which can improve the reliability of the device and the inverter [100, 101]. Hitachi has also designed its own gate drivers for its highly power dense traction inverter [86, 102]. The gate driver IC features protection functions to detect excessive temperatures, over-current and under-voltage events. The Nissan LEAF inverter, described in section 2.3.3, employs an active gate drive technique which uses dV/dt feedback from an analog differentiator in order to control the turn off speed, reducing surge voltage and switching losses. The circuit is shown in Fig. 2.7.

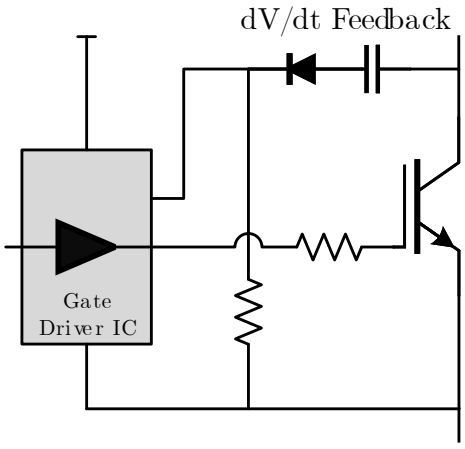

Figure 2.7: dV/dt feedback active gate drive circuit used in the Nissan LEAF inverter.

Besides the need for IGBT gate driver improvements, WBG devices raise new challenges due to their high current densities, fast switching capabilities, and high temperature operation [103–106]. This impacts the driver ICs as they will also need to operate at higher temperatures and ensure higher voltage isolation barriers. Moreover, the fast switching behavior emphasizes the effects of the parasitics responsible for voltage overshoot and ringing. Integration of the driver IC with the power module is a suitable solution to limit the stray inductance as the distance between the gate and the chip is reduced. In [107], Navitas developed the first integrated half-bridge GaN power IC for 650 V that includes protection functions and sensing circuits.

2.4.6 System Integration

Tighter integration of the traction inverter and electric machine has been a clear trend in production EVs. The majority of the production inverters surveyed in this paper have eliminated external phase cabling by packaging the inverter in direct proximity to the electric machine. This reduces both assembly and material cost while increasing reliability. Containing the phase cables within a common motor and inverter housing can also reduce radiated EMI emissions caused by the inverter.

Highly integrated inverters have been proposed in which the inverter electronics are mounted axially with the electric machine allowing a direct connection of the motor windings to the inverter phase terminals. This technique is not unprecedented; manufacturers have integrated rectifying diodes into the housings of automotive alternators for decades [108]. Multiphase machines are an excellent candidate for a highly integrated inverter as the lower phase currents allow the use of smaller switching

devices which can be more easily arranged in a circular format while mitigating the need for additional phase cables. A prototype nine phase drivetrain including a PM machine, gearbox and integrated inverter has been developed to demonstrate the concept [109]. The integrated inverter is reported to achieve a power density of 35 kW/L with the entire system capable of a peak mechanical output power of 60 kW [110].

To further increase the level of integration between the electric machine and inverter, the concept of an integrated modular motor drive (IMMD) has been proposed [111]. The modularization of the machine into concentrated winding pole pieces each with integrated drive electronics allows a further reduction in the total drive volume and enables simultaneous optimization of the machine and inverter characteristics. WBG switching devices are an attractive candidate for IMMD designs as they are capable of the high temperature operation required given the proximity to the electric machine while also allowing a reduction in the DC link capacitor sizing through increased switching frequency and interleaving techniques [112].

Manufacturers have already begun integration of the inverter with the other power electronics modules in the vehicle. This reduces weight and volume as a common housing can be used while potentially allowing sharing of the DC link capacitor and thermal management systems. For the Chevrolet Volt and Cadillac CT6, GM integrates the dual inverters into the same enclosure and Audi A3 e-Tron combines the single inverter with the APM. The Prius dual inverter module contains the APM in addition to the high power DC/DC boost converter while the BMW i3 inverter integrates both the APM and the 3.7 kW OBC. Beyond simply physically integrating the power electronics modules into a single enclosure, there is an interest in integrated topologies

that seek to reduce costs by reusing existing components and devices to achieve a new mode of functionality. In particular, integrated battery charger topologies have been proposed which use existing switching devices from the inverter and in some cases the motor winding leakage inductance to achieve battery charging functionality, eliminating the need for a dedicated OBC [113]. The concept has been implemented in a production vehicle in the Renault Zoe which is capable of charging at up to 43 kW with an integrated topology [114, 115].

2.4.7 Manufacturing Techniques

Mass manufacturing of complex inverter assemblies is a challenging task due to the high number of distinct parts and stringent requirements for reliability and cost. In particular the liquid cooling system often has unique geometries and tight tolerances to optimize coolant flow, maintain a consistent thermal resistance and ensure there is no coolant leakage which could cause catastrophic failure of the inverter. In the current generation Chevrolet Volt and Audi e-Tron inverters, FSW techniques have been applied in the manufacturing process to ensure leak free joins of liquid cooling components without requiring gaskets and fasteners [116]. Heat is generated via friction with a non-consumable rotating tool against the faces of the parts to be joined. This effectively mixes the metals as the tool moves along the join resulting in a high quality weld with minimal distortion. Delphi Technologies has claimed a 45% reduction in footprint and a 50% shorter process time through their FSW manufacturing method for a liquid cooled heat exchanger which is integrated into the inverter housing [37].

Due to recent advances in manufacturing techniques, composite materials have seen

a resurgence of interest for automotive applications which seek to improve vehicle efficiency and range through lightweighting. Composites can be up to 35% lighter than aluminium and 60% lighter than steel, reducing vehicle mass by up to 10% [117]. Several manufacturers have already adopted composite structural components including BMW which uses carbon fiber reinforced plastic extensively in the production of the i3 [118]. This trend may extend to housings and enclosures for vehicle components, including the traction inverter. Carbon fiber reinforced composite enclosures have already been marketed for aerospace applications and with continued cost reduction will become increasingly viable for automotive applications. In addition to the weight savings relative to metal enclosures, they are claimed to have superior EMI performance as the composite material can absorb the radiated emissions rather than reflecting it back to the source [119].

2.5 Conclusions

Traction inverters are a critical application of modern power electronics in developing more efficient, environmentally friendly automobiles. Detailed analysis of several production traction inverter designs is presented based on publications and reverse engineering efforts, including designs from recent model year GM, Toyota, Nissan, BMW, Audi, and Tesla vehicles. Based on the surveyed production inverters and ongoing industry and academic research, future trends in traction inverter design are identified. WBG devices have been of interest for automotive power electronics systems for some time and are just now beginning to see adoption with the industrys first fully SiC traction inverter in the Tesla Model 3. It is likely other manufacturers will follow

suit and WBG device costs will further decline as demand increases, resulting in a new generation of WBG based traction inverters with improved efficiency and power density.

Power semiconductor packaging and thermal management has played a large role in improving inverter reliability and power density. Several manufacturers have now moved to DSC IGBT modules to facilitate lower thermal resistances and increased cooling surface area. Gate driver design has also become critical to increase efficiency, with active gate drive designs reporting up to a 30% reduction in IGBT turn off losses. Fully integrated active gate drive ICs are likely to become widely available, reducing the cost and complexity issues that are currently a challenge for active gate drive techniques.

At the system level, tighter integration of the inverter with both the electric machine and other power electronics modules in the vehicle will result in cost and weight savings. Several manufacturers have already integrated the APM or OBC into the inverter housing allowing a shared DC link capacitor and thermal management system. Direct integration of the inverter electronics into the electric machine housing may present opportunities for further power density improvements as well as the implementation of multiphase machines in certain applications. Challenges with vibration robustness and high temperature operation need to be addressed as manufacturers proceed with further integration of the inverter and electric machine.

Traction inverter design is a challenging and inherently interdisciplinary engineering problem with many competing objectives. It is clear from industry examples that there are multiple valid approaches even with a single standard circuit topology. As more manufacturers introduce EVs with mass market appeal, further innovative solutions

will be required to meet the widely varying demands of various automotive applications.

Chapter 3

Advanced Traction Inverters

3.1 Introduction

In this chapter, a specific selection of the future trends identified in Chapter 2 will be investigated further, with the goal of providing motivation for the topics of the remaining chapters. Power density is an often cited goal in inverter design. Some discussion of the practical limits of power density is presented, along with strategies to further this goal, including the role of efficiency.

For some time now, academic researchers have given significant attention to alternative machine types like SR machines for traction applications. More recently, industry has begun applying SR machines in certain niche applications. A brief discussion on SR machines is presented, and how their expanded application will impact future inverter designs at the topology level.

Finally, as the practical limits of power density are reached, alternative strategies will

be required to achieve further improvements at the vehicle level. Integration of the inverter and OBC at the topology level is particularly promising from both a cost and power density perspective. As an example of the benefits already realized by manufacturers through mechanical integration, a cost analysis and comparison of the BMW i3 integrated and discrete OBCs is performed. A review of integrated charging topologies is conducted and motivation for further development of new topologies is presented.

It is challenging to predict what future traction inverters will look like. This chapter makes the case for inverters featuring high levels of integration at the topology level. The remaining chapters will then present novel embodiments of this trend and supporting theory.

3.2 Power Density

Volumetric and gravimetric power density are standard metrics used to evaluate power converters. For inverters, they are typically specified in kVA/L and kVA/kg respectively. Pursuing high volumetric and gravimetric power densities should not be a goal itself however, but generally used as a means to achieve system level improvements.

Reducing the size of the inverter facilitates increased flexibility in packaging within the vehicle. A smaller inverter also inherently requires less material to construct, therefore reducing the cost. Reducing the mass of the inverter is also an important contribution to reducing the overall vehicle weight. Lightweighting is an important consideration for improving vehicle range, particularly for EVs with heavy battery packs. Gravimetric

power density is even more critical in aerospace electrification applications, where vehicle mass is even more directly coupled with vehicle range.

While many of the strategies for increasing power density will target the component and packaging aspects of the design, it is important to understand the fundamental physical limitations in reducing the size of power converters. While these may be numerous depending on the specific converter in question, three basic limitations common to all electrical systems are presented here.

Current Density

Any non-superconducting material will have a finite conductivity σ which relates the applied electric field $\mathbf{E}$ to the resultant current density $\mathbf{J}$ in the material.

$$\mathbf{J} = \sigma \mathbf{E} \tag{3.1}$$

Considering the units of $\mathbf{J}$, $\mathrm{A/m^2}$ and $\mathbf{E}$, $\mathrm{V/m}$, the power P per unit volume of material V can be stated as

$$\frac{P}{V} = \mathbf{J} \cdot \mathbf{E} = \frac{J^2}{\sigma} \tag{3.2}$$

with units $\mathrm{W/m^3}$. P is known as Joule heating. Since the conductivity is relatively fixed by the material choice, for a given material and current, the Joule heating is determined by the cross sectional area of the material in the direction of current flow. While this is easily applied to conductors like copper, it also holds for other materials such as semiconductors, though the conductivity may now be considered a function of several variables rather than a constant. To increase the overall power density, the material cross sectional area can be reduced, however this results in increased heating.

The loss heat must now be dissipated, resulting in heat flux.

Heat Flux

In the simplest case, heat flux q with units $\mathrm{W/m^2}$ through an isotropic material of length l is described by Fourier's law as

$$q = -k\frac{\Delta T}{l} \tag{3.3}$$

where k is the thermal conductivity in $\mathrm{W/m\,K}$ and ΔT is temperature difference across the material of length l. To achieve effective heat dissipation, ΔT should be minimized. As with electrical conductivity, thermal conductivity is relatively fixed by the material choice. Therefore for a given material and total heat Q, ΔT is determined by the cross sectional area of the material in the direction of heat flux.

Reducing cross sectional area results in increased heat flux, and consequently higher operating temperatures. Like current density, the achievable heat flux in a given material limits the reduction in size of the material while maintaining acceptable temperature.

Dielectric Breakdown

To reduce Joule heating while maintaining the same power, the operating voltage can be increased and the current (and current density) consequently reduced. To maintain the integrity of the circuit, conductors must be surrounded by a dielectric material, or insulator. Equation (3.1) also applies to insulators, but the conductivity is so low that

the current density resulting from an applied field is effectively zero. Equation (3.1) is a simplification however. In reality, the conductivity is a nonlinear function of the applied field:

$$\mathbf{J} = \sigma(\mathbf{E})\mathbf{E} \tag{3.4}$$

Above a certain applied field strength, the material begins to ionize, resulting in high current density. In solids this typically begins as partial discharge which erodes the material. In gases such as air, a high enough field strength results in dielectric breakdown and formation of a plasma arc which supports very high current densities.

Dielectric breakdown effectively limits the allowable electric field strength across an insulator. Practically, for two conductors with voltage difference V insulated by distance d, the allowable field strength E is expressed as

$$\frac{V}{d} = E < E_{crit} \tag{3.5}$$

where E_{crit} is the field strength at which dielectric breakdown occurs. More fundamentally, the critical field is determined by the ionization energy E_i of the atoms constituting the material. While this is still a simplified model, it indicates as voltage increases, insulation thickness d must also increase to prevent dielectric breakdown of the material. While the conductor cross section can be reduced due to the lower current, the consequent increase in insulation may negate the effect [120]. As with electrical and thermal conductivity, dielectric breakdown places limitations on reducing the physical size of the materials.

All three of these limitations are imposed by physical constraints of the material:

1. Electrical conductivity σ

2. Thermal conductivity k

3. Ionization energy E_i

Development of new materials can certainly improve these properties, however this is often costly and the underlying physical limitations will still result in an eventual hard limit being reached. For this reason, there is a need to investigate a macro-level approach for improving the power density of power converters at the system level.

3.3 Efficiency

Future traction inverters will continue to target ever higher efficiencies. As the inverter entirely controls the power flow between the energy storage system (ESS) and the electric machines in a vehicle, it is a critical component in determining the overall system efficiency of a vehicle. Fortunately, inverter efficiencies are already high compared to typical machine and ESS efficiencies, especially for those implemented with WBG devices [121].

The second reason for targeting increased efficiency relates to the heat flux limitation described previously. Reducing loss heat allows for smaller, more power dense systems, without high heat fluxes leading to high operating temperatures. Efficiency is therefore a critical enabler of higher power density designs.

3.4 Alternative Machines

As discussed in Chapter 2, induction and PM machines are by far the most common machine types used in EVs today. One disadvantage of both induction and PM machines is the complexity of their rotors. In the case of the induction machine, the rotor is typically of a squirrel cage construction for traction applications. The rotor conductors add complexity to the manufacturing and produce losses, which are challenging to effectively cool due to the rotor motion. In PM machines, the magnets are expensive and also add complexity to the manufacturing process. Additionally they are at risk of demagnetizing at elevated rotor temperatures. For reasons of both cost and robustness, there is motivation to investigate the application of alternate machine types with simple rotor structures for traction applications.

SR machines are an attractive candidate with a rotor constructed from steel laminations only. As their only torque production mechanism is reluctance torque, SR machines tend to have lower power density than PM machines which have the benefit of PM excitation. Regardless, their robust rotor structure makes them more suitable for high speed operation, which is desirable in some applications. Additionally, the concentrated winding structure of the SR machine provides improved fault tolerance since the windings are electrically isolated from each other, unlike PM machines which are typically wye-connected. The isolated windings necessitates a different inverter topology to drive the machine. While several topologies are possible depending on the application, the most fundamental topology is known as the asymmetric bridge converter, shown in Figure 3.1. When compared with the VSI, the number of diodes and switches is identical, however they are arranged such that the current in each winding is controlled entirely independently.

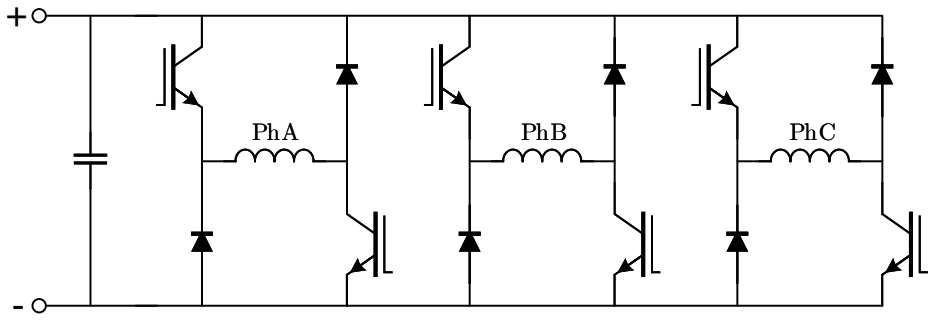

Figure 3.1: Three-phase asymmetric bridge converter topology.

SR machines do have certain challenges which has slowed their widespread adoption for traction applications. In particular, the concentrated winding structure and non-sinusoidal excitation results in high torque ripple when compared with sinusoidally distributed winding machines. Additionally, the radial magnetic forces inherent to the operation of the machine can result in significant acoustic noise. Both the torque ripple and acoustic noises challenges can be addressed through comprehensive model based optimization at the design stage, and through advanced digital control techniques in the inverter [122, 123]. Despite these challenges, SR machines are beginning to make their way into production in the automotive industry for e-supercharger and heavy equipment applications, due to their high speed capabilities and robustness [124, 125]. It is likely that SR machines will continue to expand in niche applications and will eventually be found in consumer automotive traction applications [126].

3.5 Integration

A promising approach for increasing the power density of power converters is integration. Integration refers to combining distinct components such that they become a single component that achieves equivalent functionality. As discussed in Chapter 2, it has

been an ongoing trend in the automotive industry to physically locate distinct power electronics modules in the same housing, resulting in mechanical integration. This can save some cost and increase power density through a reduction in distinct enclosures, mounting structures, and connectors. Internally the converter components remain mostly unchanged however, limiting the magnitude of realizable benefits.

To achieve a step change increase in power density, integration efforts must look beyond only mechanical aspects and consider directly combining the power electronics at the circuit level. If this can be achieved, the internal components can be combined along with the mechanical housing, resulting in a far more significant reduction in volume and mass.

3.5.1 Onboard Chargers

EVs today should allow drivers to recharge the high voltage battery pack from a standard AC grid source such as the single-phase or higher power split-phase wall outlets commonly found in their homes. This is accomplished through the OBC: a dedicated power electronics module which converts the grid AC power to the correct DC output for the battery pack. The OBC typically includes an isolation transformer and several power electronics stages for rectification and DC/DC conversion.

In a typical EV, the inverter and the OBC are the power electronic converters with the highest power rating requirements. Pursuing integration of the inverter and OBC therefore has the largest potential for increasing the power density of the overall system. This concept is known as the integrated battery charger (IBC).

3.5.2 Integrated Battery Chargers

The core premise of the IBC is to repurpose the existing inverter power electronics in the vehicle as a charger, eliminating the need for a separate OBC. Integrated topologies can be applied to either three-phase or single-phase charging at power levels potentially up to that of the inverter rating in the propulsion mode. This has the potential to reduce the vehicle cost, increase the effective power density, and increase the charging power capability [127]. Additionally, some IBC solutions can offer improved functionality, like vehicle-to-grid (V2G) operation, in which the vehicle's battery pack can be used to supply power to the grid or the owner's home.

These benefits come with potential challenges however. If the machine windings are utilized along with the inverter during charging, considerations must be given to preventing the machine from rotating. A detailed analysis of torque production in the charging mode for PM machines and how this can be addressed is conducted in Chapter 4. A second challenge is the lack of galvanic isolation between the grid and vehicle battery in most IBC topologies. The rationale behind including galvanic isolation in conventional OBCs is presented here, along with references to works on potential solutions for non-isolated integrated chargers.

3.5.3 Galvanic Isolation

OBCs today typically implement galvanic isolation between the AC grid and the vehicle with a high frequency isolation transformer [127, 128]. This is done for safety reasons which can be understood by examining the details of the vehicle-grid connection and the converter implementation.

Grounding Schemes

A typical vehicle-grid connection during charging is shown in Figure 3.2

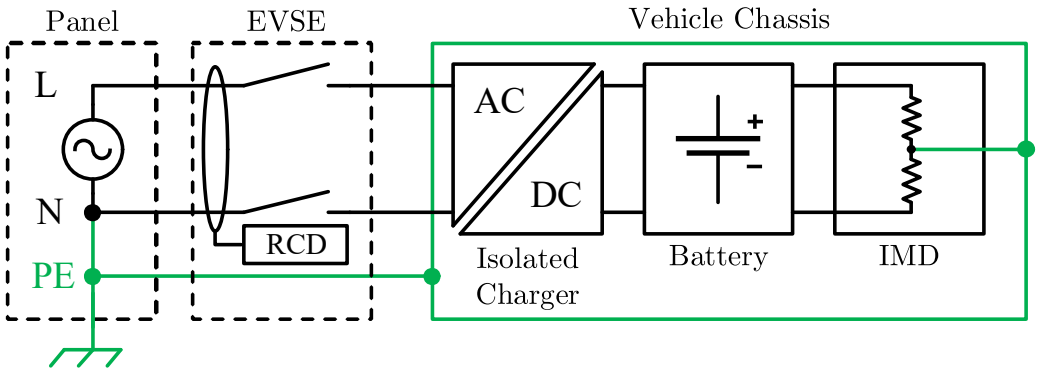

Figure 3.2: Vehicle-grid connection during charging with TN grounding system.

In the terra-neutral (TN) grounding configuration, a low impedance protective earth (PE) conductor connects the vehicle chassis to earth potential through the electric vehicle supply equipment (EVSE). In the event of a fault in which the line conductor (L) becomes connected to the vehicle chassis, the fault current will flow through the PE conductor. This greatly reduces the danger of electric shock should a person be touching the vehicle while standing on the ground during a fault condition, as they will present a much higher impedance path to earth than the PE conductor and no significant current will flow through them [129].

Residual Current Device

While a dedicated PE conductor can provide some level of safety, it remains only a passive system that can itself be subject to faults which could render it ineffective. Additionally, some countries use a terra-terra (TT) grounding scheme in which a PE conductor is not used at all. To further increase human safety during vehicle charging,

a residual current device (RCD) is often included in the EVSE. The RCD measures the line and neutral currents, and ensures they sum to zero. Should there be a fault and some fraction of the current is returning via the PE conductor, a human touching the vehicle, or any other path, the currents will not sum to zero and the RCD can open the EVSE contactors. The RCD therefore offers active safety during the charging process.

Insulation Monitoring Device

Also pictured in Figure 3.2 is an insulation monitoring device (IMD), which is commonly installed in production EV battery packs. It constantly monitors the integrity of the insulation between the positive and negative poles of the battery, and the vehicle chassis. Isolation at the OBC prevents the negative pole of the battery pack from being galvanically connected to the grid neutral, which is connected to the PE conductor at the electrical supply panel. If this isolation is omitted, the IMD would report an insulation fault between the battery negative pole and the vehicle chassis. This can be resolved by disabling insulation monitoring during charging, however like the RCD, the IMD is an active safety device. Careful consideration should be given to the potential safety implications of disabling it.

Common Mode Leakage Currents

PWM based AC/DC or DC/AC converters will create alternating common mode (CM) voltages during their normal operation. These CM voltages can occur at the switching frequency and subsequent harmonics above the switching frequency. Due to

the high frequency nature of the CM voltage, CM currents are able to flow through the parasitic capacitances which are generally unavoidable in the construction of the power converter.

In a traction inverter, shown in Figure 3.3, CM voltages occur at the switching nodes V_a, V_b and V_c, and consequentially at the motor neutral point V_n. This results in displacement current flow through the parasitic capacitances C_p of the power semiconductor packaging to the inverter heatsink and housing (I_{cm1}), as well as through the winding to frame capacitance C_{wf} of the motor (I_{cm2}). Y-capacitors C_Y are therefore placed within the traction inverter to provide a low impedance path for these CM currents to return to their source. To maintain a low impedance return path, C_Y should be sized to be several times larger than C_{wf}, which is typically already many times larger than C_p. This is critical for reducing radiated EMI, as it minimizes the physical loop area of the CM current path. Were the Y-capacitors not present, CM current would flow in the chassis "ground" and return to its source through various other parasitic capacitances like those in the battery pack C_b [130].

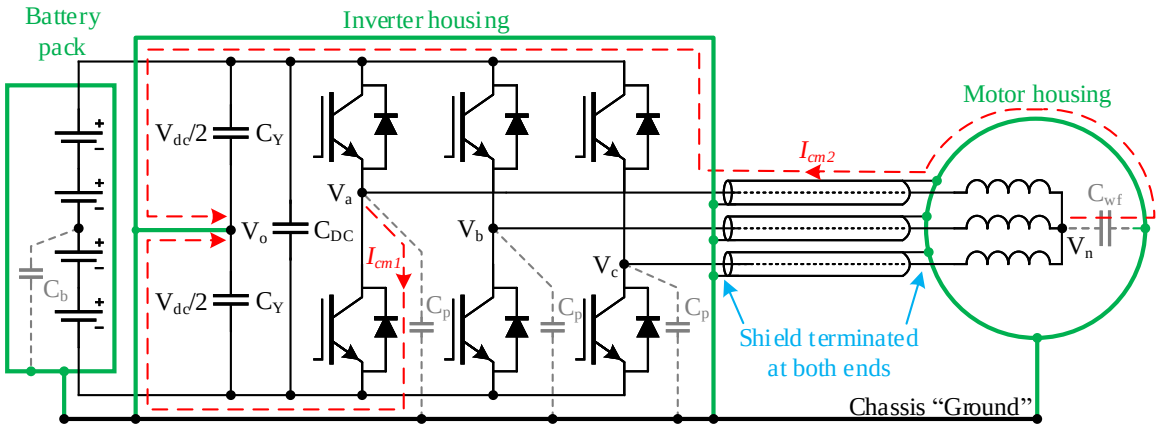

Figure 3.3: Traction inverter common mode current paths with Y-capacitors.

In a non isolated grid connected converter, like a full bridge boost rectifier shown in

Figure 3.4, the switching rectification action results in the alternating CM voltages now appearing at the DC output of the converter. Depending on the state of the IGBT switches, the V_{DC+} and V_{DC-} nodes can vary significantly relative to the chassis ground potential, with high dv/dt. As the converter enclosure is earth grounded, CM current will flow through any parasitic capacitance C_p between the DC output rails and the enclosure. This parasitic capacitance is typically small enough that only a small amount of high frequency CM current flows, which can be returned to its source through small AC side Y-capacitors C_{Yac}. This current is denoted as I_{cm1}.

If Y-capacitors C_Y like those required in the traction inverter are present on the DC output, an unwanted CM current path is created in which I_{cm2} can flow. Since V_{DC+} and V_{DC-} experience alternating voltage swings relative to chassis "ground" with high dv/dt, significant current may flow through C_Y. Depending on the relative impedances presented by C_{Yac} and L_{PE}, some fraction of I_{cm2} may return via C_{Yac}, however since C_Y is typically much larger than C_{Yac} and L_{PE} is small, the majority of the current will flow in the PE conductor as I_{PE}. Current in the PE conductor is often referred to as leakage current.

In the traction inverter, C_Y provides a controlled low impedance return path for the inevitable CM currents produced in the traction inverter and motor. In the grid connected converter, C_Y now provides a low impedance path which results in significantly more CM current flow than would have existed otherwise. This can fundamentally be attributed to the inverter being DC bus referenced, with a floating AC output, while the grid connected converter is AC mains earth referenced, with a floating DC bus. Using the same DC side Y-capacitors for both systems is suboptimal. The undesirable increased CM current flow creates the following problems, which are

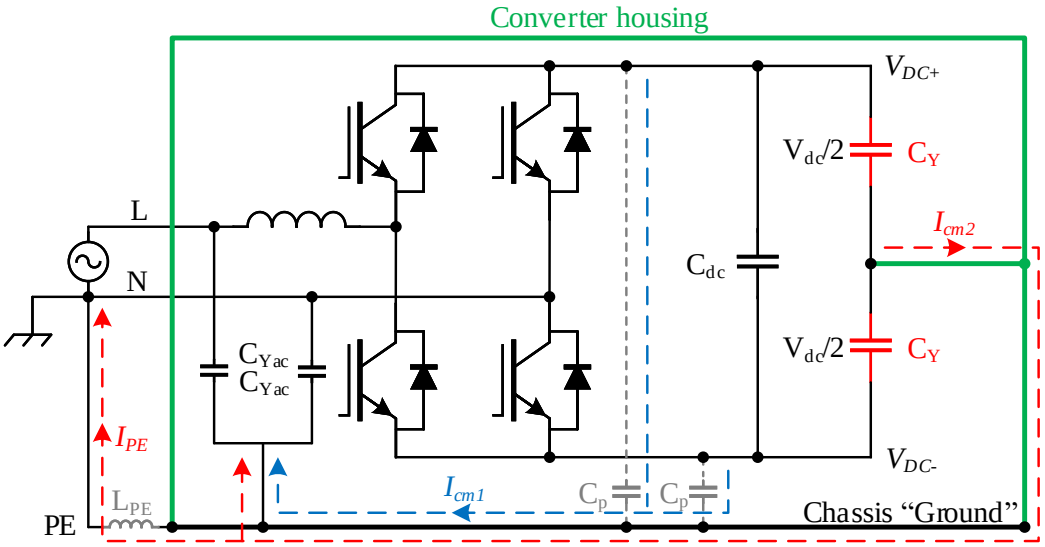

Figure 3.4: Non isolated TN grid connected converter with large DC side Y-capacitors.

further detailed in [129]:

1. Potential for electric shocks to the user in the case of a TT grounding system or a TN grounding system with open circuit PE conductor fault

2. Tripping of the RCD due to CM leakage current flowing in the PE conductor

3. Damage to the Y-capacitors, if the larger CM current exceeds their current ratings

4. Failure to meet conducted emissions standards, due to CM current flow in the PE conductor, which must return in the L and N conductors

5. Circulating CM currents if other non-isolated chargers are connected to the same local grid

In a conventional OBC, shown in Figure 3.5, the AC grid and DC battery sides of the converter are galvanically isolated with a transformer. An ideal transformer will

prevent any CM current flow between the primary and secondary windings. Any CM current generated on the DC side of the converter is therefore restricted from flowing back into the grid along the PE conductor.

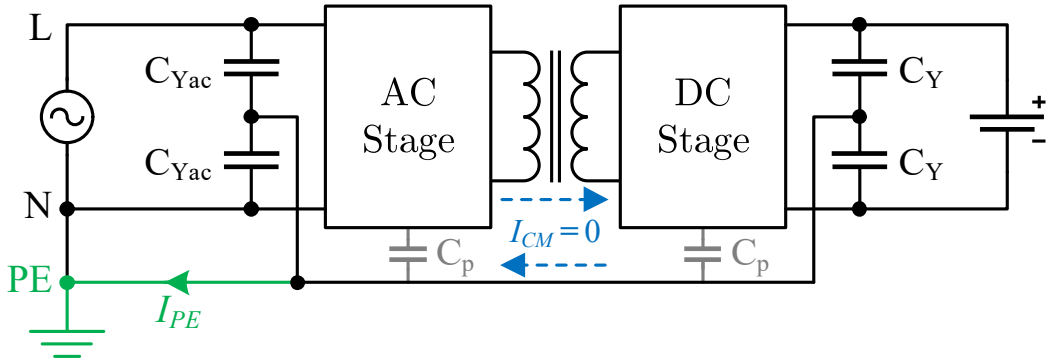

Figure 3.5: Typical isolated OBC implementation.

Potential Solutions

Several solutions have been proposed for resolving the CM leakage current problem in non-isolated integrated converters. Alternative PWM schemes have the potential to reduce or eliminate CM voltages at the motor neutral point, which can greatly reduce the size of the required Y-capacitors in the inverter [131]. However these alternatives schemes often come at the expense of increased THD.

The specific implementation of the non-isolated grid connected converter will also have an influence on the CM leakage current in the presence of large DC side Y-capacitors. For example the totem pole PFC rectifier, discussed in detail in Chapter 6, reduces the CM voltage swings from occurring at the switching frequency to occurring at the line frequency, resulting in a significant reduction in CM current flow through any DC side Y-capacitors.

Entirely disconnecting the large DC side Y-capacitors during charging is also a viable option. The integration of a switching element in series with the capacitor could inhibit its high frequency performance, so careful design is required, considering the required bandwidth of the Y-capacitors in the inverter mode.

The motor CM voltage can also be eliminated with sine wave filtering of the output voltage, which may become practical with very high switching frequency inverters as demonstrated in [132] and [133]. This will eliminate current flow through the winding to frame capacitance, reducing the required Y-capacitor size. It may also be possible to even further reduce the Y-capacitor size by reducing the parasitic switching device package capacitances through non-metallic heatsinks [134].

Active CM filters and floating filters are also a promising approach to enable safe non-isolated vehicle charging. Active CM filters can inject current such that the net leakage current is close to zero [135]. While the principle is relatively simple, the implementation can require high bandwidth, high voltage circuitry, which can be challenging to achieve cost effectively. A floating filter design is prototyped and experimentally validated for an integrated charger application in [136]. Essentially two sets of DC side Y-capacitors are implemented, in which the majority of the CM leakage current is directed through the floating filter, back to the AC input of the converter, but away from the PE conductor. The remaining high frequency CM current can be bypassed with smaller Y-capacitors as usual, keeping the total leakage current low.

Isolated IBC topologies have also been proposed, though not as extensively as non-isolated topologies. Isolation is achieved through two primary methods: using the machine as a transformer or introducing an offboard transformer while still repurposing the machine as in the non-isolated case. In both methods the inverter is used as a

rectifier. Using the machine as a transformer requires the machine to be specially designed with dual, mutually coupled windings or some means of reconfiguring them as such [137]. This places significant requirements on the design of the machine to make it suitable for use in an IBC, making it less attractive for general applications. Offboard isolation may be suitable for some applications, but would require an isolated EVSE, making the system incompatible with existing EVSEs.

While the lack of galvanic isolation is certainly a challenge for non-isolated IBCs, safe charging can be achieved through careful design and proper mitigation of leakage currents. The high frequency transformers found in conventional isolated OBCs add to the cost and weight while reducing the efficiency due to the additional converter stages required. Non-isolated IBCs have the potential to eliminate the need for a discrete OBC while also improving upon the conventional OBC topologies from a cost, weight and efficiency perspective. As mentioned in Chapter 2, a non-isolated 43 kW integrated charger developed by Continental has previously been implemented in the Renault Zoe EV, indicating the commercial viability of such a solution [128].

3.6 BMW i3 Analysis

As discussed in Chapter 2, the BMW i3 features a traction inverter with a mechanically integrated 3.7kW OBC and 12V DC/DC converter. The integrated design was first analyzed by ORNL in [54]. A significantly more in depth analysis from a manufacturing costing perspective was conducted by Munro & Associates in [138]. Interestingly, the i3 also includes a second discrete 3.7kW OBC option which can be operated in parallel with the integrated OBC, to achieve 7.4kW charging. This makes the i3 an excellent

candidate for quantifying the benefits of mechanical integration of the OBC, as the integrated and discrete solutions can be directly compared. The mechanically integrated solution can then be considered as the benchmark with which proposed electrically integrated solutions can be measured against. This comparison can be considered conservative, as many production vehicles do not feature any mechanical integration, making the potential benefits of electrical integration even more pronounced.

3.6.1 Methodology

Based on analysis of the values reported in [138], an approximate cost breakdown of the inverter, integrated OBC, and discrete OBC can be established. Additionally, a weight breakdown of the discrete OBC can be determined. Since the reported values are categorized based on how the components are manufactured rather than their functionality, it is challenging to separate some of the values for the integrated inverter and OBC. In the cases where the components are shared between the inverter, integrated OBC and integrated APM, the subcomponents were evaluated to establish a relative cost fraction for each. For example, based on the IC content of the integrated inverter and OBC control board, approximately 30% of the cost can be attributed to the charger functionality. Values are reported on a relative rather than absolute basis, as the intention is to show a representative breakdown of a typical solution rather than the specific implementation in the i3.

3.6.2 Results

First, the total costs are compared for the inverter with integrated OBC, and the discrete OBC, as shown in Figure 3.6.

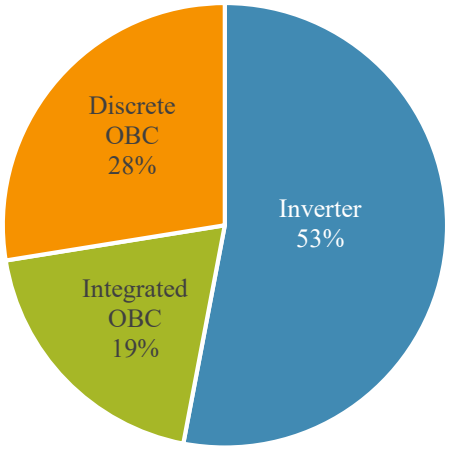

Figure 3.6: BMW i3 inverter and OBC power electronics cost breakdown.

As expected, the integrated OBC represents a lower fraction of the cost than the discrete OBC. These components can be further broken down to their individual parts. The inverter cost breakdown is shown in Figure 3.7. The discrete and integrated OBC cost breakdowns are shown in Figure 3.8a and 3.8b respectively.

The largest inverter cost is the IGBTs. The control board also represents a significant portion of the cost, primarily due to the DSP and FPGA content.

Comparing the discrete and integrated OBC, the enclosure, heatsink, and control board represent a larger fraction of the cost in the discrete OBC, as their cost is not shared with the inverter.

The direct comparison shown in Figure 3.9 indicates the mechanically integrated 3.7kW OBC is approximately 70% the cost of the discrete 3.7kW OBC.

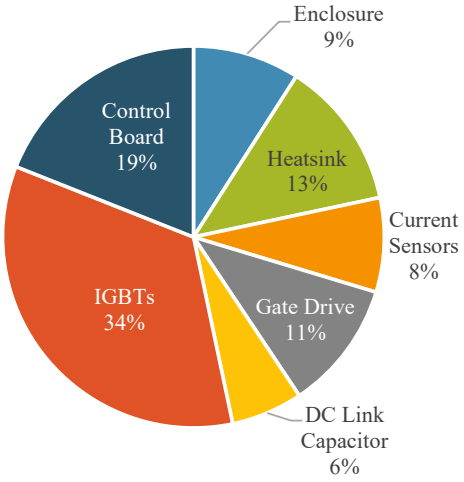

Figure 3.7: BMW i3 inverter cost breakdown.

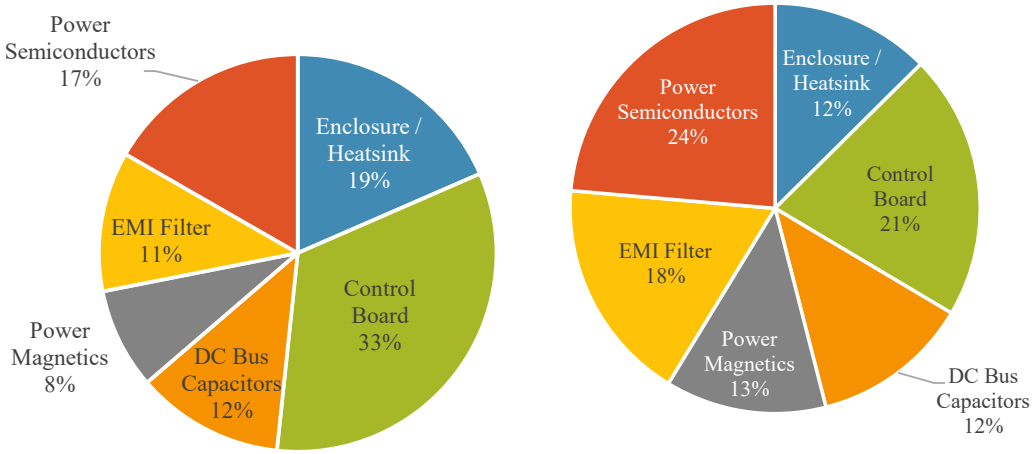

(a) BMW i3 discrete OBC cost breakdown.

(b) BMW i3 mechanically integrated OBC cost breakdown.

Figure 3.8: Discrete and integrated OBC cost breakdowns.

While detailed information is available for cost, weight is only provided for sub-assemblies rather than individual parts. Therefore it is not possible to establish the weight breakdown of the integrated OBC, however the discrete OBC weight can be broken down at the sub-assembly level. The approximate weight breakdown of the discrete OBC is shown in Figure 3.10. Notably the enclosure and heatsink make up a significant portion of the weight. Mechanical integration can potentially reduce these

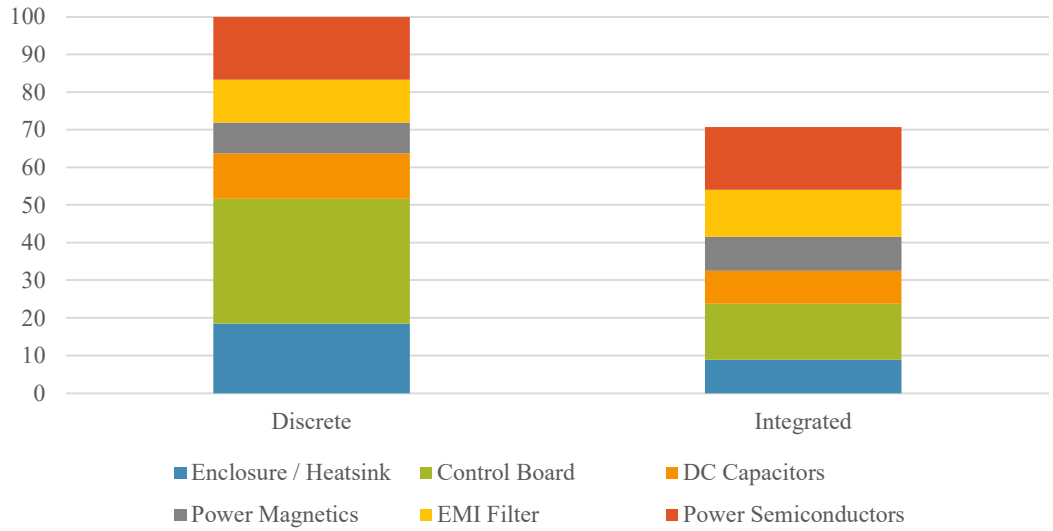

Figure 3.9: BMW i3 discrete and mechanically integrated OBC cost comparison.

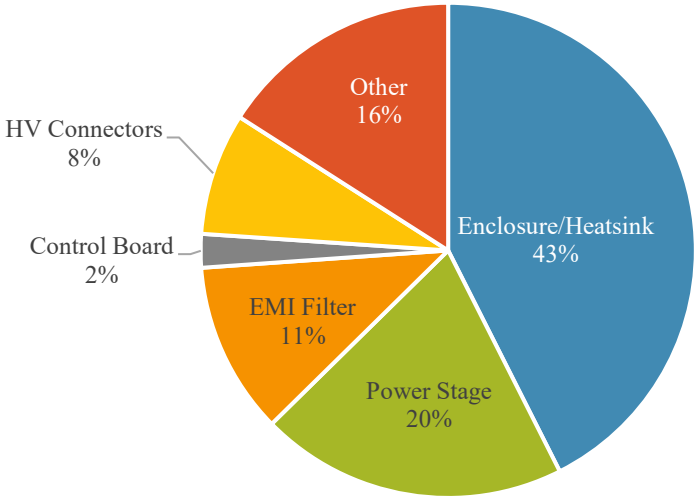

Figure 3.10: BMW i3 discrete OBC weight breakdown.

weights, along with the HV connectors. Electrical integration has the potential to also reduce the power stage weight, while the EMI filter weight will likely remain roughly the same. This comparison, including electrical integration, is revisited in Chapter 7.

3.7 Review of IBC Topologies

In this section, a literature review of IBC topologies is presented, focusing on non-isolated chargers. Non-isolated chargers can be further classified based on which components of the powertrain are reused to implement the IBC, primarily those using both the traction inverter and machine, those using only the inverter without the machine and those using neither the inverter or machine but using a high voltage DC/DC converter between the battery pack and the inverter [113]. In a BEV the higher voltage battery pack will likely eliminate the need for a DC/DC converter to boost the battery pack voltage before the inverter, thus making topologies reliant on the DC/DC converter unsuitable for fully electric vehicles. Use of the electric machine is also likely a requirement as passive elements with power ratings suitable for charging at higher power levels are bulky and expensive and can be obtained essentially for free through repurposing of the electric machine. Therefore, for non-isolated chargers, topologies using both the traction inverter and machine will be the primary focus as they are the most suitable for general adoption in consumer EVs.

3.7.1 Chargers Accessing the Machine Neutral Point

A non-isolated charger can be implemented by using the machine windings and inverter to form a boost rectifier topology. For a three-phase wye-connected machine, the phase neutral points are disconnected from each other and connected to the three-phase grid. A 1994 patent by AC Propulsion demonstrates a single-phase and three-phase non-isolated charger using the machine windings as filter inductors and the inverter as a rectifier [9]. This topology can also be isolated through the use of an offboard

isolation transformer as presented in [139].

The primary concerns with this topology are torque production, vibrations, and acoustic noise, as a rotating field will be produced by the three-phase grid frequency currents in the stator. The machine must also have the neutral point of all three windings externally accessible and contactors are required to reconfigure the windings between the charging and propulsion modes. Finally, the boost rectifier topology requires that the peak AC grid supply voltage be lower than the DC link voltage to ensure control of the output current and to maintain unity power factor operation. This may pose a challenge for lower voltage battery packs at low states of charge (SOC). This requirement can be alleviated with the use of a DC/DC converter to buck the rectifier output down to the required battery voltage as shown in [140] however, as mentioned previously this DC/DC converter is unlikely to be present in all vehicles.

One solution to the torque production problem, patented by Renault, is through the use of a separately excited synchronous machine in which the excitation winding power is cut off in the charging mode [141]. Contactors are still required to reconfigure the windings and an additional excitation winding supply is now required adding to the system cost. Separately excited machines are also much less common than induction and PM machines in traction applications. Another solution presented in [142] involves a specially designed PM machine with dual stator windings. The windings are reconfigured from a delta configuration in the traction mode to an open ended configuration in the charging mode and are arranged such that the grid currents flow in opposite directions through the paralleled windings, cancelling the flux and ideally eliminating any torque production or vibrations. This solves the torque production issue, but evidently requires a special machine design specifically for this

purpose.

3.7.2 Chargers With External Interface Converter

To further reduce torque production and vibration issues, the addition of a non-integrated three-phase rectifier to interface with the grid has been proposed. This results in only DC current flowing through the machine windings. In the solution presented in [143], an interface converter is implemented requiring an additional six switches and six diodes. The resultant topology is similar to a non-inverting buck-boost converter and as such can output a DC voltage higher or lower than the grid voltage. An additional benefit of this topology is that no access to the machine neutral point is required and no reconfiguration of the system is needed between the propulsion and charging modes. The evident disadvantage is the addition of non-integrated components which according to the authors, result in a slightly higher cost than the OBC but are capable of much higher powers while being much lower in cost than an equivalent offboard charger. A single-phase version of this concept is also presented in [144]. The three-phase interface converter is simplified to a full bridge diode rectifier for single-phase operation.

Interestingly, the integrated charger with an interface converter is currently the only known production vehicle implementation of an integrated charger topology, found in the Renault Zoe. Patents issued to Renault describe a fast integrated charger with an interface converter as well as an additional DC/DC converter which accesses the machine neutral point to use the three paralleled phase winding inductances [115]. Continental has also developed an integrated charger topology called “AllCharge”

[145]. While few details on the technical implementation are available, it is claimed to be capable of up to 350 kW charging power which would make it the highest power integrated charger to date.

3.7.3 Chargers With Split Winding Machines

Another topology has been proposed which eliminates both torque generation from three-phase currents and the need for additional contactors to reconfigure the machine windings. An open ended, split winding machine and accompanying three-phase H-bridge inverter are proposed in [140], [146] and [147]. The three-phase grid is connected to the midpoints of the machine windings while each end of the winding is connected to a phase leg of the inverter. The grid current flows in spatially opposite directions in each half of the coil, cancelling any flux generation. Each H-bridge converter in the charging mode effectively acts as a two phase paralleled boost rectifier and is equivalent to two VSIs in parallel in the propulsion mode. A DC-DC converter is only required if the battery voltage is lower than the peak AC input voltage. Evidently this topology requires a specially constructed machine with nine terminals for the windings and their midpoints. The number of switches in the inverter are doubled however the current rating for each switch is halved [148]. This topology also allows for interleaved control of the phase legs to improve the grid current THD without increasing switching frequency or adding passive filters.

3.7.4 Chargers Using Multiple Machines

Other integrated charger topologies have been proposed for powertrains with multiple machines. In [149], a strategy for mechanical torque cancellation in two PM machines with coupled shafts is presented. This topology requires both machines to be of open ended winding type and includes two additional sets of contactors to switch from a neutral point connection to the three-phase grid connection. The machine rotors should be properly aligned before charging which is a disadvantage of this topology as it requires special mechanical considerations for independently rotating the motors before charging. Interleaved switching of the two VSIs allows for lower grid current THD.

Another topology is proposed for a powertrain with four three-phase electric machines and four VSIs in [150]. One phase of the three-phase grid is connected to each of the neutral points of three of the machines and the fourth machine is unused. No torque is generated in any of the machines as the same current flows in all three stator windings which will not induce a rotating field. While this topology requires access to the machine neutral points, it only requires a single terminal since the phases are not reconfigured in any way during the charging mode. The main disadvantage of this topology is the high cost of the required three or four motor powertrain, making it unlikely to be widely adopted in production vehicles. This topology is electrically equivalent to a nine phase machine topology which is discussed in the next section.

3.7.5 Chargers Using Multiphase Machines

Multiphase machines (machines with more than three phases) are attractive for high power, integrated charger implementations as they provide additional degrees of freedom over three-phase machines which can be used to eliminate torque production in the machine. While multiphase drives are occasionally found in high power industrial applications, they have seen little adoption in the automotive industry likely due to the cost of the additional semiconductor switches and phase cables. One example of a production six phase and nine phase machine and inverter for heavy duty vehicle applications is TM4's SUMO offerings [151].

Integrated chargers using multiphase machines can either be supplied by a single phase, three-phase or multiphase grid. In [152] a theoretical analysis of a five phase machine supplied by a five phase grid is presented. Phase transposition is employed to eliminate electromagnetic torque production in the machine. The analysis is generalized to machines with a higher odd number of phases. A similar concept is presented in [150] and [153] for a six phase machine. An offboard isolation transformer with dual secondaries is proposed to generate a symmetrical six phase voltage supply from a three-phase grid connection. Phase transposition is again employed to eliminate torque production. While phase transposition provides a simple solution to torque production during charging, generation of a multiphase voltage supply requires large and costly offboard transformers making the solution less attractive for widespread implementation.

A symmetrical six phase machine with a nine switch converter topology for integrated charging is presented in [154]. In the charging mode, the topology is configured such

that it is equivalent to a three-phase boost rectifier with the motor phases paralleled such that flux is cancelled, preventing torque production. During the motoring mode however, the winding configurations results in a maximum modulation index of 0.5, requiring a DC link voltage twice that of a twelve switch six phase converter. While this higher DC link voltage may be achievable if a boost converter is present, it is otherwise an unacceptable tradeoff to achieve integrated charging functionality. Additionally the machine must have open ended windings resulting in twelve phase terminals. Nine contactors are required for reconfiguration between motoring and charging modes.

Nine phase machines offer an elegant solution for three-phase charging as no reconfiguration is required between motoring and charging modes and only the single neutral terminal for each group of three-phase windings needs to be made accessible. A theoretical analysis of a nine phase machine integrated charger topology is developed in [155] with experimental results presented in [156] and an efficiency analysis conducted in [157]. The topology offers inherent torque production elimination with no reconfiguration requirements however it requires an 18 switch inverter and twelve phase terminals, including the three neutral point terminals. One potential solution to the large number of phase cables is development of an integrated motor drive as demonstrated in [109]. The nine phase inverter is built into the motor housing, eliminating phase cables all together. Further comparisons of five, six and nine phase machine based integrated chargers are discussed in [158].

3.7.6 Chargers Using Switched Reluctance Machines

SRMs have not yet seen adoption in the automotive industry for traction applications though they are a promising candidate due to their low cost, simple construction which requires no permanent magnets. Since the SRM is inherently an open ended winding machine, integrated charger topologies do not impose any additional requirements on the neutral point accessibility. Torque elimination is still a concern in topologies using the machine windings as filter inductances as the rotor will tend to rotate to the minimum reluctance position as the windings are excited.

Much of the research into IBCs based on SRM drives has focused on single-phase charging. A single-phase integrated charger based on a four phase SRM and asymmetric bridge converter is presented in [159]. The topology also includes a front end DC/DC converter which in the charging mode results in a buck-boost converter topology capable of active power factor correction. A similar single-phase topology is proposed in [160], however the machine features split windings and utilizes two isolated DC battery sources, enabling multilevel operation. A third similar single-phase buck-boost topology is presented in [161]. A topology capable of split-phase charging is shown in [162], also including a front end DC/DC converter. While these topologies require minimal reconfiguration and additional components, they are restricted to single-phase operation and dependent on the presence of a front end DC/DC converter.

A three-phase integrated charger based on a three-phase SRM and C-dump converter for a hybrid vehicle application is presented in [163]. The topology requires a three-phase diode rectifier to convert the grid voltage to DC and two contactors to enable reconfiguring the C-dump converter to either a buck or buck-boost converter for

charging operation. A multi source topology including batteries and ultracapacitors capable of three-phase integrated charging is shown in [164]. In [165] a three-phase active PFC boost converter front end rectifies the grid current and the four phase asymmetric bridge converter is used as an interleaved buck converter. This topology is promising for high power operation but requires six additional switches and three filter inductors in the boost rectifier front end. The split winding three-phase asymmetric bridge converter based topology in [166] achieves power factor corrected three-phase charging with flux cancellation. The front end DC/DC converter again results in a buck-boost topology however if the grid voltage is below the battery voltage, the DC/DC converter is not required and the topology can be simplified to a boost rectifier. The topology requires two asymmetric bridge converters in parallel per phase and an additional six terminals for the winding midpoints but requires no reconfiguration between the propulsion and charging modes.

SRM based powertrains show strong potential for IBC applications. Since it is not a given that a three-phase SRM is ideal for traction applications, further research is necessary on integrated charger topologies for higher phase count machines.

3.8 Conclusions

This chapter provides a conceptual justification for selected proposed future trends in traction inverter development. The physical limitations of power density for power converters are discussed. These limitations lead to the concept of integration, as a system level alternative to increasing the power density of individual converters directly. The traction inverter and OBC are identified as the primary candidates for integration

in an electrified vehicle. Common challenges for IBCs are presented, including galvanic isolation, which is discussed along with possible solutions. A cost analysis of the BMW i3 indicates that the mechanical integration alone of the OBC can result in a 30% cost reduction when compared with a discrete OBC implementation. A review of existing IBC topologies in the literature is presented. Additional challenges are identified in many of the proposed topologies, including special machine designs specifically for integrated charging, the addition of contactor devices for winding reconfiguration, and requirements for non-integrated power electronics components. While a significant number of IBC topologies have been proposed, very few IBC topologies have ever been commercialized. Evidently additional research is justified, with careful consideration paid to the practical aspects of integration such that the concepts may be viable in the automotive industry.

Chapter 4

Theory of Integrated Chargers

4.1 Introduction

Power electronics is fundamentally concerned with transforming electrical power from one form to another, and the multitude of practical ways in which this can be achieved. Considering at a high level how the traction inverter and OBC transform electrical power, commonality between the systems can be identified and opportunities for integration explored. This chapter presents a conceptual basis for the development of IBC topologies, through manipulation of the standard traction inverter circuit by decomposing it into fundamental converter cells. Additionally, a model for electric machine behaviour in IBCs is developed from first principles.

Figure 4.1 shows the charger, at a fundamental level, converts AC grid power to DC which charges the battery. The AC grid power is often single or split-phase, though it may also be three-phase. The power flow is typically unidirectional, though may be

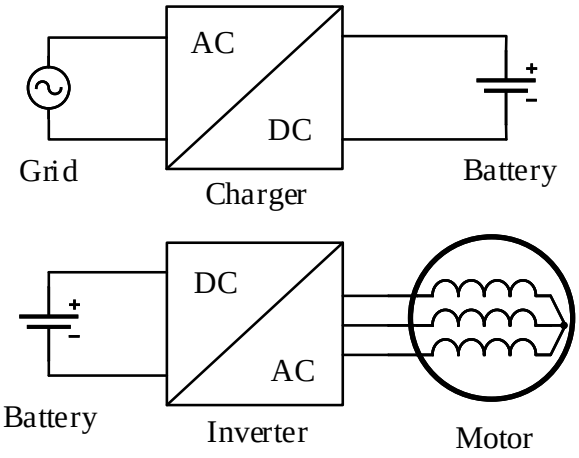

Figure 4.1: Power conversion block diagram of the onboard charger and traction inverter in an EV.

bidirectional to achieve V2G functionality. The inverter converters DC battery power to three-phase AC to drive the electric machine. The power flow is bidirectional to allow regenerative braking. Additionally the fixed nature of the grid supply typically dictates that the vehicle be stationary during charging. This high level analysis leads to two simple but critical insights:

1. Both the inverter and charger implement AC/DC power conversion

2. The inverter and motor are idle when the charger is operating, and the charger is idle when the inverter and motor are operating

It is the combination of the functional commonality and the temporal exclusivity between the two systems that allows the possibility of integration.

4.2 Fundamental Converter Circuits

With the basis for integration established, the implementation details can begin to be addressed. In power electronics, a number of fundamental converter circuits exist, which can be considered the building blocks for achieving more complex power conversion functionality. Five of the fundamental converter circuits which are most applicable to inverter and charger implementations are presented here. The schematics are shown with generic single pole double throw (SPDT) switches, which are modulated between the on state with terminal 1 connected, and the off state with terminal 2 connected, at duty cycle d. Each converter's voltage transfer function $\frac{V_o}{V_i}$ is shown as a function of the duty cycle.

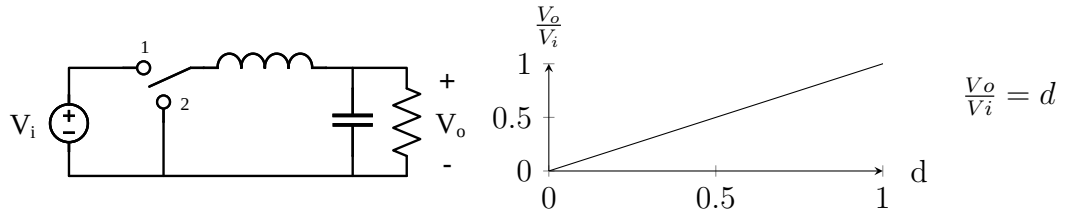

Figure 4.2: Buck converter.

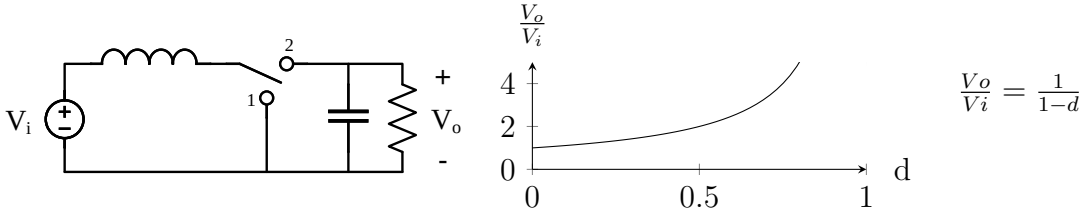

Figure 4.3: Boost converter.

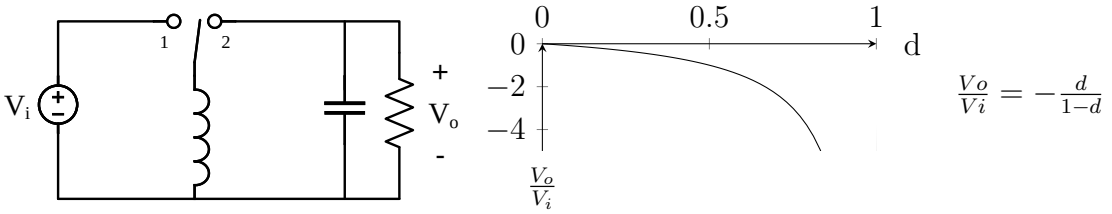

Figure 4.4: Buck-boost converter.

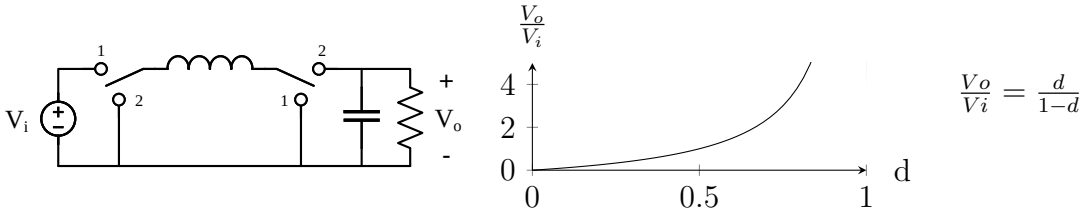

Figure 4.5: Non-inverting buck-boost converter.

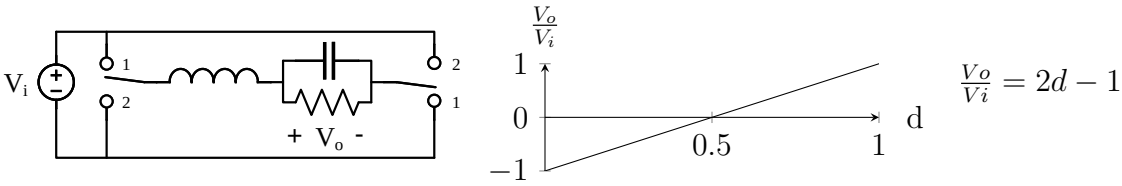

Figure 4.6: Full bridge converter.

4.2.1 The Three-Terminal Cell

These converters all share a common element known as the three-terminal cell, which is formed by a SPDT switch and an inductor [167]. The three-terminal cell is shown in Figure 4.7. By simply rotating the connection of the terminals a, b, and c, it can be seen how the three-terminal cell can form a buck, boost, or buck-boost converter. For example, the boost converter can be obtained by switching the source and load connections of the buck converter, which is equivalent to rotating the three-terminal cell by 180 degrees. The non-inverting buck-boost converter and the full bridge converter can be derived from the buck and boost converter. The non-inverting

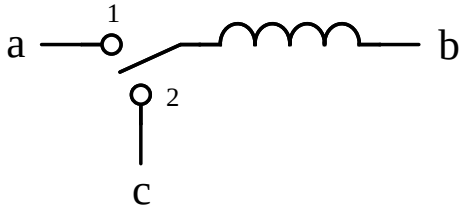

Figure 4.7: Three-terminal cell.

buck-boost converter is a buck converter cascaded with a boost converter. The full bridge converter can be considered two buck converters connected to the same load with opposite polarities, enabling a bipolar output voltage. Both the non-inverting buck-boost and full bridge converters contain the equivalent of two three-terminal cells, though their inductors are shared.

This fundamental power conversion element and its ability to change functions based on its orientation within the circuit is the foundation for developing integrated charging solutions. Indeed, integrated solutions must also change functions as required. The cascading and rotation principles of the three-terminal element are instructive in how this can be achieved.

4.2.2 Three-Phase VSI

The three-phase VSI topology discussed previously can be reconsidered as three buck converters with the loads sharing a common neutral point, shown in Figure 4.8. This results in similar properties to the full bridge converter, in which bipolar output voltages are possible. In the case of a typical motor drive, the voltage waveform does not significantly affect the torque, so the output capacitor filters can be neglected. The motor windings present an inductive load which effectively filters the resultant

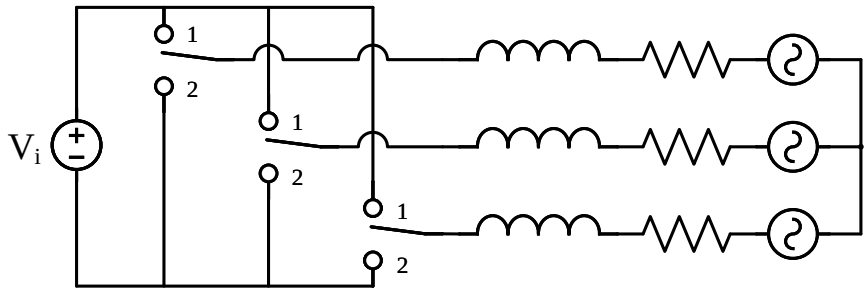

Figure 4.8: Simplified voltage source inverter with generic SPDT switches.

current waveform, removing the need for a discrete output inductor as well. When the duty cycle of the switches are modulated sinusoidally, a sinusoidal current results.

Considering an inversion of source and load for the three-phase VSI results in three boost converters. Indeed this is the principle of regenerative braking, in which energy from the motor is returned to the DC source. If a AC grid were to be connected in place of the motor back EMF sources in Figure 4.8, battery charging could be implemented through proper control of the VSI switches, with the motor windings providing the necessary inductances for the boost converters. The three-phase windings could support a single-phase, split-phase or three-phase grid connection. This concept, while appealing due to its simplicity, presents two primary challenges:

1. The machine must be reconfigured from a wye connection to an open ended winding configuration to allow connection of the three-phase grid.

2. The boost converter can only control the flow of current if the peak grid voltage is below the DC link voltage.

The first challenge can be resolved through the addition of relays to reconfigure the neutral point connection, or through the use of an open ended winding machine, shown in Figure 4.9a, driven by two three-phase inverters. In either case, a new machine

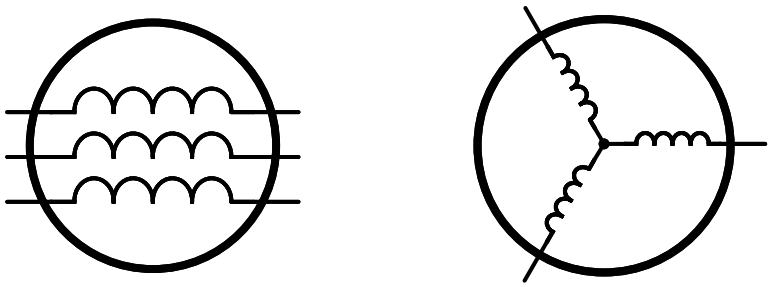

(a) Open ended winding machine. (b) Wye-connected machine.

Figure 4.9: Machine winding configurations.

design is required which makes these solutions potentially less appealing, as discussed in Chapter 3. Other machine types such as SR machines are inherently built with an open ended winding construction, and will be considered in Chapter 5. A third possibility is to use an external inductor and a relay to disconnect the motor phase entirely. The three-terminal cell is therefore formed by the inverter SPDT element and the external inductor which is switched into the circuit when it is required. This eliminates any restrictions imposed by the motor construction, but reduces the level of integration by requiring additional components not already present in the system.

The second challenge could be addressed by limiting the allowed grid voltages for the charging operation, however this restricts the application of the integrated charger to systems with very low grid voltages or very high nominal battery voltages. This challenge can be more generally solved through further application of integrated converters.

Regardless of these challenges, it is still desirable to take advantage of the motor winding inductance in the formation of a new converter for charging purposes. The wye-connected machine shown in 4.9b can still be used as a single inductance in the charging mode, without any changes to the machine itself.

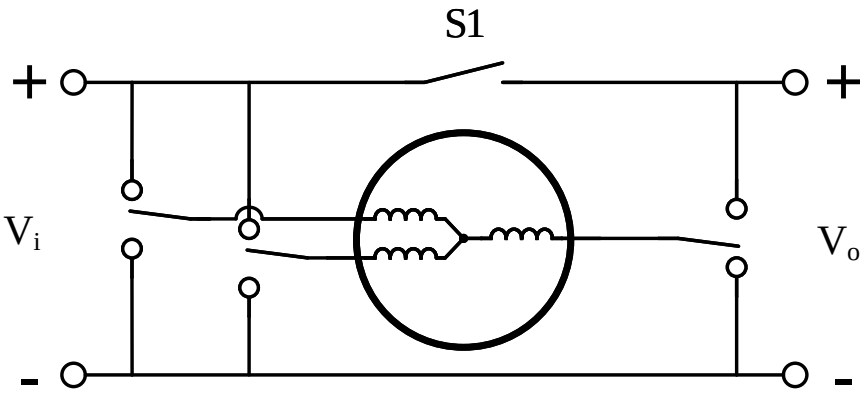

Figure 4.10: Voltage source inverter with split DC link.

Considering the wye-connected machine configuration in the context of a VSI, it can be seen that with the addition of one switch S_1, a non-inverting buck-boost converter is formed. S_1 disconnects one of the inverter phases, which is fundamentally a buck converter, from the input voltage. This results in a 180 degree rotation of the buck converter, or an inversion of source and load, producing a boost converter. The boost converter is now cascaded with the first two parallel phases (buck converters), resulting in the non-inverting buck-boost topology.

The non-inverting buck-boost converter formed with the addition of a single relay is a potential integrated solution to the second challenge of controlling the flow of current irrespective of input and output voltage magnitudes. It is only capable of accepting a DC input however and would require an external rectifier circuit should the input be AC.

4.2.3 SPDT Implementation

The SPDT switch is implemented with power semiconductors, the exact configuration of which depends on the power flow requirements. Three SPDT switch implementations

in the context of the three-terminal cell are shown in Figure 4.11.

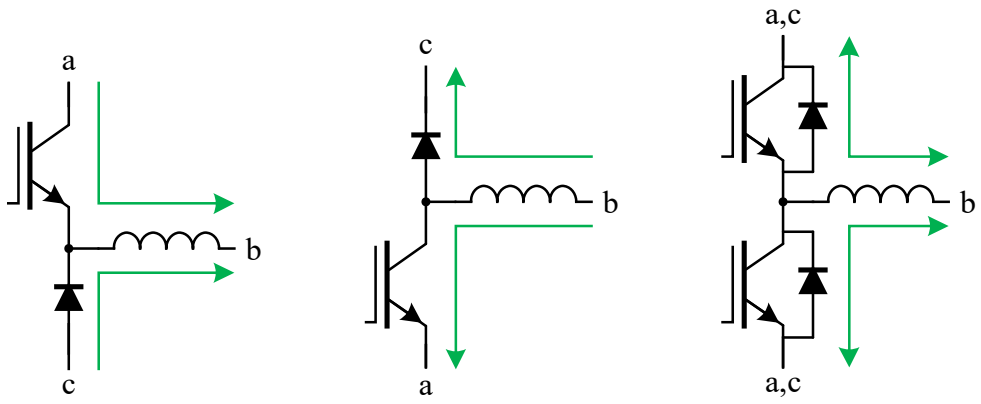

(a) Unidirectional buck SPDT implementation.

(b) Unidirectional boost SPDT implementation.

(c) Superimposed buck & boost SPDT implementation.

Figure 4.11: SPDT switch implementations.

Figure 4.11a shows a SPDT implementation typical of a unidirectional buck converter, in which current can only flow out of node b. Figure 4.11b shows the equivalent implementation for a unidirectional boost converter, in which current can only flow into node b. Finally Figure 4.11c shows the SPDT implementation resulting from superimposing the buck and boost implementations. Current can flow out of node b when operating as a buck converter, and into node b when operating as a boost converter. This implementation is therefore bidirectional which enables the inversion of source and load principle discussed previously. Evidently a three-phase VSI is implemented with three of these cells, effectively cascaded through the neutral point of the machine, facilitating bipolar voltages generation and bidirectional current flow.

Integrated converters can therefore be realized through the judicious application of relays and external components to the fundamental bidirectional three-terminal cells already present in any conventional VSI motor drive. While the function of the switching elements in the converter are the same between modes, the function of the

machine changes significantly. At this point, further analysis of the machine windings and their behaviour when repurposed as inductors is warranted.

4.3 Machine Model

To facilitate the design of any integrated converter taking advantage of the machine winding inductances, a model of those inductances should be developed. The model should be germane to the task at hand and avoid any complexity which may be necessary to model the machine as an electromechanical energy conversion device, but unnecessary when used as only an inductor. With this in mind, the standard stationary reference frame model of the IPMSM is derived. The model is further simplified for the case of a wye-connected machine with internal neutral point, resulting in a decoupled model of the phase inductances. The decoupled model greatly simplifies determination of the equivalent phase inductances for use in an integrated converter. Finally, the electromagnetic torque production of the machine is evaluated for two possible phase connection configurations suitable for application as an integrated inductor.

4.3.1 Magnetic Modelling

A three-phase permanent magnet synchronous machine (PMSM) consists of three sets of coils embedded in slots in the stator, and one or more permanent magnets attached to the rotor. In the case of an interior permanent magnet machine (IPMSM), the magnet is embedded inside the rotor, rather than attached to the surface of the rotor as in a surface permanent magnet machine (SPM). The stator and rotor are both

constructed from high permeability iron material. Figure 4.12 depicts a simplified three-phase IPMSM with a single magnet in the rotor. The stator phase magnetic axis are shown in black and the rotor direct and quadrature axis are shown in blue.

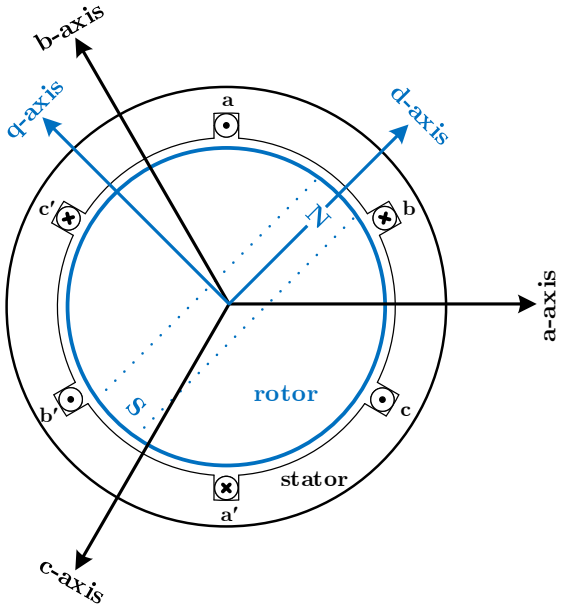

Figure 4.12: Simplified three-phase IPMSM.

The rotor d-axis is defined along the north magnetic pole of the permanent magnet, and the q-axis is 90 degrees ahead of the d-axis. The stator magnetic axis are displaced by 120 degrees and the windings are electrically connected in a wye configuration. Since the airgap between the stator and rotor is physically small compared to the radius of the rotor, it can be assumed that the flux across the airgap is constant. Additionally, the flux travels only in the radial direction across the airgap, as this is the lowest reluctance path between the stator and rotor.

A single concentrated winding for each phase, like that shown in Figure 4.12, if excited with a constant DC current, would produce an approximately constant magnetic field in the direction of the phase magnetic axis. If the stator were to be "unrolled" and the

field plotted on a linear axis, it would be depicted as a square wave. If the windings were instead distributed across multiple slots, the field would increase stepwise as each additional slot is crossed then decrease again. With a sufficient number of slots, the square wave field will become approximately sinusoidal. This is known as a distributed winding which is commonly employed in PMSMs [8].

Airgap Magnetomotive Force

Considering Ampère's law

$$\oint \mathbf{B} \cdot d\mathbf{l} = \mu I_{enc} \tag{4.1}$$

For a multi turn conductor, the enclosed current I_{enc} can be expressed as NI where N is the number of turns. This is also the definition of magnetomotive force (MMF) $\mathfrak{F}$, with unit ampere-turns:

$$\mathfrak{F} = NI \tag{4.2}$$

Consider the machine in Figure 4.13 in which only the sinusoidally distributed phase A winding is depicted. If it is assumed that flux travels only circumferentially in the stator back iron and radially in the airgap and rotor, evaluating (4.1) for the integration path shown in green can be written as a sum of each segment k in the path of length l_k with permeability μ_k

$$\sum_k \frac{Bl_k}{\mu_k} = \mathfrak{F}_{stator} + \mathfrak{F}_{rotor} + 2\mathfrak{F}_{airgap} = NI\cos\phi \tag{4.3}$$

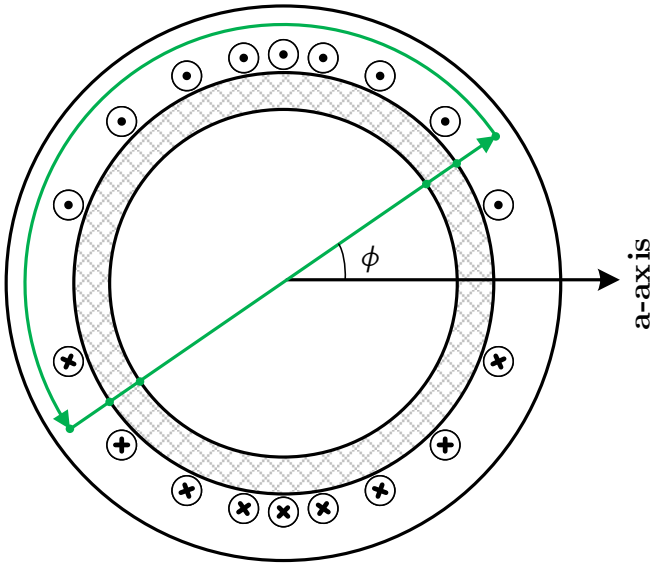

Figure 4.13: Integration path with sinusoidally distributed windings for phase A.

From (4.3) it is clear that the MMF is inversely proportional to the permeability of the material μ. Since the rotor and stator iron have a permeability several thousand times higher than that of the airgap, the simplifying assumption can be made that all of the MMF is concentrated in the airgap, and the MMF drops in the iron are negligible [168]. This is somewhat analogous with how the voltage drops in copper wires are often neglected in electric circuit analysis. It is assumed that magnetic saturation does not occur. As the integration path rotates with angle ϕ from the phase A magnetic axis, the sinusoidal distribution of the windings will cause the total enclosed current to vary with $\cos\phi$.

The MMF can be separated into two parts, one which describes the excitation and one which describes the physical distribution of the conductors which link magnetic flux, known as the winding function. For phase A the excitation is simply the current

i_a and the winding function is

$$w_a(\phi) = \frac{N}{2}\cos\phi \tag{4.4}$$

Phase B and C are described similarly, with their winding functions phase shifted by 120 degrees. The resulting airgap MMFs for each phase are

$$\begin{aligned}
\mathfrak{F}_a(\phi) &= \frac{Ni_a}{2}\cos(\phi) \\
\mathfrak{F}_b(\phi) &= \frac{Ni_b}{2}\cos(\phi - 2\pi/3) \\
\mathfrak{F}_c(\phi) &= \frac{Ni_c}{2}\cos(\phi + 2\pi/3)
\end{aligned}$$

The total airgap MMF can be determined by summing the individual phase contributions. Assuming the phases are excited by a balanced three-phase set of currents with amplitude I:

$$\begin{aligned}
i_a &= I\cos(\omega t) \\
i_b &= I\cos(\omega t - 2\pi/3) \\
i_c &= I\cos(\omega t + 2\pi/3)
\end{aligned}$$

where ω is the electrical frequency, the resultant airgap MMF is

$$\mathfrak{F}_{total} = \frac{3}{2}NI\cos(\phi - \omega t) \tag{4.5}$$

Note that (4.5) is a solution to the one dimensional wave equation, describing a rotating MMF wave at speed ω. A set of three-phase sinusoidally distributed windings, when excited with a balanced three-phase set of sinusoidal currents, is equivalent to a single

rotating sinusoidal winding with a MMF 1.5 times larger.

4.3.2 Voltage Equation

The phase voltage can be fundamentally written as a sum of the resistive component $\mathbf{R}$ and an induced component from a time varying flux linkage $\boldsymbol{\lambda}$.

$$\mathbf{V} = \mathbf{R}\mathbf{i} + \frac{d\boldsymbol{\lambda}}{dt} \tag{4.6}$$

The flux linkage is a function of both rotor position θ and phase currents $\mathbf{i}$. In a permanent magnet machine, the flux linkage is created by current flowing in the stator windings as well as from the rotor permanent magnet flux ψ_f. For an IPMSM, the stator inductance $\mathbf{L}$ varies as a function of rotor position θ, due to the salient rotor structure. The permanent magnet flux varies as a function of rotor position in all PM machines.

$$\boldsymbol{\lambda}(i,\theta) = \mathbf{L}(\theta)\mathbf{i} + \boldsymbol{\psi_f}(\theta) \tag{4.7}$$

By the chain rule, the derivative of the flux linkage expression can be written as

$$\frac{d\lambda(i,\theta)}{dt} = \frac{\partial\lambda(i)}{di}\frac{di}{dt} + \frac{\partial\lambda(\theta)}{d\theta}\frac{d\theta}{dt} \tag{4.8}$$

Evaluating (4.8) and noting that $d\theta/dt$ is the rotor speed ω:

$$\frac{d\boldsymbol{\lambda}}{dt} = \mathbf{L}(\theta)\frac{di}{dt} + \mathbf{i}\frac{d\mathbf{L}(\theta)}{d\theta}\omega + \frac{d\boldsymbol{\psi_f}(\theta)}{d\theta}\omega \tag{4.9}$$

The permanent magnet flux will be ignored for the remainder of the analysis, as it has no impact on the stator flux other than through introducing rotor saliency, which is a consequence of the magnetic material itself, rather than the magnet flux. The permanent magnet flux can be added in again after the stator analysis in complete.

4.3.3 Stator Inductance

To proceed further, the stator inductance matrix **L** must be determined. The matrix will be in the form

$$\mathbf{L} = \begin{bmatrix} L_{aa} & L_{ab} & L_{ac} \\ L_{ba} & L_{bb} & L_{bc} \\ L_{ca} & L_{cb} & L_{cc} \end{bmatrix} \tag{4.10}$$

where the diagonal elements are the phase self inductances and the off diagonal elements are the mutual inductances. The matrix will be symmetric as the coupling between two windings is the same in both directions, e.g $L_{ac} = L_{ca}$ [168].

Mutual leakage inductance is neglected entirely, and self leakage inductance is neglected for this section of the analysis. Self leakage inductance will not depend on rotor position and therefore can be added after the position dependent inductances have been established.

Figure 4.14 illustrates how the stator inductances will depend on the rotor position θ. When the rotor d-axis is aligned with the phase A axis, $\theta = 0$, the phase A flux will pass through the permanent magnets embedded in the rotor. Permanent magnets have a relative permeability close to that of air, significantly lower than that of the rotor iron. The flux in Figure 4.14a experiences a higher reluctance than the flux in 4.14b,

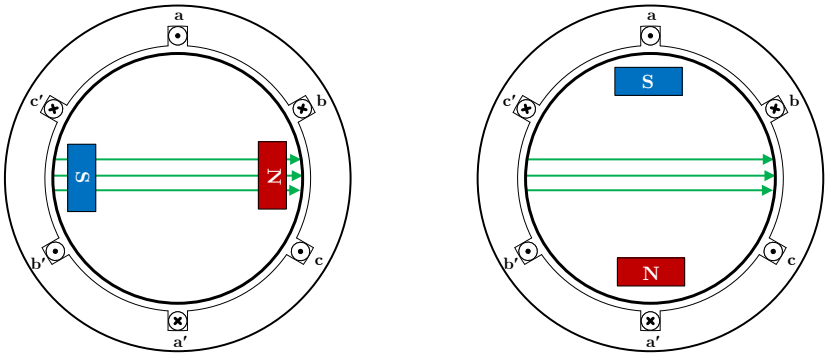

(a) Rotor d-axis aligned with phase A magnetic axis, $\theta = 0$

(b) Rotor q-axis aligned with phase A magnetic axis, $\theta = \frac{\pi}{2}$

Figure 4.14: Phase A flux passing through a rotor with interior permanent magnets.

increasing the effective airgap. Inductance is inversely proportional to reluctance $\mathfrak{R}$:

$$L = \frac{N^2}{\mathfrak{R}} \tag{4.11}$$

Therfore we can say the phase inductance varies between a minimum at $\theta = 0$ to a maximum at $\theta = \frac{\pi}{2}$ and returns to a minimum at $\theta = \pi$, thus varying as

$$L_{aa} = L_A + L_B \cos 2\theta \tag{4.12}$$

where L_A is the average value of the inductance and L_B is the amplitude of the sinusoidally varying component. A similar argument can be made to define the effective airgap length at the phase A magnetic axis for a given rotor angle, $g(\theta)$. Since reluctance is proportional to length l:

$$\mathfrak{R} = \frac{l}{\mu A} \tag{4.13}$$

and inductance is inversely proportional to reluctance, then $l \propto L^{-1}$, so the effective

airgap function must be a reciprocal form of (4.12)

$$g(\theta) = \frac{1}{\alpha_1 - \alpha_2 \cos 2\theta} \tag{4.14}$$

where α_1 and $alpha_2$ are the inverse average and sinusoidally varying components of the effective airgap length. L_{bb} and L_{cc} are determined similarly with their respective phase shifts

$$L_{bb} = L_A + L_B \cos 2(\theta - \frac{2\pi}{3})$$
$$L_{cc} = L_A + L_B \cos 2(\theta + \frac{2\pi}{3})$$

The mutual inductance between windings x and y, L_{xy}, is defined as

$$L_{xy} = \frac{\lambda_x|_{\text{due to } i_y}}{i_y} \tag{4.15}$$

To evaluate this, the flux from winding x linking to winding y must be determined. Integrating over the interior surface of the stator, with the incremental area $lrd\phi$ where l is the axial length of the machine, r is the radius of the inner stator surface, ϕ is some angle along the stator from the phase A magnetic axis, and $d\phi$ is the incremental angle:

$$\lambda_x = \int_0^{2\pi} B_y(\phi) w_x(\phi) lr d\phi \tag{4.16}$$

where $w_x(\phi)$ is the winding function for phase x. The B field due to current in winding y can be determined from the winding y MMF, which can also be written in terms of its winding function $w_y(\phi)$.

$$\mathfrak{F}_y(\phi) = w_y(\phi) i_y \tag{4.17}$$

From (4.3) we can write B in terms of the MMF and the effective airgap. Note that the effective airgap function is defined in terms of the rotor angle relative to the phase A magnetic axis and can also be determined at an arbitrary stator position ϕ with given rotor angle θ as $g(\phi - \theta)$.

$$B_y(\phi) = \frac{\mu_0 \mathfrak{F}_y(\phi)}{g(\phi - \theta)} = \frac{\mu_0}{g(\phi - \theta)} w_y(\phi) i_y \tag{4.18}$$

Substituting (4.18) into (4.16):

$$\lambda_x = \left(\mu_0 r l \int_0^{2\pi} \frac{w_x(\phi) w_y(\phi)}{g(\phi - \theta)} d\phi \right) i_y \tag{4.19}$$

The mutual inductance L_{xy} is therefore

$$L_{xy} = \frac{\lambda_x}{i_y} = \mu_0 r l \int_0^{2\pi} w_x(\phi) w_y(\phi) (\alpha_1 - \alpha_2 \cos(2\phi - 2\theta)) d\phi \tag{4.20}$$

Evaluating for example L_{ab} which have winding functions

$$\begin{aligned} w_a(\phi) &= \frac{N}{2} \cos \phi \\ w_b(\phi) &= \frac{N}{2} \cos \left(\phi - \frac{2\pi}{3} \right) \end{aligned}$$

Results in

$$L_{ab} = -\frac{1}{2} \left(\frac{N}{2} \right)^2 \phi \mu_0 r l \alpha_1 + \frac{1}{2} \left(\frac{N}{2} \right)^2 \pi \mu_0 r l \alpha_2 \cos 2(\theta - \frac{\pi}{3}) \tag{4.21}$$

The self inductance can also be determined from (4.20) by evaluating the flux linkage

of the winding with itself, i.e setting $y = x$.

$$L_{aa} = \left(\frac{N}{2}\right)^2 \phi\mu_0 rl\alpha_1 + \frac{1}{2}\left(\frac{N}{2}\right)^2 \pi\mu_0 rl\alpha_2 \cos 2\theta \tag{4.22}$$

Relating (4.22) back to the originally assumed form (4.12), L_A and L_B can now be defined as

$$L_A = \left(\frac{N}{2}\right)^2 \phi\mu_0 rl\alpha_1$$
$$L_B = \frac{1}{2}\left(\frac{N}{2}\right)^2 \pi\mu_0 rl\alpha_2$$

The mutual inductance (4.21) can also be expressed in terms of L_A and L_B:

$$L_{ab} = -\frac{1}{2}L_A + L_B \cos 2(\theta - \frac{\pi}{3}) \tag{4.23}$$

The same procedure can be followed to determine the remainder of the inductance matrix [168]:

$$\mathbf{L} = \begin{bmatrix} L_A + L_B\cos 2\theta & -\frac{1}{2}L_A + L_B\cos 2(\theta - \frac{\pi}{3}) & -\frac{1}{2}L_A + L_B\cos 2(\theta + \frac{\pi}{3}) \\ -\frac{1}{2}L_A + L_B\cos 2(\theta - \frac{\pi}{3}) & L_A + L_B\cos 2(\theta - \frac{2\pi}{3}) & -\frac{1}{2}L_A + L_B\cos 2(\theta + \pi) \\ -\frac{1}{2}L_A + L_B\cos 2(\theta + \frac{\pi}{3}) & -\frac{1}{2}L_A + L_B\cos 2(\theta + \pi) & L_A + L_B\cos 2(\theta + \frac{2\pi}{3}) \end{bmatrix} \tag{4.24}$$

The resistance matrix $\mathbf{R}$ is a function of the individual winding geometry and can be simply expressed since all three windings are identical

$$\mathbf{R} = \begin{bmatrix} r_s & 0 & 0 \\ 0 & r_s & 0 \\ 0 & 0 & r_s \end{bmatrix} \tag{4.25}$$

4.3.4 DQ Transform

The inductance matrix (4.24) is obviously dependent on the rotor angle and is therefore time varying. The phase current vector **i** in the phase voltage equation (4.6) is also time varying. In many cases, analysis can be greatly simplified by transforming the voltage equation from the stationary stator reference frame into a rotating rotor reference frame. A suitable transformation is the dq0 transform which decomposes the a, b, c axis into a direct, quadrature and zero sequence component, rotating at a given speed. The transformation matrix is defined as:

$$\mathbf{K}_s = \frac{2}{3}\begin{bmatrix} \cos\theta & \cos(\theta - \frac{2\pi}{3}) & \cos(\theta + \frac{2\pi}{3}) \\ \sin\theta & \sin(\theta - \frac{2\pi}{3}) & \sin(\theta + \frac{2\pi}{3}) \\ \frac{1}{2} & \frac{1}{2} & \frac{1}{2} \end{bmatrix} \tag{4.26}$$

and its inverse is:

$$\mathbf{K}_s^{-1} = \begin{bmatrix} \cos\theta & \sin\theta & 1 \\ \cos(\theta - \frac{2\pi}{3}) & \sin(\theta - \frac{2\pi}{3}) & 1 \\ \cos(\theta + \frac{2\pi}{3}) & \sin(\theta + \frac{2\pi}{3}) & 1 \end{bmatrix} \tag{4.27}$$

Transforming the inductance matrix (4.24) into the rotor reference frame results in a significant simplification

$$\mathbf{L}_{dq} = \mathbf{K}_s\mathbf{L}\mathbf{K}_s^{-1} = \begin{bmatrix} \frac{3}{2}(L_A - L_B) & 0 & 0 \\ 0 & \frac{3}{2}(L_A + L_B) & 0 \\ 0 & 0 & 0 \end{bmatrix} \tag{4.28}$$

Defining $L_d = \frac{3}{2}(L_A - L_B)$ and $L_q = \frac{3}{2}(L_A + L_B)$, or equivalently $L_A = \frac{L_d+L_q}{3}$ and $L_B = \frac{L_q-L_d}{3}$, the inductance matrix in the dq reference frame can be written as

$$\mathbf{L}_{dq} = \begin{bmatrix} L_d & 0 & 0 \\ 0 & L_q & 0 \\ 0 & 0 & 0 \end{bmatrix} \tag{4.29}$$

In a synchronous machine, the rotor rotates at the same speed as the airgap MMF, the speed of which is determined by the phase currents. Therefore the phase currents can also be transformed into the same rotating reference frame. Considering the phase current vector

$$\mathbf{i} = \begin{bmatrix} i_a \\ i_b \\ i_c \end{bmatrix} = \begin{bmatrix} I\cos(\theta+\phi) \\ I\cos(\theta-2\pi/3+\phi) \\ I\cos(\theta+2\pi/3+\phi) \end{bmatrix} \tag{4.30}$$

where ϕ is an arbitrary phase shift of the current from the rotor angle θ. Recall θ is defined as the angle between the rotor d-axis and the phase A magnetic axis. Transforming to the dq reference frame results in:

$$\mathbf{K}_s\mathbf{i} = \begin{bmatrix} I\cos(\phi) \\ I\sin(\phi) \\ 0 \end{bmatrix} = \begin{bmatrix} i_d \\ i_q \\ i_0 \end{bmatrix} \tag{4.31}$$

4.3.5 Voltage Equation in Rotating Reference Frame

The full stator voltage equation can now be transformed into the rotating reference frame. Restating (4.6) with explicit subscripts indicating the reference frame of each

quantity

$$\mathbf{V}_{abc} = \mathbf{R}i_{abc} + \frac{d}{dt}\boldsymbol{\lambda}_{abc} \tag{4.32}$$

$$= \mathbf{R}\mathbf{K}_s^{-1}\mathbf{i}_{dq0} + \frac{d}{dt}(\mathbf{K}_s^{-1}\boldsymbol{\lambda}_{dq0}) \tag{4.33}$$

Changing reference frames, and noting that $\mathbf{R}$ is invariant under the transform

$$\mathbf{v}_{dq0} = \mathbf{K}_s\mathbf{v}_{abc} \tag{4.34}$$

$$= \mathbf{R}\mathbf{i}_{dq0} + \mathbf{K}_s\frac{d}{dt}(\mathbf{K}_s^{-1}\boldsymbol{\lambda}_{dq0}) \tag{4.35}$$

expanding the second term

$$\mathbf{K}_s\frac{d}{dt}(\mathbf{K}_s^{-1}\boldsymbol{\lambda}_{dq0}) = \mathbf{K}_s\left[\left(\frac{d}{dt}\mathbf{K}_s^{-1}\right)\boldsymbol{\lambda}_{dq0} + \mathbf{K}_s^{-1}\frac{d}{dt}\boldsymbol{\lambda}_{dq0}\right] \tag{4.36}$$

which can be further simplified since

$$\mathbf{K}_s\frac{d}{dt}\mathbf{K}_s^{-1} = \omega\begin{bmatrix}0 & -1 & 0\\ 1 & 0 & 0\\ 0 & 0 & 0\end{bmatrix} \tag{4.37}$$

where $\omega = \frac{d\theta}{dt}$. The stator voltage equation in the dq0 frame is:

$$\mathbf{v}_{dq0} = \mathbf{R}\mathbf{i}_{dq0} + \omega\begin{bmatrix}-\lambda_q\\ \lambda_d\\ 0\end{bmatrix} + \frac{d}{dt}\boldsymbol{\lambda}_{dq0} \tag{4.38}$$

where

$$\boldsymbol{\lambda}_{dq0} = \begin{bmatrix} \lambda_d \\ \lambda_q \\ \lambda_0 \end{bmatrix} = \mathbf{K}_s \mathbf{L} \mathbf{K}_s^{-1} \mathbf{i}_{dq0} = \mathbf{L}_{dq} \mathbf{i}_{dq0} \tag{4.39}$$

4.3.6 Zero Sequence Current

The zero sequence current i_0 represents any component in the phase current waveforms, such that they would not have an average value of zero. The current vector $\mathbf{i}$ in (4.30) is one such set of currents that has no zero sequence, however it can be further generalized. Looking at the transformation matrix $\mathbf{K}_s$, the condition for $i_0 = 0$ is only that $i_a + i_b + i_c = 0$. In a three-phase wye-connected machine with a floating neutral point, this is necessarily true based on a simple application of Kirchhoff's current law. Therefore the following holds for any i_b and i_c

$$\mathbf{K}_s \begin{bmatrix} -i_b - i_c \\ i_b \\ i_c \end{bmatrix} = \begin{bmatrix} i_d \\ i_q \\ 0 \end{bmatrix} \tag{4.40}$$

justifying the reduction from three current variables to two.

Another important consideration is that a zero sequence current can only arise as the result of a zero sequence voltage. In the case of a wye-connected machine with a floating neutral, a zero sequence voltage can exist, but since the neutral is floating it has infinite zero sequence impedance, so the voltage will not result in any current flow. A zero sequence voltage at the neutral point is common to all phases, and therefore does not appear in any line-to-line measurements of the phases.

4.3.7 Stator Model Decoupling

While the DQ reference frame is convenient in many cases for modeling of the machine itself, it can be challenging to implement the model in the context of external circuits connected to the machine, such as a voltage source inverter, which exists in the stator reference frame. A typical implementation would involve transforming the stationary frame phase voltages to the rotating reference frame, solving for the d and q axis currents, then transforming them back to the stationary reference frame and applying them as a set of voltage controlled current sources in the circuit model. Voltage controlled current sources present a challenge in the context of switching circuits, as the solver must ensure the current is continuous across switching instants. For this reason it is often preferable to implement the machine model in the stator reference frame when interfacing it with switching circuits [169]. This is known as a voltage behind reactance (VBR) model. While the inductance matrix (4.24) is suitable for parameterizing the reactance, further simplification can be achieved by imposing some constraints.

More precisely, the goal is to find a diagonal form of the $\mathbf{L}$ matrix that results in the same model behaviour under the following constraints [170]:

1. There is no path for zero sequence current to flow: $i_0 = 0$

2. The neutral point of the machine is floating and inaccessible, so any zero sequence voltage cannot be measured: v_0 does not have any influence outside of the machine model

As stated in (4.39) flux linkage in the dq0 frame is

$$\begin{bmatrix} \lambda_d \\ \lambda_q \\ \lambda_0 \end{bmatrix} = \begin{bmatrix} L_d & 0 & 0 \\ 0 & L_q & 0 \\ 0 & 0 & 0 \end{bmatrix} \begin{bmatrix} i_d \\ i_q \\ i_0 \end{bmatrix} \tag{4.41}$$

Examining the right hand side of the equation, since $i_0 = 0$, the entries in the last column of the $\mathbf{L}_{dq}$ matrix have no effect on the flux linkage. These three entries can therefore be altered to arbitrary nonzero values with no physical effect, which can further the goal of finding a diagonal $\mathbf{L}$ matrix. Following this logic also for the last row of the $\mathbf{L}_{dq}$ matrix, if the first two entries L_{31} and L_{32} were non-zero, a zero sequence flux λ_0 would arise:

$$\lambda_0 = L_{31} i_d + L_{32} i_q \tag{4.42}$$

resulting in a zero sequence voltage v_0:

$$v_0 = \frac{d\lambda_0}{dt} \tag{4.43}$$

which can be safely ignored because of constraint (2). The problem can now be formulated in terms of a new matrix $\mathbf{L}'_{dq}$ with unknown elements that must be determined such that the matrix, when transformed into the stationary reference frame, is diagonal.

$$\mathbf{L}'_{dq} = \begin{bmatrix} L_d & 0 & L_{13} \\ 0 & L_q & L_{23} \\ L_{31} & L_{32} & L_{33} \end{bmatrix} \tag{4.44}$$

Transforming into the stationary reference frame and equating the off diagonal elements to zero results in a system of six equations and five unknowns (L_{13}, L_{23}, L_{31}, L_{32} and L_{33}):

$$\mathbf{K}_s^{-1}\mathbf{L}'_{dq}\mathbf{K}_s = \begin{bmatrix} L_a & 0 & 0 \\ 0 & L_b & 0 \\ 0 & 0 & L_c \end{bmatrix} \tag{4.45}$$

Solving the system and much algebra results in the following $\mathbf{L}'_{dq}$ matrix

$$\mathbf{L}'_{dq} = \begin{bmatrix} L_d & 0 & (L_d - L_q)\cos 3\theta \\ 0 & L_q & (L_q - L_d)\sin 3\theta \\ \frac{(L_d - L_q)}{2}\cos 3\theta & \frac{(L_q - L_d)}{2}\sin 3\theta & \frac{L_d + L_q}{2} \end{bmatrix} \tag{4.46}$$

Which, in the stationary reference frame, produces a diagonal matrix $\mathbf{L}'$:

$$\mathbf{L}' = \mathbf{K}_s^{-1}\mathbf{L}'_{dq}\mathbf{K}_s =$$

$$\begin{bmatrix} \frac{L_d+L_q}{2} + (L_d - L_q)\cos 2\theta & 0 & 0 \\ 0 & \frac{L_d+L_q}{2} + (L_d - L_q)\cos 2(\theta - \frac{2\pi}{3}) & 0 \\ 0 & 0 & \frac{L_d+L_q}{2} + (L_d - L_q)\cos 2(\theta + \frac{2\pi}{3}) \end{bmatrix} \tag{4.47}$$

Subject to the two defined constraints, this matrix produces a model of the machine in the stationary reference frame equivalent to that of the full matrix (4.24).

4.4 Machines in Integrated Converters

Returning to the subject of integrated converters, the details of the available machine winding inductance can now be determined with the motor model. The primary considerations are the magnitude of the inductance itself, which dictates the integrated converter design and performance, and the potential for torque production during operation of the integrated converter.

4.4.1 Inductance Analysis

The decoupled model of the machine greatly simplifies the analysis of equivalent inductances for the purposes of designing integrated converters. It should be noted that the model no longer has a direct physical meaning. Indeed the inductances in (4.47) can be negative at some values of θ if $L_d < L_q/3$. The previously neglected leakage inductance can be added to the diagonal terms of (4.47) if desired, and depending on the machine geometry, may form a significant portion of the overall phase inductance. The leakage inductance does not have any effect on torque production.

Two possible motor winding configurations suitable for integrated converters using a standard wye-connected machine with internal neutral point will be analyzed. The parallel configuration uses all three windings in the machine, with two of the windings connected in parallel and the third in series, as shown in 4.15a. The series configuration uses only two of the windings, with the third left disconnected or open circuit, as shown in 4.15b.

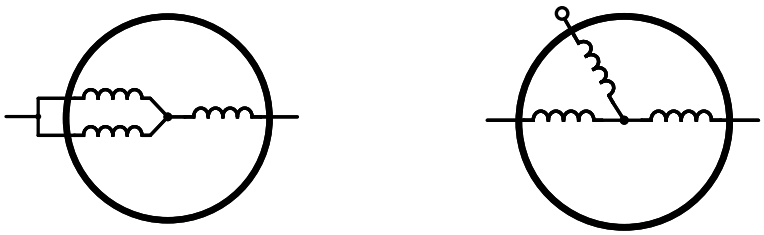

(a) Parallel configuration. (b) Series configuration.

Figure 4.15: Wye-connected machine winding configurations for integrated topologies.

Parallel Configuration

The equivalent total inductance is

$$L_{par} = L_a + L_b \parallel L_c \tag{4.48}$$

$$= \frac{3L_dL_q}{L_d + L_q + (L_q - L_d)\cos 2\theta} \tag{4.49}$$

Series Configuration

The equivalent total inductance is

$$L_{ser} = L_a + L_b \tag{4.50}$$

$$= L_d + L_q + (L_d - L_q)\cos\left(2\theta - \frac{\pi}{3}\right) \tag{4.51}$$

To compare the two configurations, L_{par} and L_{ser}, it is helpful to define the saliency ratio χ

$$\chi = \frac{L_q}{L_d} \tag{4.52}$$

An evaluation of the the average, maximum and minimum inductances in the range $\theta = [0, \pi)$ for L_{par} and L_{ser}, plotted as function of χ is shown in Figure 4.16.

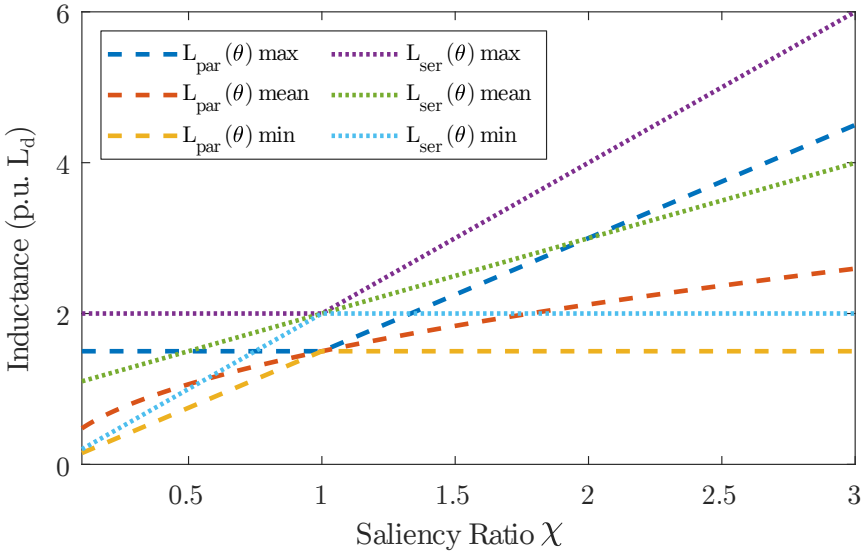

Figure 4.16: Per unit inductance (relative to L_d) of series and parallel winding configurations.

Evidently the series configuration results in a higher equivalent inductance for all saliency ratios. The remaining consideration in selecting a configuration is the torque production, which is an undesirable characteristic for an inductor. Fortunately, there exists specific rotor positions in which the electromagnetic torque is zero. The torque production as a result of the stator flux from the series and parallel inductor configurations of the machine will be considered in the next section.

4.4.2 Torque Production

The electromagnetic torque τ_e can be determined from co-energy considerations. For any electromagnetic system, the stored energy W can be calculated by integrating the current required to produce a given flux linkage

$$W = \int_0^{\lambda_1} i(\lambda) d\lambda \tag{4.53}$$

Equivalently (for linear systems), the co-energy W' can be calculated by integrating the flux linkage with respect to current

$$W' = \int_0^{i_1} \lambda(i) di \tag{4.54}$$

From the flux linkage expression (4.7), defining the PM flux as

$$\boldsymbol{\psi_f}(\theta) = \psi_0 \begin{bmatrix} \cos(\theta) \\ \cos(\theta - \frac{2\pi}{3}) \\ \cos(\theta + \frac{2\pi}{3}) \end{bmatrix} \tag{4.55}$$

the co-energy can be evaluated as

$$\mathbf{W}' = \int_0^i \mathbf{iL}(\theta) di + \int_0^i \boldsymbol{\psi_f}(\theta) di \tag{4.56}$$

$$= \frac{1}{2}\mathbf{i}^T \mathbf{L}(\theta)\mathbf{i} + \mathbf{i}^T \boldsymbol{\psi_f}(\theta) \tag{4.57}$$

If the diagonalized inductance matrix (4.47) is used, the torque contribution from each phase can be determined individually by noting the following power relationship and solving for the torque:

$$P = \tau_e \omega = \frac{dW'}{dt} \tag{4.58}$$

$$\frac{dW'}{dt} = \frac{1}{2} i^2 \frac{dL}{d\theta}\omega + i\frac{d\psi_f}{d\theta}\omega \tag{4.59}$$

$$\tau_e = \frac{1}{2} i^2 \frac{dL}{d\theta} + i\frac{d\psi_f}{d\theta} \tag{4.60}$$

Solving for each phase's torque contribution:

$$\tau_{ea} = i_a^2(L_q - L_d)\sin 2\theta - i_a\psi_0 \sin\theta \tag{4.61}$$

$$\tau_{eb} = i_b^2(L_q - L_d)\sin 2(\theta - \frac{2\pi}{3}) - i_b\psi_0 \sin(\theta - \frac{2\pi}{3}) \tag{4.62}$$

$$\tau_{ec} = i_c^2(L_q - L_d)\sin 2(\theta + \frac{2\pi}{3}) - i_c\psi_0 \sin(\theta + \frac{2\pi}{3}) \tag{4.63}$$

The total electromagnetic torque can now be evaluated for each winding configuration.

Parallel Configuration

Assuming that the average currents are split evenly between the two paralleled windings such that

$$i_b = i_c = -\frac{i_a}{2} \tag{4.64}$$

The torque is

$$\tau_e = \frac{3}{4}i_a^2(L_q - L_d)\sin(2\theta) - \frac{3}{2}i_a\psi_0 \sin\theta \tag{4.65}$$

which is zero for $\theta = n\pi, n \in \mathbb{Z}$

Series Configuration

In this configuration, $i_b = -i_a$ and $i_c = 0$. The torque is

$$\tau_e = i_a^2(Lq - Ld)\sin(2\theta + \frac{\pi}{3}) - \sqrt{3}i_a\psi_0 \sin(\theta + \frac{\pi}{6}) \tag{4.66}$$

which is zero for $\theta = n\pi - \frac{\pi}{6}, n \in \mathbb{Z}$

4.5 Conclusion

In this chapter, a theoretical basis for the development of integrated charger topologies is established. By breaking down any converter circuit into its fundamental three terminal cells, it becomes apparent how converters can be transformed and cascaded to achieve new conversion functionality. The procedure is applied to the three-phase VSI as the basis for providing integrated charging functionality in an EV.

While the functionality of the semiconductor switches remains essentially unchanged between the driving and charging modes, the role of the electric machine is entirely different. A decoupled stator reference frame model of an IPMSM is developed to facilitate analysis of the electric machine in the charging mode. The winding inductance and torque production during charging are quantified through application of the model. The existence of zero torque conditions is established, indicating the suitability of the machine windings to be used as an inductor in the integrated converter circuit.

Chapter 5

Integrated Charger for Switched Reluctance Machines

5.1 Introduction

SRMs have been proposed as an alternative to the PM and induction machines commonly used in electrified powertrains today. As discussed in Chapter 3, they benefit from a simple and low cost construction which does not require any permanent magnets or conductors on the rotor. While SRMs have not yet been widely adopted in electrified powertrains due to challenges with torque ripple and acoustic noise, recent research has begun to address these challenges and demonstrate suitability for powertrain applications [122, 126, 171]. The concentrated winding structure of the machine stator allows each phase to be isolated which presents new opportunities for integrated charger topologies compared to traditional wye or delta connected

three-phase machines.

In this chapter, a new IBC topology is proposed based on a four-phase asymmetric bridge converter and SRM. The topology is capable of power factor corrected three phase charging and both buck and boost output voltage control. No modifications to the machine are required while a limited number of additional inverter components are added. An equivalent-circuit based model of the machine is developed to facilitate investigation of the integrated charger performance. A control strategy for the charging mode is developed. The proposed topology is demonstrated through simulation of two distinct three-phase grid based charging applications.

Several IBC topologies have been proposed based on SRM drives with asymmetric bridge converters. Generally, the converter is re-purposed in the charging mode to accomplish AC mains rectification, DC to DC voltage conversion, or both. An interleaved DC/DC converter for battery charging is proposed in [172] using a four-phase SRM and asymmetric bridge converter. A similar topology with a three-phase buck type rectifier frontend is presented in [173]. To achieve PFC operation, additional line filter inductors are now required and the buck type rectifier requires six switches and 12 diodes. In [174] an IBC topology is proposed which integrates both PFC single-phase mains rectification and DC/DC conversion for a three-phase SRM drive. In the charging mode, two phases of the drive are used as a PFC boost converter while the third phase is used as a buck-boost converter. Further examples of SRM based IBC topologies also exist in which the machine windings are configured to have an accessible midpoint [160, 166, 175]. This can prevent torque production during charging, however a specially configured machine is now required. Additional SRM based IBC topologies are presented in Chapter 3. The previously proposed topologies

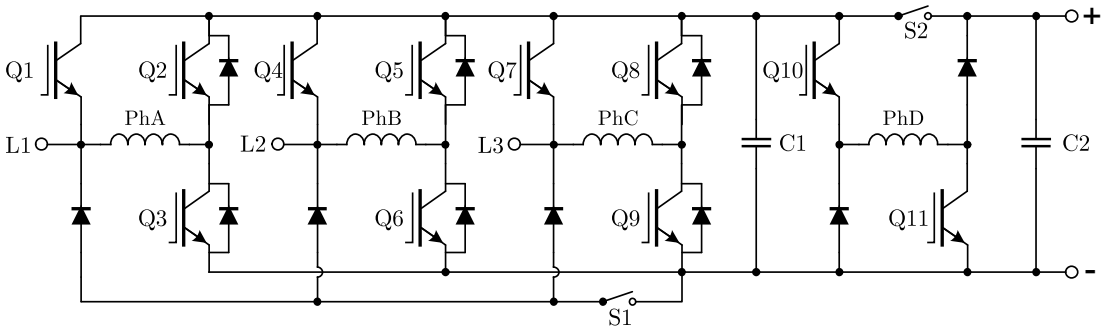

Figure 5.1: Asymmetric plus half bridge (A+HB) converter.

are either limited to single-phase mains or operate only as DC/DC converters, requiring additional rectifier frontends for charging from an AC grid source. Specifically, when compared with existing SRM based three-phase IBC topologies, the proposed topology requires less non-integrated semiconductor components, and no additional magnetic components.

5.2 Proposed Topology

To achieve charging from a three-phase grid with integrated output voltage regulation, a new topology is proposed which operates as a four-phase asymmetric bridge converter in the motoring mode and as a three-phase boost rectifier with a buck-boost DC/DC converter in the charging mode. This topology, as shown in Fig. 5.1, will be denoted as the asymmetric plus half bridge (A+HB) converter due to each phase being constructed from an asymmetric half bridge leg and a standard half bridge leg. When compared with the four-phase asymmetric half bridge converter, the A+HB converter requires three additional IGBT switches, three additional diodes and two relays. This increased component count is justified however by the elimination of the discrete OBC module

in the vehicle.

Considering the SPDT switch implementations discussed in Chapter 4, the asymmetric bridge converter phases (Figure 3.1) are implemented with cascaded unidirectional buck and unidirectional boost SPDT cells. This allows generation of bipolar voltages, but unlike the conventional VSI implemented with bidirectional SPDT cells, only unidirectional currents. To enable interfacing with the AC grid which requires bidirectional currents, one of the cascaded SPDT implementations must be converted to bidirectional through the addition of an additional switch and diode. This is performed for the first three phases. For the final phase implementing the buck-boost converter, unidirectional current flow is acceptable for charging the battery and the phase can remain unchanged. To implement a bidirectional (V2G) converter, the final phase would require both legs to be bidirectional SPDT cells. By applying the principle of the three terminal-cell to a given inverter topology, it becomes clear which additional converters can be implemented and if any additional components may be required to achieve the required functionality.

In the motoring mode, relays S1 and S2 are closed, and only the antiparallel diodes of Q2, Q5 and Q8 are used as the IGBTs are held off. This effectively reduces the topology to the standard four-phase asymmetric bridge converter. In the charging mode, S1 and S2 are opened and Q1, Q4 and Q7 are held off. Terminals L1, L2 and L3 are connected to a three-phase grid supply and all current is forced through the motor winding inductance (PhA, PhB, PhC). In combination with switch/diode pairs Q2, Q3, Q5, Q6, Q8 and Q9, a three-phase boost rectifier topology is formed which can provide active power factor correction and DC output voltage regulation where the DC output voltage must be greater than the peak AC line voltage. The fourth

phase inductance (PhD) is used to form a non-inverting buck-boost converter which can regulate the current to the battery regardless of if the battery's voltage is above or below the peak AC line voltage.

5.3 Modeling

To determine the performance of the converter, both the converter and the machine must be modelled as the machine windings form an integral part of the converter topology. Due to the salient pole nature of a SR machine, the winding inductance varies significantly with the rotor position. In addition, the inductance will vary with applied current due to the saturation characteristics of the iron core. To model both of these effects in the context of the converter, an equivalent circuit model for the SR machine will be applied, parameterized with inductance profiles from electromagnetic finite element analysis (FEA) of the machine. The equivalent circuit model will be used to develop and validate the converter controls and also to predict the torque production of the machine in the charging mode.

5.3.1 Switched Reluctance Traction Machine

A four-phase 8/6 SR machine is selected to demonstrate the converter operation. Several examples of four-phase 8/6 SR machines have been proposed for traction applications [176–178]. This machine is not optimized as the machine design is not the focus of this work, but is representative of a typical inductance and torque profile for a four-phase SR traction machine. The machine parameters are given in Table 5.1.

Table 5.1: Switched reluctance traction machine parameters.

Parameter	Value
Stator poles	8
Rotor poles	6
Phases	4
Stack length	190 mm
Outer diameter	350 mm
Coil connection	Series
Coil turns	13
Peak torque	350 Nm
Base speed	2000 RPM
Max speed	4600 RPM
Power	70 kW

Two dimensional electromagnetic FEA, shown in Figure 5.2, is conducted on the machine model. Two 2D lookup tables (LUTs) of the flux linkage and torque, as a function of rotor position and current, are produced which will be used to parameterize the equivalent circuit model of the machine.

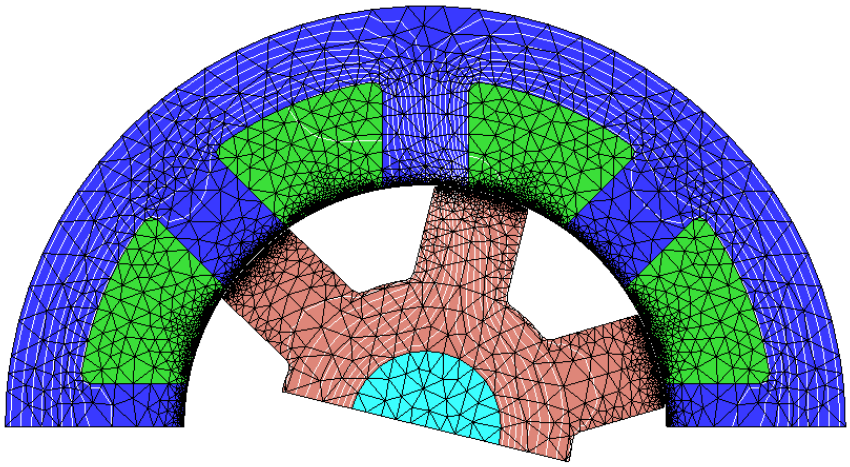

Figure 5.2: 2D electromagnetic FEA of 8/6 traction machine.

5.3.2 Equivalent Circuit Model

The equivalent circuit of a phase in a SR machine can fundamentally be written as a sum of the resistive component R and an induced component from a time-varying flux linkage λ.

$$V = iR + \frac{d\lambda}{dt} \tag{5.1}$$

The flux linkage can be expressed as the product of the phase inductance and the phase current, with the inductance as a function of rotor position θ: $\lambda = L(\theta)i$. Noting that $\omega = \frac{d\theta}{dt}$

$$V = iR + L(\theta)\frac{di}{dt} + i\frac{dL(\theta)}{d\theta}\omega \tag{5.2}$$

The equivalent circuit is therefore a constant resistance, variable inductance and speed dependent back EMF term, shown in Fig. 5.3. Note that this is a simplification as (5.2) does not consider that the flux linkage is a function of both rotor position and current, due to saturation effects. The neglected term is known as the incremental inductance [179]:

$$\ell(\theta, i) = i\frac{dL(\theta, i)}{di}\frac{di}{dt} \tag{5.3}$$

In the linear region of operation, dL/di is zero as the ratio λ/i is constant. In the motoring mode, at the unaligned position, dL/di is also zero as the effective permeability is low and saturation does not occur. Near the aligned position where saturation occurs, di/dt is only as large as the hysteresis band of the controller which is typically less than 5% to achieve good torque quality. In the charging mode, the machine is not operated in saturation. Therefore this simplification of the model is justified. Saturation effects are modelled through parameterizing the LUTs by both current and rotor position.

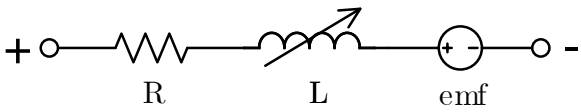

Figure 5.3: Equivalent phase circuit of an SRM.

The inductance LUT can be obtained by dividing the flux linkage by the current at each step. While the inductance LUT can be used to parameterize the variable inductance, the back EMF term is a function of the inductance derivative with respect to the mechanical rotor position. Since the inductance LUT is already available, it can be numerically differentiated to produce a second $dL(\theta)$ LUT. The L and dL LUTs are shown in Fig. 5.4.

The rotor torque contribution for a single phase as a function of phase current and rotor position can also be obtained from the FEA simulation as a LUT. The total torque contributions of all phases are summed and input to the mechanical model.

5.3.3 Mechanical Model

The rotor inertia and shaft friction are modelled as

$$\tau = J\frac{d\omega}{dt} + B\omega \tag{5.4}$$

where J is the rotor moment of inertia and B is the friction constant. The differential equation can be solved to determine the rotor speed for an applied torque, which is fed back to the electrical model.

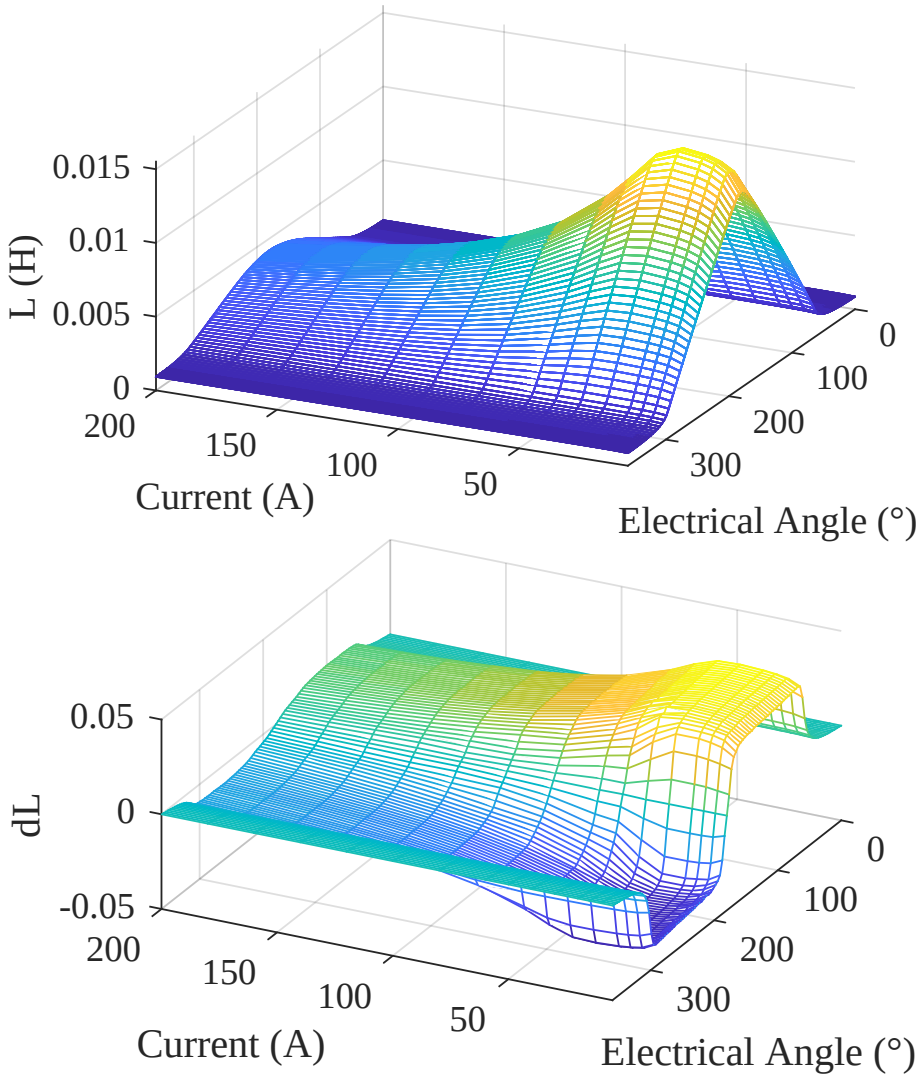

Figure 5.4: L and dL LUTs for the proposed SR traction machine.

5.4 Control Design

5.4.1 Motoring Mode

To validate the model and demonstrate the converter operation in the motoring mode, a hysteresis based soft-switching constant conduction angle controller is implemented [179]. The converter operates as a standard four phase asymmetric bridge converter and maintains a current within the hysteresis band through the conduction period. First a phase excitation signal is defined for each phase as

$$p(\theta) = \begin{cases} 1 & \text{if } \theta_{on} < \theta < \theta_{off} \\ 0 & \text{otherwise} \end{cases} \tag{5.5}$$

where θ_{on} and θ_{off} are the defined conduction angles and θ is the electrical angle of the phase. If the phase excitation signal evaluates to 1, the converter applies voltage to the phase to maintain the phase current within the hysteresis band:

$$v_{ph} = \begin{cases} V_{dc} & \text{if } i_{ph} < i_{min} \\ 0 & \text{if } i_{ph} > i_{max} \end{cases} \tag{5.6}$$

Finally after θ_{off}, during the demagnetization phase, $-V_{dc}$ is applied by the converter until i_{ph} drops to zero.

5.4.2 Charging Mode

In the charging mode, relays S1 and S2 are opened, resulting in a three-phase boost rectifier and buck-boost DC/DC converter. A critical function of the boost rectifier is

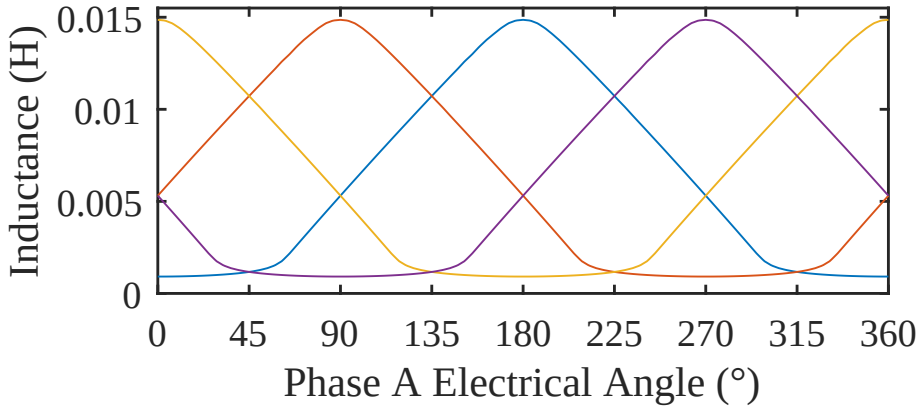

Figure 5.5: Phase inductances at $I = 40$ A over one electrical cycle.

to perform power factor correction to ensure the current drawn from the three-phase grid meets the relevant standards for harmonic content and displacement power factor [180]. Evaluating the phase inductances over an electrical cycle, it is clear from Fig. 5.5 that there is no rotor position in which any three of the four phases will present an equal inductance. Consequently, the phase inductances will create an inherently unbalanced load which must be actively compensated by the boost rectifier control. While the inductances are unbalanced, they are constant for a given rotor position which is maintained by a mechanical brake during charging, making the system effectively time invariant. The controller gains may be scheduled based on the rotor position and resulting inductances, or they may be designed such that acceptable performance is achieved across the range of possible inductances. Particular attention should be paid to the minimum inductance position, to avoid discontinuous operation or excessive current ripple.

Techniques for active power factor correction control of the three-phase boost rectifier (Fig. 5.6) are well established. Generally, the input phase voltages are measured and the grid phase angle θ_g is determined with a phase locked loop (PLL). The input

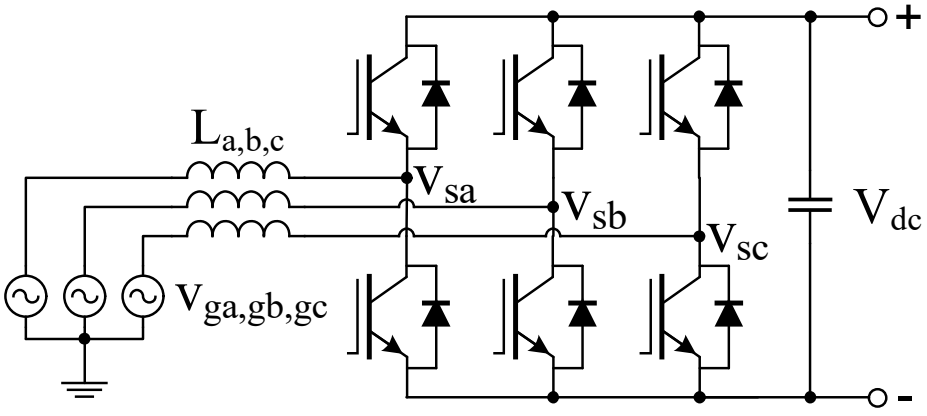

Figure 5.6: Three-phase boost rectifier topology.

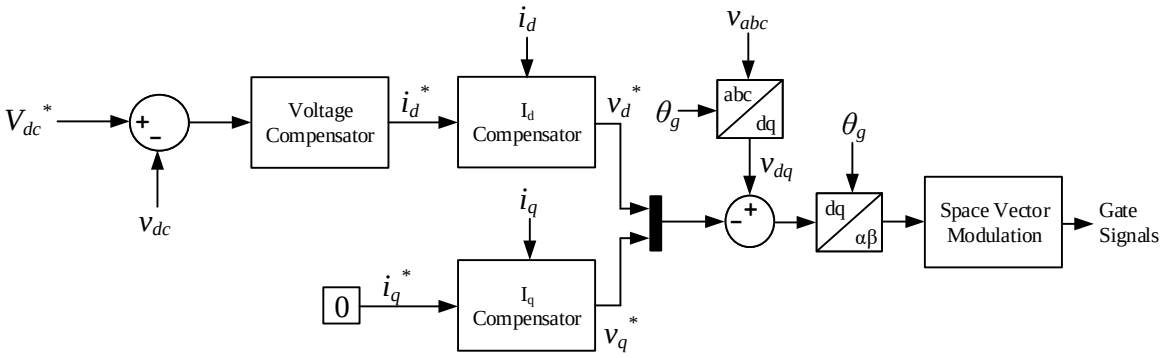

Figure 5.7: i_d and i_q control of a boost rectifier with outer voltage loop.

phase currents are also measured and transformed into the rotating reference frame. For a single boost rectifier feeding an ungrounded DC bus, there can be no zero sequence current, hence the direct and quadrature axis currents i_d and i_q are the control variables of interest. These quantities directly relate to the active and reactive power respectively, therefore to draw only real power, i_q must be 0 and i_d can be controlled to maintain a desired DC bus voltage at the output of the rectifier. The i_d and i_q control scheme with outer voltage loop is illustrated in Fig. 5.7. The voltage compensator is a standard proportional integral (PI) controller. The voltage at the rectifier terminals v_s is produced by space vector modulation (SVM) of the rectifier switches.

$$\begin{bmatrix} i_d \\ i_q \\ i_0 \end{bmatrix} = \frac{2}{3} \begin{bmatrix} \cos(\omega t) & \cos(\omega t - \frac{2\pi}{3}) & \cos(\omega t + \frac{2\pi}{3}) \\ -\sin(\omega t) & -\sin(\omega t - \frac{2\pi}{3}) & -\sin(\omega t + \frac{2\pi}{3}) \\ \frac{1}{2} & \frac{1}{2} & \frac{1}{2} \end{bmatrix} \begin{bmatrix} I_a \cos(\omega t) \\ I_b \cos(\omega t - \frac{2\pi}{3}) \\ I_c \cos(\omega t + \frac{2\pi}{3}) \end{bmatrix} \tag{5.7}$$

$$i_d = \frac{1}{3}(I_a + I_b + I_c) + \frac{1}{3}\Big[I_a \cos(2\omega t) + I_b \cos(2\omega t + \frac{2\pi}{3}) + I_c \cos(2\omega t - \frac{2\pi}{3})\Big] \tag{5.8}$$

$$i_q = -\frac{1}{3}\Big[I_a \sin(2\omega t) + I_b \sin(2\omega t + \frac{2\pi}{3}) + I_c \sin(2\omega t - \frac{2\pi}{3})\Big] \tag{5.9}$$

For a converter operating in balanced conditions, the i_d and i_q compensators may also be implemented as PI controllers. In unbalanced conditions however, the rotating reference frame quantities no longer consist of strictly DC components which are suitable for tracking with a PI controller. This can be shown by applying the rotating reference frame (dq0) transformation to a three-phase quantity with magnitudes I_a, I_b, I_c as in (5.7). If the system is balanced such that $I_a = I_b = I_c = I$, the i_d and i_q quantities evaluate to $i_d = I$ and $i_q = 0$. However in the unbalanced case where $I_a \neq I_b \neq I_c$, applying the dq0 transform now results in i_d and i_q evaluating to (5.8) and (5.9) respectively.

From inspection of (5.8) and (5.9), both quantities now contain an AC component at twice the line frequency. It is well known from power system analysis that an unbalanced set of n phasors can be represented as 3 sets of n balanced phasors, namely the positive, negative and zero sequence components [181]. The AC components of the rotating reference frame quantities (which is rotating with angle $+\omega t$) are simply the negative sequence components of the original system, which would be represented as DC quantities in a rotating reference frame rotating at angle $-\omega t$, hence appearing with frequency 2ω in the $+\omega t$ frame.

To achieve power factor correction and draw balanced currents from the grid, despite an unbalanced input impedance, it is necessary to control both the positive and negative sequence components of the input current. Numerous control techniques have been proposed for operation in unbalanced conditions [182–190]. In general, extraction of the positive and negative sequence components of the measured currents must be performed so they may be regulated. A simple technique for achieving this is proposed in [191] based on the moving average filter (MAF). The MAF is defined as:

$$\bar{x}(t) = \frac{1}{T_w} \int_{t-T_w}^{t} x(\tau) d\tau \tag{5.10}$$

where T_w is the averaging window. Setting $T_w = \frac{1}{2f_{line}}$ will result in filtering of the second harmonic AC component of the i_d and i_q quantities, allowing the PI controller to track a DC value, representing the positive sequence current.

To cancel the negative sequence current, an approach is proposed based on a direct proportional gain compensator in the positive sequence rotating reference frame. The negative sequence component is extracted by subtracting the MAF output from the MAF input. A gain is applied to the negative sequence component which is then subtracted from the voltage command output of the PI controller, effectively inducing a negative sequence voltage at the rectifier terminals that is 180° out of phase with the negative sequence current. In steady state, this will drive the negative sequence components to zero while allowing the PI controller to regulate the positive sequence components as it would in a balanced system. The structure for the i_d compensator is shown in Fig. 5.8. The i_q compensator is identical, though the PI gains may be adjusted to provide more robust tracking of the constant $i_q = 0$ setpoint.

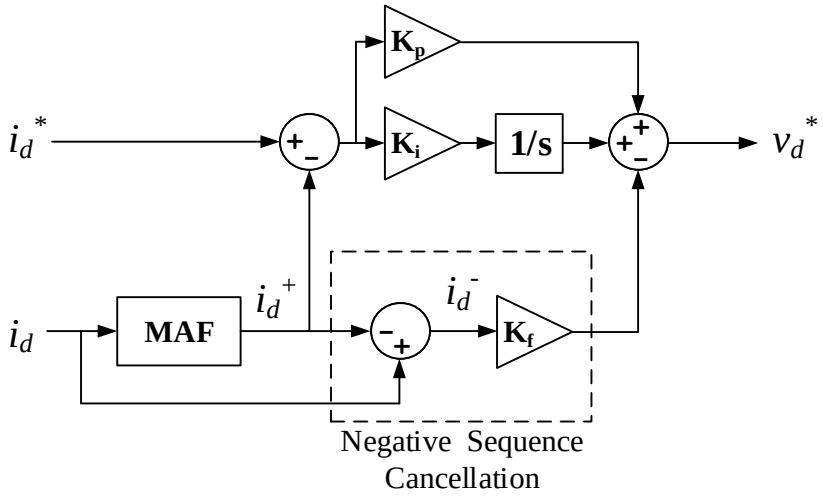

Figure 5.8: Current compensator structure for i_d and i_q control with negative sequence cancellation.

While it is simple to implement and offers good steady state performance, this method has some disadvantages as the MAF introduces a delay of T_w which negatively impacts the transient response of the controller. Additionally the negative sequence compensation proportional gain K_f must be chosen carefully to ensure controller stability yet cause the negative sequence current to be sufficiently suppressed. In the case of a battery charging application, the transient response time is not critical as the battery pack voltage changes significantly more slowly than the controller response, hence this method will be employed in demonstrating the A+HB converter charging capability.

The fourth phase of the converter is used as a non-inverting buck-boost DC/DC converter, shown in Fig. 5.9. By holding Q_H on and modulating Q_L, boost operation is achieved according to $V_o = \frac{1}{1-d}V_i$ where d is the modulation duty cycle. Similarly, holding Q_L off and modulating Q_H results in buck operation in which $V_o = dV_i$. Closed loop output voltage control can be achieved with a PI regulator which controls the

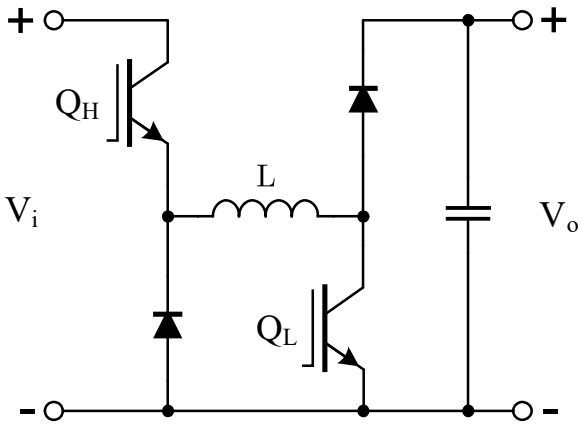

Figure 5.9: Non-inverting buck-boost DC/DC converter topology.

modulation duty cycle based on the measured output voltage. For battery charging applications in which a constant-current constant-voltage (CCCV) profile is used, this voltage loop can be altered to instead control the output current during the constant current portion of the charge.

5.5 Results

5.5.1 Motoring Mode

Simulation results are presented in Figures 5.10 and 5.11 of a 300 Nm load which is applied at 0.01s being accelerated to a speed of 1200 rpm. The mean torque is measured to be 350 Nm. The hysteresis controller reference current is 350A and the DC link voltage is 800V.

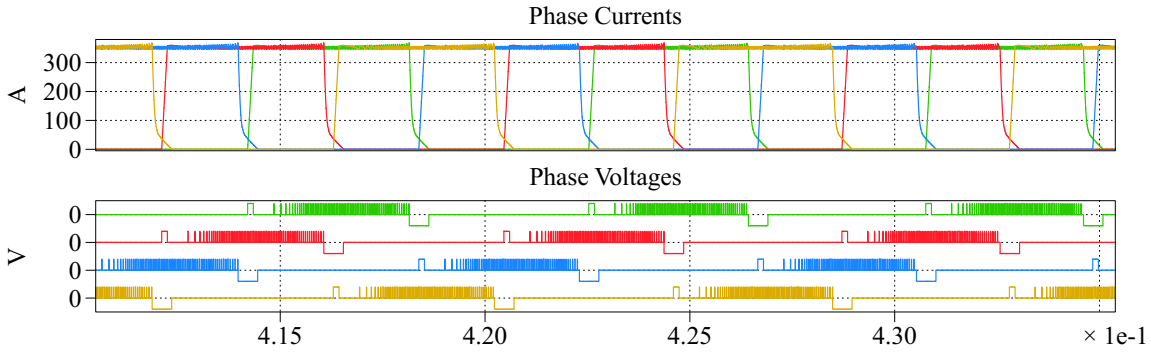

Figure 5.10: Phase voltages and currents operating in the motoring mode with soft switching ($\theta_{on} = -15°, \theta_{off} = 155°$, $I_{ref} = 350$,A, $V_{dc} = 800$V).

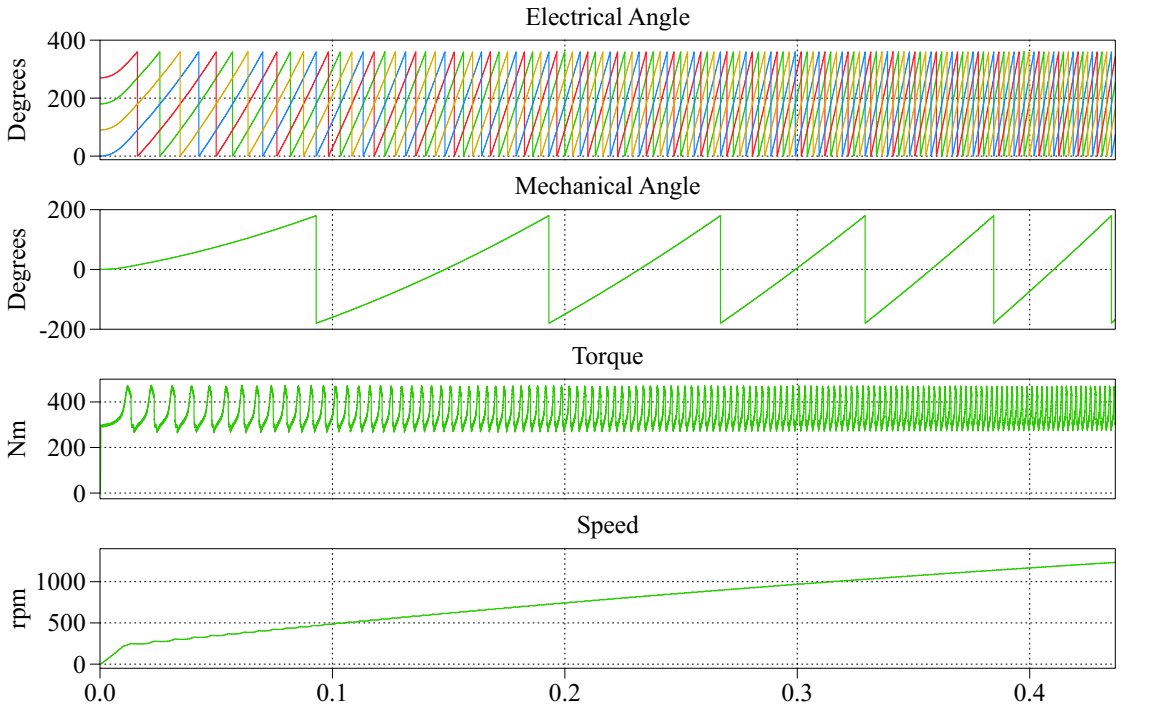

Figure 5.11: SRM model accelerating 300 Nm load.

5.5.2 Charging Mode

The machine and converter models and control are implemented in MATLAB/Simulink with PLECS. To demonstrate the converter charging mode in vehicle applications, the converter is tested at two operating points. First, an 800 V battery and a 208 V (line-to-line rms) three-phase grid are applied to demonstrate the boost capabilities. Second, a 400 V battery and a 480 V (line-to-line rms) three-phase grid are applied to demonstrate buck operation. The battery is modelled as a fixed voltage source with a series resistance. The simulation parameters are shown in Table 5.2.

During the charging mode, the rotor is fixed in place with the vehicle parking pawl or a separate brake on the motor shaft to prevent rotation. Evidently the parked rotor position will have an effect on the converter performance as the phase inductances will vary. For the simulations, the initial angle was selected as 37.5 mechanical degrees or 225 electrical degrees, as given in Fig. 5.5. This is corresponding to phase A and phase D being in the minimum inductance position and phase B and C having equal inductances that are 2/3 of the maximum inductance. This position indicates that the DC/DC converter and one phase of the boost rectifier can operate with the minimum phase inductance, while the remaining phases can operate with 2/3 of the maximum inductance. Converter operation was also validated where the DC/DC converter phase operates at minimum phase inductance. As the transient response requirements of the DC/DC converter are not significant, the controller can be conservatively tuned for stability across the range of plant transfer functions.

A practical implementation should consider the capacitor voltages when actuating the switches to reconfigure the converter. After charging, C1 and C2 will be at different

voltages, with C2 either being at a higher or lower voltage than C1, depending on the boost or buck mode of operation respectively during charging. When transitioning out of the buck mode, C1 can be easily discharged to the same potential as C2 by briefly operating Q10 and Q11 as a buck converter after disconnection of the grid input. To transition out of the boost mode, C1 should first be discharged to zero volts with the same mechanism as the buck mode, then the battery pack contactors opened, and C2 discharged with the typical bleed resistor discharge circuitry implemented in traction inverters. With C1 and C2 now both at zero volts, S2 can be closed and the standard precharge mechanism used to bring C1 and C2 to the battery pack voltage before closing the battery pack contactors. With these strategies, no additional hardware is required to balance the capacitor voltages before reconfiguring between the charging and motoring modes.

Boost mode charging at 16 kW is illustrated in Fig. 5.12. Buck mode charging at 32 kW is illustrated in Fig. 5.13. The simulation results are summarized in Table 5.3. In both cases, the power factor was calculated to be above 0.99.

Table 5.2: Charging mode simulation parameters.

Parameter	Value
Switching frequency	12.6 kHz
Grid frequency	60 Hz
C1	250 µF
C2	250 µF
Boost Mode (16 kW)	
Grid voltage	208 V (line-to-line rms)
Battery voltage	800 V
Battery resistance	200 mΩ
Battery current setpoint	20 A
Buck Mode (32 kW)	
Grid voltage	480 V (line-to-line rms)
Battery voltage	400 V
Battery resistance	100 mΩ
Battery current setpoint	80 A

Table 5.3: Charging mode simulation results.

Quantity	Value
Boost Mode (16 kW)	
Line current rms	45 A
Line current THD	1.1%
Battery voltage ripple	0.37%
Peak rotor torque	29.3 Nm
Buck Mode (32 kW)	
Line current rms	39 A
Line current THD	1.4%
Battery voltage ripple	0.24%
Peak rotor torque	32.7 Nm

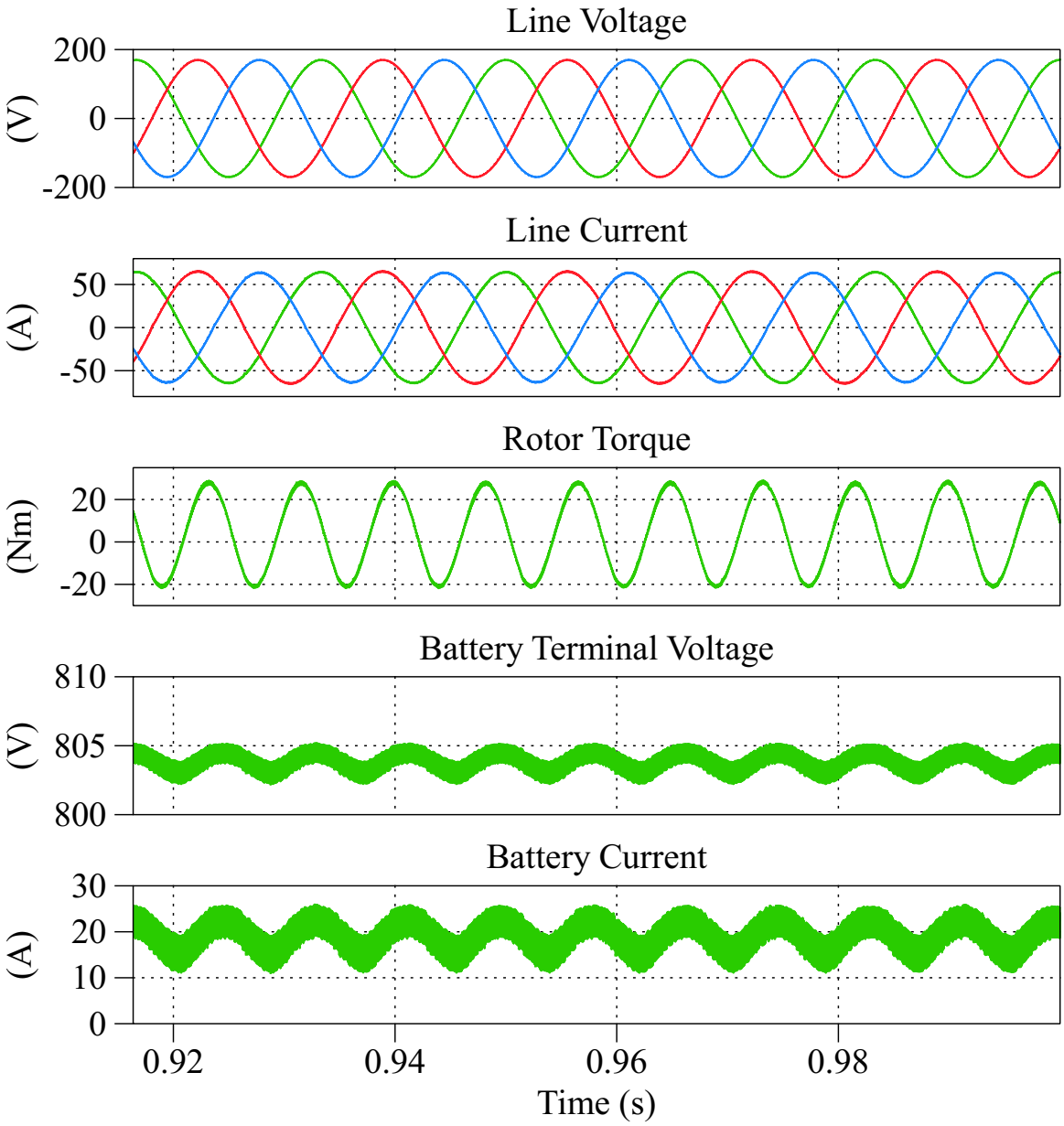

Figure 5.12: Charging with 208 V grid and 800 V battery.

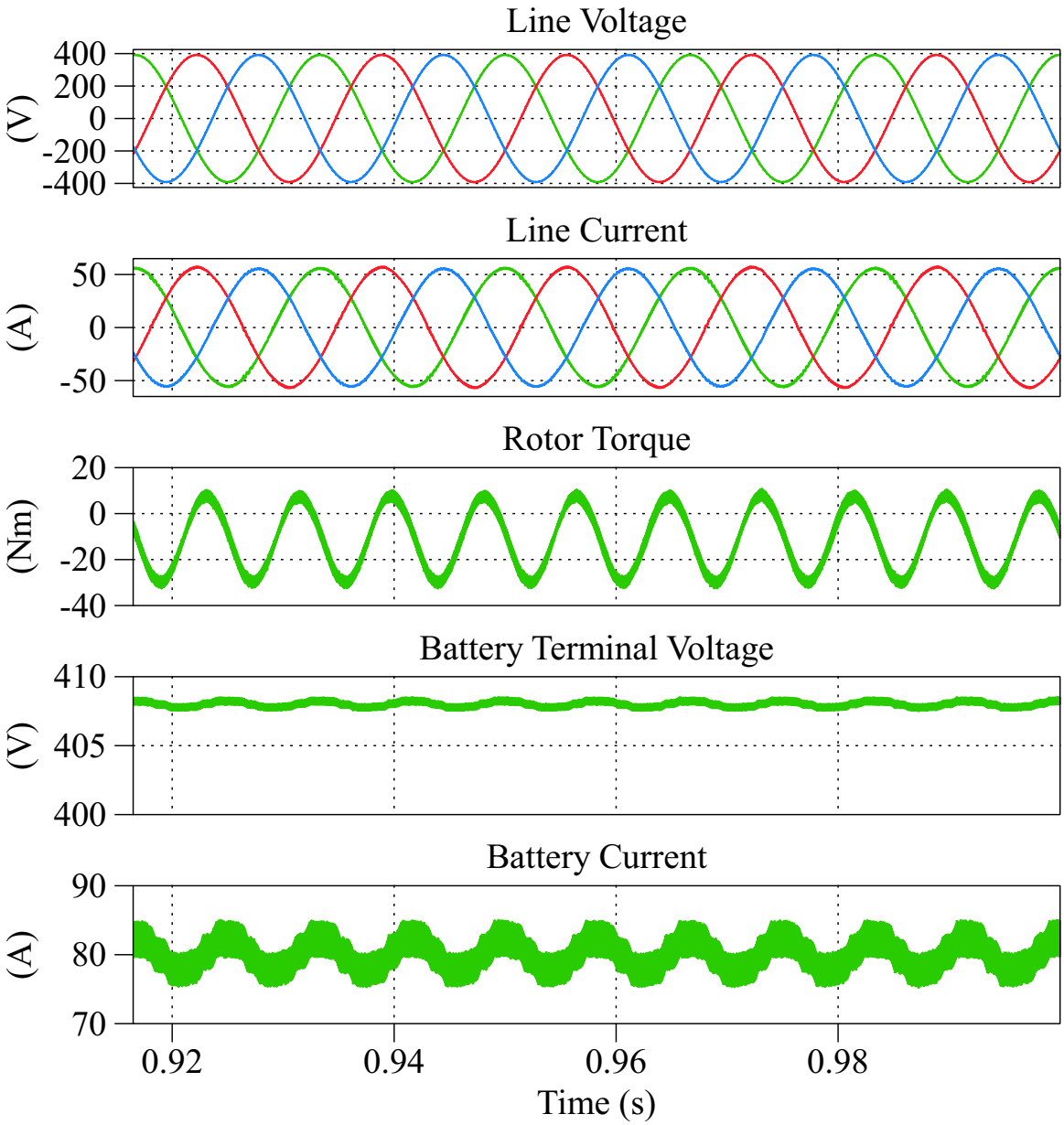

Figure 5.13: Charging with 480 V grid and 400 V battery.

5.6 Conclusions

A new integrated charging topology for four-phase SRM based powertrains has been presented. Compared to a standard four-phase asymmetric bridge converter, the proposed A+HB converter requires three additional IGBT switches, three additional diodes and two relays. In the motoring mode, the topology operates as a conventional asymmetric bridge converter. In the charging mode, three phases are used to form a boost rectifier while the last phase forms a non-inverting buck-boost converter. A control scheme is developed to achieve power factor correction of the input grid current under the inherently unbalanced input impedance conditions presented by the topology. Moving average filters are used to extract the positive and negative sequence components of the input current which can then be regulated independently.

Buck and boost mode operation of the DC/DC converter stage is demonstrated at 32 and 16 kW respectively. Output voltage ripple was found to be below 1%, making the topology suitable for constant voltage charging. This represents a significant improvement in power over typical existing dedicated OBC systems with a minimal number of additional required components.

Though the presented topology is for three phase charging using a four phase asymmetric bridge converter, the concept can be generalized to other input and machine phase counts. The power capability of the proposed topology is limited by the final DC/DC converter phase which must transfer the entirety of the charging power. By increasing the machine phase count to five or more phases, the DC/DC converter power capability can be increased through interleaving with the additional phases. Reducing the phase count of the machine to three phases presents two potential configurations: boost only

three phase charging in which the battery voltage must always be higher than the peak grid voltage, or single phase operation with the third phase retaining the the DC/DC converter functionality. The four phase machine configuration presented may also be used for single phase charging, with a two phase interleaved DC/DC converter.

Chapter 6

Integrated Charger for Conventional Machines

6.1 Introduction

This chapter presents a new IBC topology which takes advantage of paralleled devices in the traction inverter. The topology can achieve both single-phase AC charging and DC/DC conversion for fast charging, eliminating the need for both the OBC and boost converter for DC fast charging compatibility. Additionally, the proposed IBC is capable of V2G operation, demonstrating the functionality benefits of integrated solutions. The proposed topology is developed and the modes of operation explained. Modelling of the converter operation and electric machine is presented. The decoupled machine model developed in Chapter 4 is applied to predict the torque production in the electric machine during charging and zero torque rotor positions are identified.

A control strategy is derived for the charging modes and experimental results for all operating modes presented.

As discussed in Chapter 3, EVs today are expected to be capable of charging their battery packs from a variety of power sources at ever increasing power levels. OBCs enable charging from a standard AC grid connection allowing drivers to recharge their vehicles at their homes overnight. Most EVs include OBCs with power capabilities ranging from 6.6 kW to 11.5 kW. For more rapid charging, DC fast chargers have begun to proliferate, connecting directly to the vehicle's battery pack with advertised charging rates in excess of 300 kW [128].

Conventional OBCs consist of several stages of converters which provide PFC rectification, galvanic isolation through a high frequency transformer, and regulation of the DC output. DC fast chargers move the power electronics off board, providing isolation, rectification, and DC/DC conversion at much higher power levels than would be possible on board. While the vast majority of plug-in electric vehicles today operate with a nominal battery voltage in the range of 400V and below, new vehicles are beginning to emerge with battery voltages up to 800V [10]. To allow fast charging an 800V battery pack from the deployed networks of 400V fast chargers, Porsche has included a 50 kW DC/DC boost converter in their recent 800V powertrain, optionally upgraded to 150 kW [192]. This boost converter is in addition to the onboard AC charger, adding further weight and cost to the vehicle.

Numerous IBC topologies have been proposed, for both single-phase and three-phase charging and across many powertrain configurations and electric machine types. For general automotive applicability, the IBC topology should at least be capable of charging the battery from single-phase AC mains in the case where the peak grid

voltage is above or below the battery pack voltage at any state of charge (SoC). As discussed in Chapter 3, many proposed topologies require non-standard electric machine connections which expose the machine neutral point [9, 139, 142], provide open ended windings or split windings [140, 146, 147], or make use of multiphase machines [152, 193, 194]. This can be a disadvantage as it presents an additional barrier to adoption by automotive manufacturers, requiring new machine designs and in some cases significant modifications to the inverter design and operation. Additionally, many solutions result in torque being produced by the machine during charging, requiring a mechanical brake to prevent the vehicle from moving. Other proposed solutions require no modifications to the machine, but add an additional frontend converter for AC rectification and PFC, resulting in a less integrated solution [143, 144]. The ideal charging solution will vary significantly based on the specific application requirements, presenting opportunities for further integrated charging concepts to be developed.

The traction inverter, which is a key component of many IBC topologies, is typically a three-phase, two level voltage source inverter, implemented with six IGBT or more recently, SiC MOSFET switches. In some implementations, paralleled discrete devices are used to achieve the required current ratings, and in the case where phase leg or six-pack power modules are used, several dies are often paralleled internally to implement one switch [10]. These paralleled devices can provide additional flexibility in implementing an IBC topology, as they may be separated into additional phase legs during charging operation, with careful application of additional semiconductor or electromechanical switches at the point of paralleling.

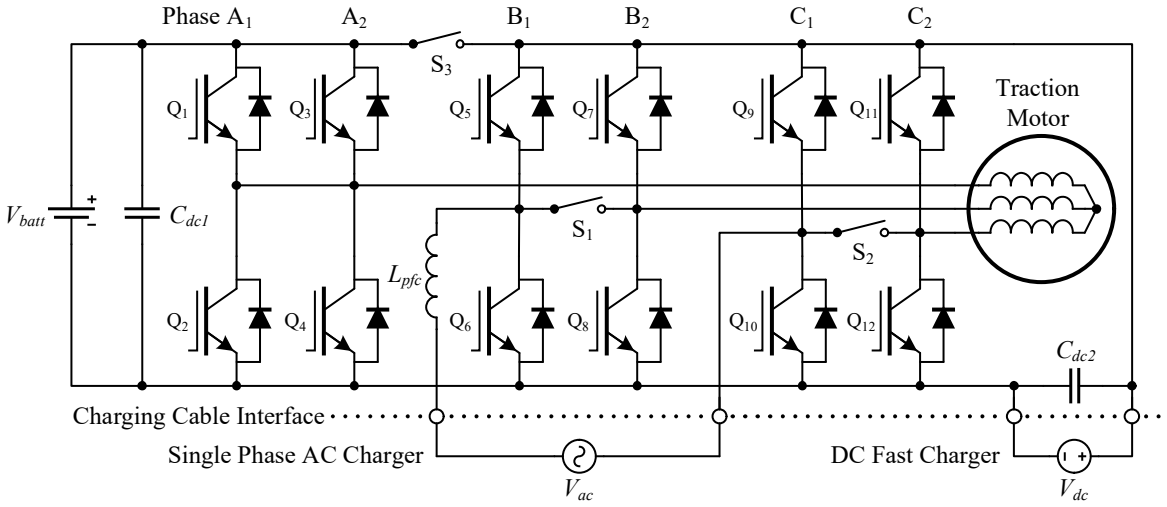

Figure 6.1: Proposed IBC topology with AC and DC charging connections.

6.2 Proposed Topology

The proposed IBC topology is developed from a three-phase VSI constructed with at least two devices in parallel per switch. In the VSI mode these devices operate in unison, sharing the phase current. In the charging mode, the devices are separated and can operate independently. The proposed topology is shown in Figure 6.1. The topology is considered to have universal input capabilities as it can charge the battery from any single phase AC or DC voltage source within the component voltage ratings, regardless of the relative source and battery voltages. Additionally, the converter is fully bidirectional, capable of vehicle-to-grid (V2G) operation. Switch S_1 and S_2 separate the individual phase legs in phases B and C, allowing phase legs B_1 and C_1 to act as a full bridge boost rectifier, with the addition of external PFC inductor L_{ac}. Switch S_1, when opened, splits the DC link of the converter, allowing DC/DC conversion of either the full bridge rectifier output or an external DC fast charger output, to the battery pack voltage, facilitating charging. The phases of the electric

machine are used to form the DC/DC converter inductance. If the DC/DC converter is operating in buck mode, phases A and B are used in series. In boost mode, phases B and C are paralleled, and series connected with phase A. In this implementation, an interior permanent magnet synchronous machine (IPMSM) is considered, though an induction machine can also be used. With all switches S_1, S_2, S_3 closed and charging sources disconnected, the converter forms a conventional three-phase VSI. Standard motor control and modulation techniques may be applied to drive the machine. Note that unlike a conventional VSI, the DC link capacitor must be split into two distinct capacitors C_{dc1} and C_{dc2}, though the total capacitance can remain the same. Ideally the capacitors are distributed across the DC bus, to mitigate the effects of any parasitic inductance introduced by S_3. An example of this configuration is shown in Section 6.5.

Considering the converter from the perspective of three-terminal cells as discussed in Chapter 4, there are six potential bidirectional SPDT implementations present. With the introduction of S_1 and S_2, five of them become accessible, as A_1 and A_2 remain paralleled effectively forming a single cell. The wye-connected machine however presents only one usable inductance. Therefore with the addition of S_3, the machine windings can act as a common inductance between two cascaded SPDT implementations, resulting in a bidirectional non-inverting buck-boost converter. To form any additional three-terminal cells now that the motor winding inductance has been used, an external inductor is required, hence the addition of L_{ac}. L_{ac} can be considered as a common inductor between B_1 and C_1, again cascading the bidirectional SPDT cells, forming a full bridge converter.

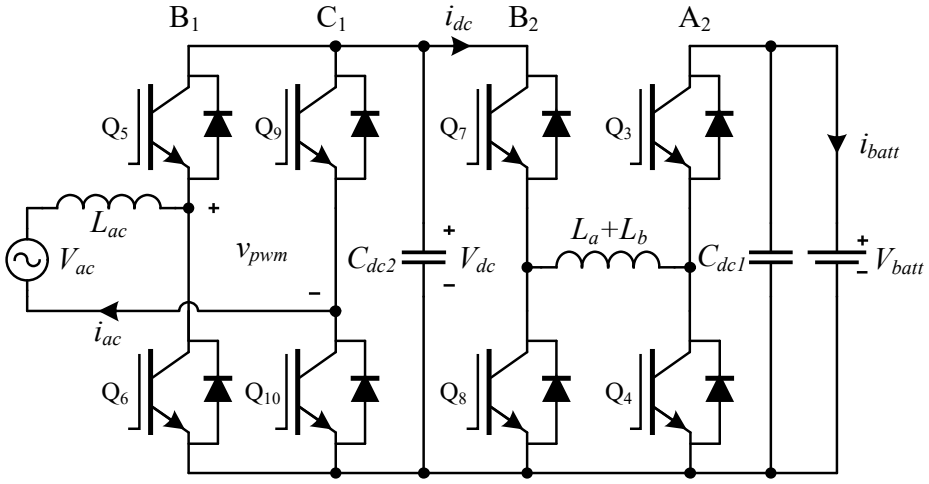

Figure 6.2: AC charging mode equivalent circuit.

6.2.1 AC Grid Charging

In the AC charging mode, switches S_1, S_2 and S_3 are opened. The equivalent circuit in the AC charging mode is shown in Fig. 6.2. V_{ac} is the rms voltage of the AC supply. Phase legs B_1 and C_1 form a single phase, full bridge boost rectifier while A_2 along with B_2 and C_2, form a buck, boost or buck-boost converter using the motor winding inductance. The two stage converter allows charging the battery regardless of the relative voltages of the grid and battery pack. In the case where the peak grid voltage is less than the battery pack voltage, S_3 can remain closed and the boost rectifier can directly charge the battery pack as a single stage. The full bridge boost rectifier controls are detailed in Section 6.4.1.

6.2.2 DC Fast Charging

If a DC source V_{dc} is available, all switches S_1, S_2, and S_3 are opened and a buck, boost or buck-boost converter can be formed. In the buck mode, to minimize the inductor

current ripple, it is preferable to maximize the inductance by using only phases A and B in series. This is achieved by modulating Q_7 and leaving the remaining devices turned off. The equivalent inductance is $L_a + L_b$, as phase C is left open circuit. The equivalent circuit for the buck mode is shown in Fig. 6.3a.

In the boost mode, phases B and C must be paralleled. This is due to the voltage at the motor winding midpoint now being higher than V_{dc}, which would result in current flowing back through phase C and the antiparallel diode of Q_{11}. Therefore to achieve boost operation, Q_7 and Q_{11} are held on, and Q_4 is modulated. The equivalent inductance is now $L_a + L_b \parallel L_c$. The equivalent circuit in the boost mode is shown in Fig. 6.3b.

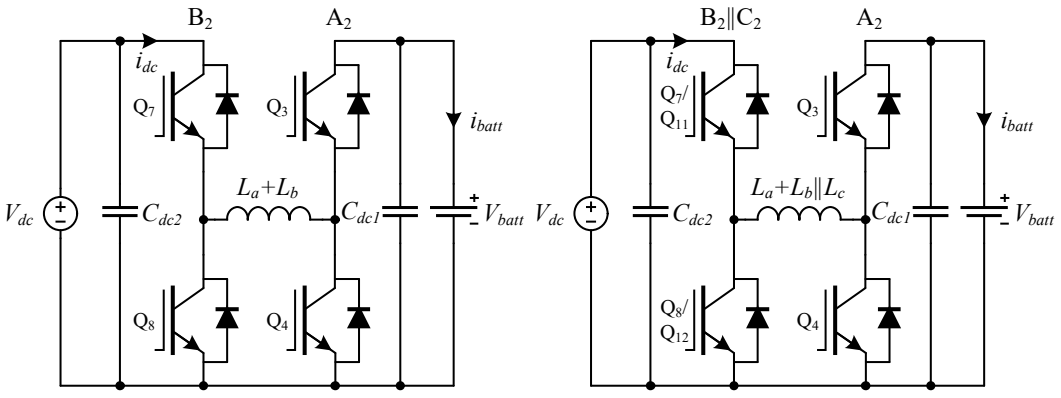

(a) DC charging buck mode ($V_{dc} > V_{batt}$) equivalent circuit.

(b) DC charging boost mode ($V_{dc} < V_{batt}$) equivalent circuit.

Figure 6.3: DC charging mode equivalent circuits.

6.3 Converter Modelling

To establish the performance of the proposed converter in the charging modes, several aspects of the system are modelled analytically. First, the maximum charging power

capability as a function of the inverter power rating is determined. Next, a simplified decoupled model of the phase inductances and torque production in the electric machine during charging is presented, based on the analysis in Chapter 4. Finally, this model is used to predict the rotor positions in which torque is not produced during charging, and calculate the inductance provided by the machine phases for DC/DC converter operation.

6.3.1 Charging Power Limits

In the AC charging mode, the power will typically be limited by the PFC inductor L_{ac} with series parasitic resistance R_{ac}. The inductor must be sized to support the AC input current for maximum power rating P_{ac} of the charger for all supported grid voltages V_{ac}.

$$I_{L_{ac},rms} = \frac{P_{ac}}{V_{ac}} \tag{6.1}$$

In the DC charging mode, the power will be limited by the current rating of the inverter switches and the motor phase windings. The inverter kVA S can be expressed as

$$S = \sqrt{3} V_{ll} I_{ph} \tag{6.2}$$

where $V_{ll} = \frac{V_{batt}}{\sqrt{2}}$, assuming maximum modulation index and SVPWM. Thus the maximum rms phase current I_{ph} as a function of rated kVA and battery voltage V_{batt} is

$$I_{ph} = \sqrt{\frac{2}{3}} \frac{S}{V_{batt}} \tag{6.3}$$

In the boost mode of operation, the average inductor current in phase A is equal to

the input current I_{dc} which can be written in terms of the DC charging power P_{dc} and the DC charging input voltage V_{dc}

$$I_{L_a,avg} = I_{dc} = \frac{P_{dc}}{V_{dc}} \tag{6.4}$$

The input voltage can be written in terms of the battery voltage and the boost ratio η, where $\eta = V_{batt}/V_{dc}$. Therefore the average inductor current can be written as

$$I_{L_a,avg} = \sqrt{\frac{2}{3}}\frac{P_{dc}\eta}{V_{batt}} \tag{6.5}$$

Equating the average inductor current in the charging mode, and the maximum rms phase current in the driving mode, the maximum charging power as a function of rated inverter kVA can be found as

$$P_{dc} = \sqrt{\frac{2}{3}}\frac{S}{\eta} \tag{6.6}$$

This assumes parallel operation of both legs of phases A such that the total switch current capability is the same as in the driving mode. For example, when charging an 800V battery from a 400V fast charger, the worst case boost ratio is 2, therefore $P_{dc} = S/\sqrt{6}$.

6.3.2 Torque Production

To analyze the torque production in the machine during the charging mode, the standard three-phase synchronous machine model in the stationary reference frame

can be used. This is derived in detail in Chapter 4, with the key results repeated here. The phase voltage equation in the stationary frame can be written as:

$$\mathbf{v}_{abc} = r_s \mathbf{i}_{abc} + \frac{d}{dt}\boldsymbol{\lambda}_{abc} \tag{6.7}$$

where r_s is the winding resistance, which will be assumed to be negligible, and $\mathbf{i}_{abc}$ and $\mathbf{v}_{abc}$ are the stator current and voltage vectors respectively. Assuming a sinusoidal flux distribution, the flux linkage vector $\boldsymbol{\lambda}_{abc}$ can be represented as the product of the self and mutual stator winding inductances and the phase currents, plus the rotor permanent magnet flux

$$\boldsymbol{\lambda}_{abc} = \mathbf{L}_s \mathbf{i}_{abc} + \boldsymbol{\psi_f} \tag{6.8}$$

where $\mathbf{L}_s$ is defined as (6.9) and $\boldsymbol{\psi_f}$ is the permanent magnet flux [168]. L_A is the average value of the inductance and L_B is the amplitude of the sinusoidally varying component, and θ is the electrical angle of the rotor. L_A and L_B can also be defined in terms of the L_d and L_q quantities from the rotating reference frame as $L_A = \frac{L_d+L_q}{3}$ and $L_B = \frac{L_q-L_d}{3}$.

$$\mathbf{L}_s = \begin{bmatrix} L_A + L_B\cos 2\theta & -\frac{1}{2}L_A + L_B\cos 2(\theta - \frac{\pi}{3}) & -\frac{1}{2}L_A + L_B\cos 2(\theta + \frac{\pi}{3}) \\ -\frac{1}{2}L_A + L_B\cos 2(\theta - \frac{\pi}{3}) & L_A + L_B\cos 2(\theta - \frac{2\pi}{3}) & -\frac{1}{2}L_A + L_B\cos 2(\theta + \pi) \\ -\frac{1}{2}L_A + L_B\cos 2(\theta + \frac{\pi}{3}) & -\frac{1}{2}L_A + L_B\cos 2(\theta + \pi) & L_A + L_B\cos 2(\theta + \frac{2\pi}{3}) \end{bmatrix} \tag{6.9}$$

$$\mathbf{L}'_s = \begin{bmatrix} \frac{L_d+L_q}{2} + (L_d - L_q)\cos 2\theta & 0 & 0 \\ 0 & \frac{L_d+L_q}{2} + (L_d - L_q)\cos 2(\theta - \frac{2\pi}{3}) & 0 \\ 0 & 0 & \frac{L_d+L_q}{2} + (L_d - L_q)\cos 2(\theta + \frac{2\pi}{3}) \end{bmatrix} \tag{6.10}$$

In the case of a wye-connected machine with internal neutral point, in which no zero sequence current can flow (the sum of the phase currents is always zero) the $\mathbf{L}_s$ matrix can be simplified to the diagonal matrix $\mathbf{L}'_s$ in (6.10). This decoupled form is mathematically equivalent, subject to the stated constraint on the phase currents, and simplifies the analysis in the stationary frame. Note that the winding leakage inductance has been neglected so far. With the simplified matrix representation of the phase inductances, the leakage inductance can simply be added to the values of L_d and L_q to achieve accurate representation of the total phase inductance while having no impact on the resulting torque.

The torque expression can now be determined via co-energy considerations from the stationary frame model. For any electromagnetic system, the stored energy W can be calculated by integrating the current required to produce a given flux linkage

$$W = \int_0^{\lambda_1} i(\lambda) d\lambda \tag{6.11}$$

Equivalently (assuming no magnetic saturation in the machine), the co-energy W' can be calculated by integrating the flux linkage with respect to current

$$W' = \int_0^{i_1} \lambda(i) di \tag{6.12}$$

From the flux linkage expression (6.8), defining the PM flux as

$$\boldsymbol{\psi_f}(\theta) = \psi_0 \begin{bmatrix} \cos(\theta) \\ \cos(\theta - \frac{2\pi}{3}) \\ \cos(\theta + \frac{2\pi}{3}) \end{bmatrix} \tag{6.13}$$

the co-energy can be evaluated as

$$\begin{aligned}\mathbf{W}' &= \int_0^i \mathbf{i}_{abc}\mathbf{L}_s(\theta)di + \int_0^i \boldsymbol{\psi_f}(\theta)di \\ &= \frac{1}{2}\mathbf{i}_{abc}^T\mathbf{L}_s(\theta)\mathbf{i}_{abc} + \mathbf{i}_{abc}^T\boldsymbol{\psi_f}(\theta)\end{aligned} \tag{6.14}$$

If the decoupled inductance matrix (4.47) is used, the torque contribution from each phase can be determined individually by noting the following power relationship and solving for the torque τ:

$$P = \tau\omega = \frac{dW'}{dt} \tag{6.15}$$

$$\frac{dW'}{dt} = \frac{1}{2}i^2\frac{dL}{d\theta}\omega + i\frac{d\psi_f}{d\theta}\omega \tag{6.16}$$

$$\tau = \frac{1}{2}i^2\frac{dL}{d\theta} + i\frac{d\psi_f}{d\theta} \tag{6.17}$$

Solving for each phase's torque contribution:

$$\begin{aligned}\tau_a &= i_a^2(L_q - L_d)\sin 2\theta - i_a\psi_0\sin\theta \\ \tau_b &= i_b^2(L_q - L_d)\sin 2(\theta - \frac{2\pi}{3}) - i_b\psi_0\sin(\theta - \frac{2\pi}{3}) \\ \tau_c &= i_c^2(L_q - L_d)\sin 2(\theta + \frac{2\pi}{3}) - i_c\psi_0\sin(\theta + \frac{2\pi}{3})\end{aligned} \tag{6.18}$$

In the proposed connection of the motor windings in the buck mode, $i_b = -i_a$ and $i_c = 0$. Therefore the total torque τ is

$$\tau = i_a^2(Lq - Ld)\sin(2\theta + \frac{\pi}{3}) - \sqrt{3}i_a\psi_0\sin(\theta + \frac{\pi}{6}) \tag{6.19}$$

which is zero for $\theta = n\pi - \frac{\pi}{6}, n \in \mathbb{Z}$, regardless of i_a.

In the boost mode, the average currents are split evenly between the two paralleled windings such that

$$i_b = i_c = -\frac{i_a}{2} \tag{6.20}$$

The average torque is

$$\tau_e = \frac{3}{4} i_a^2 (L_q - L_d) \sin(2\theta) - \frac{3}{2} i_a \psi_0 \sin\theta \tag{6.21}$$

which is zero for $\theta = n\pi, n \in \mathbb{Z}$.

To reach a zero torque position, the rotor would have to rotate a maximum of $\frac{\pi}{2}$ or 90 electrical degrees. This can be converted to a mechanical angle θ_m given the number of pole pairs P as $\theta_m = \frac{\theta}{P}$. If the total drive ratio N_t and the tire radius r_{wheel} of the vehicle is known, the rotor shaft rotational displacement can be converted to a linear displacement d of the vehicle

$$d = \frac{\theta_m}{N_t} r_{wheel} \tag{6.22}$$

As an example, the Chevy Bolt EV has a 4 pole-pair IPMSM, total drive ratio of 7.05 and standard tire diameter of 25.5 inches. In the worst case, the vehicle would need to move forwards or backwards 1.8cm to reach a zero torque rotor position suitable for charging. This is similar in magnitude to the already existing backlash in the geartrain and parking pawl and therefore does not place any significant requirements on the vehicle or driver to achieve zero torque integrated charging.

6.3.3 DC/DC Converter Inductance

The equivalent inductance from the phase windings available for use by the DC/DC converter can be easily calculated from the decoupled inductance matrix. In the buck mode:

$$L_a + L_b = L_d + L_q + (L_d - L_q)\cos\left(2\theta - \frac{\pi}{3}\right) \tag{6.23}$$

which at any zero torque position for the series winding configuration is

$$L_a + L_b = 0.5L_d + 1.5L_q \tag{6.24}$$

In the boost mode:

$$L_a + L_b \parallel L_c = \frac{3L_dL_q}{L_d + L_q + (L_q - L_d)\cos 2\theta} \tag{6.25}$$

which at any zero torque position for the parallel winding configuration is

$$L_a + L_b \parallel L_c = 1.5L_d \tag{6.26}$$

6.4 Control Strategy

The high level control strategy is shown in Fig. 6.4 and consists of three primary controllers. A conventional field oriented control scheme is used in the driving mode. In the charging mode, the PFC and DC/DC controllers are activated. The active controller(s) are determined by the mode selector block, which also enables the relays as required to achieve each mode.

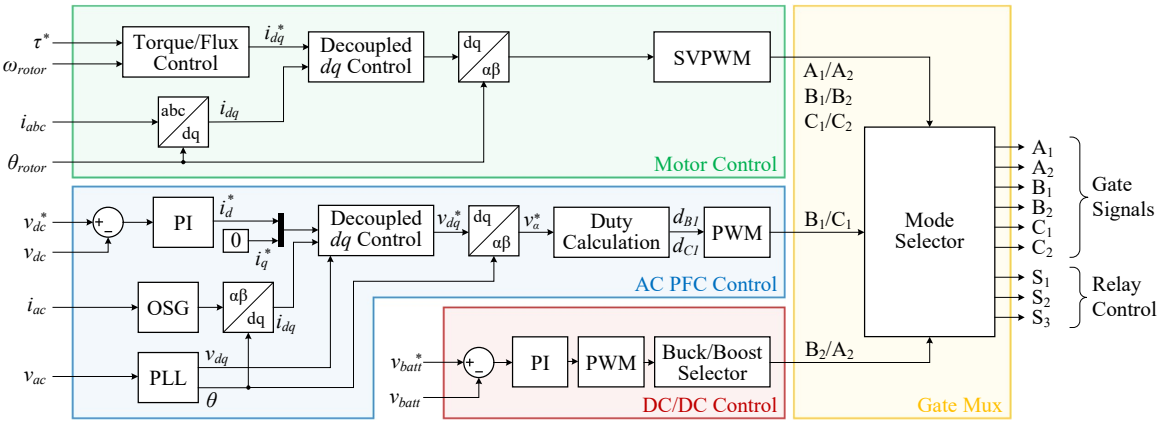

Figure 6.4: IBC control block diagram.

6.4.1 AC PFC Control

In the AC charging mode, power factor corrected operation of the full bridge converter is implemented with single-phase *dq* control using fictitious axis emulation (FAE) [195]. This control structure allows independent bidirectional control of active and reactive power, allowing a single controller for both charging and V2G operation. The primary components of the controller are the phase locked loop (PLL), the *dq* frame current controller, and the outer voltage or current loop. A brief overview is provided of the relevant transfer functions for each component and their gain selection procedures.

PLL

In three-phase systems, the measured phase voltages can be directly transformed into the two variable $\alpha\beta$ frame and subsequently into the rotating *dq* frame. A standard *dq* transform based PLL can then be implemented to estimate the grid phase angle. For single-phase systems, the β voltage must first be synthesized from the measured α voltage through an orthogonal signal generator (OSG). A second order generalized

integrator (SOGI) is used to both filter the measured single-phase grid voltage and generate an orthogonal β voltage component. The SOGI structure is shown in Fig. 6.5.

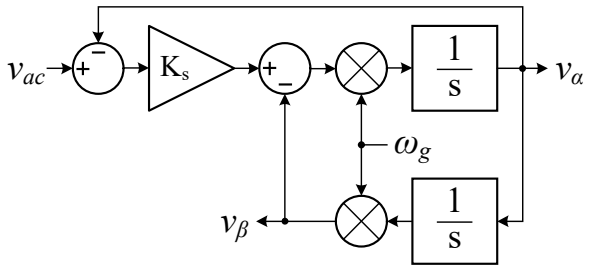

Figure 6.5: Second order generalized integrator structure.

The transfer function for the α and β outputs of the SOGI are given by

$$\begin{bmatrix} v_\alpha \\ v_\beta \end{bmatrix} = \begin{bmatrix} \dfrac{K_s\omega_g s}{s^2 + K_s\omega_g s + \omega_g^2} \\ \dfrac{K_s\omega_g^2}{s^2 + K_s\omega_g s + \omega_g^2} \end{bmatrix} v_{ac} \tag{6.27}$$

where ω_g is the estimated grid frequency and K_s is the SOGI gain. Given the second order transfer function, K_s can be selected as $\sqrt{2}$ to achieve optimal damping.

With the fictitious β voltage v_β now established by the SOGI, a standard dq PLL can now be implemented as shown in Fig. 6.6 where ω_0 is the initial grid frequency

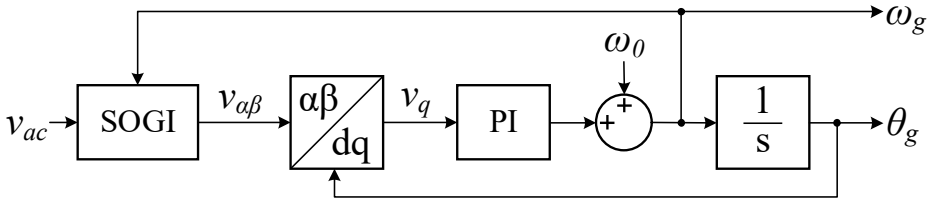

Figure 6.6: Phase locked loop structure.

estimate, and θ_g is grid phase angle estimated by the PLL. The SOGI PLL transfer

function is given by

$$G_{pll}(s) = \frac{K_{sp}s + K_{si}}{s^2 + K_{sp}s + K_{si}} \tag{6.28}$$

where K_{sp} and K_{si} are the PLL proportional and integral gains respectively. To achieve a desired settling time and optimal damping, K_{sp} and K_{si} can determined from the damping ratio ζ and natural frequency ω_{pll} of (6.28) [196].

$$\zeta = \frac{K_{sp}}{2\sqrt{K_{si}}} \qquad \omega_{pll} = \sqrt{K_{si}} \tag{6.29}$$

With the damping ratio set to $1/\sqrt{2}$ and the 1% settling time t_s given by

$$t_s = \frac{-\ln(0.01)}{\zeta\omega_{pll}} \tag{6.30}$$

The PI gains are determined as

$$K_{sp} = \frac{9.2}{t_s} \qquad K_{si} = \frac{42.3}{t_s^2} \tag{6.31}$$

DQ Current Controller

Similar to the voltage, an orthogonal β current signal must be generated in order for the input current to be transformed into the dq frame for regulation by conventional PI controllers. A delay based OSG is employed for the current since the transient response requirements for a battery charging application do not necessitate more complex techniques which can be sensitive to component parameter variations. The measured line current is delayed by one quarter of a line cycle ($T/4$) to produce a the β current signal, as shown in Fig. 6.7.

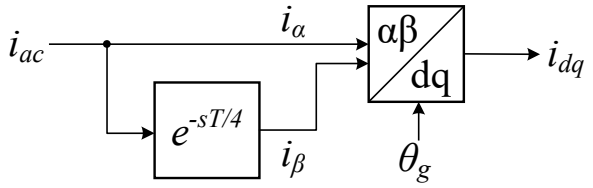

Figure 6.7: Delay based orthogonal signal generator for input current.

The d and q axis currents can now be regulated independently with a typical decoupled dq current regulator as shown in Fig. 6.8. The d axis current represents real power, while the q axis represents reactive power. The sign of the d and q axis currents determines the direction of power flow allowing charging or V2G operation.

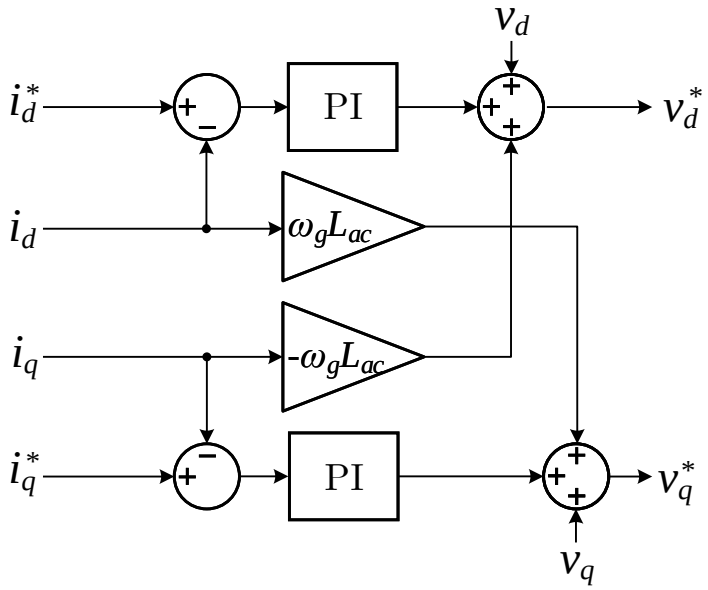

Figure 6.8: Decoupled dq current controller.

PI gains for the dq current controller can be determined based on the current plant transfer function $G_p^i(s)$. As the d and q axis currents are decoupled by the controller, their transfer functions are identical and the same PI gains can be used for both axis.

$$G_p^i(s) = \frac{i_d(s)}{v_d(s)} = \frac{i_q(s)}{v_q(s)} = \frac{1}{sL_{ac} + R_{ac}} \tag{6.32}$$

The PI controller transfer function is

$$G_{PI}(s) = K_p + \frac{K_i}{s} \tag{6.33}$$

resulting in an open loop transfer function of

$$G^i_{ol}(s) = \frac{K_p}{L_{ac}}\left(\frac{s + K_i/K_p}{s + R_{ac}/L_{ac}}\right) \tag{6.34}$$

The plant pole can be canceled by selecting K_p and K_i as

$$K_p = \frac{L_{ac}}{\tau_i} \qquad K_i = \frac{R_{ac}}{\tau_i} \tag{6.35}$$

reducing the closed loop transfer function to

$$G^i_{cl}(s) = \frac{i_d(s)}{i^*_d(s)} = \frac{i_q(s)}{i^*_q(s)} = \frac{1}{\tau_i s + 1} \tag{6.36}$$

where τ_i is the time constant of the system and can be determined by standard bandwidth and phase margin considerations [196]. The bandwidth should be high enough to minimize distortions in the input current but low enough to substantially reject switching current ripple.

Outer Voltage/Current Loop

When the boost rectifier is charging the battery directly, the output current should be controlled during the constant current (CC) phase of charging. During the constant voltage (CV) phase of charging, or in the case when the cascaded DC/DC converter is

employed, the output voltage should be regulated. In either case, due to the nature of single-phase rectifiers, a large ripple component at twice the line frequency will exist and the controller bandwidth should be limited to avoid attempted regulation of the ripple. A safe choice is to limit the controller bandwidth to one tenth the ripple frequency. For a 60Hz grid, the ripple appears at 120Hz and the controller bandwidth should therefore be no more than 12Hz.

Assuming the load can be modelled by an equivalent resistance R_L, the ouput voltage plant transfer function $G_p^v(s)$ can be approximated by power balance considerations [196] as

$$G_p^v(s) = \frac{v_{dc}(s)}{i_d(s)} = \frac{1}{\sqrt{2}} \frac{V_{ac}}{V_{dc}} \frac{R_L}{sC_{dc}R_L + 1} \tag{6.37}$$

where C_{dc} is either C_{dc2} or $C_{dc1} + C_{dc2}$, depending on the state of S_3. The open loop voltage transfer function is therefore

$$G_{ol}^v(s) = G_{PI}^v(s) G_{cl}^i(s) G_p^v(s) \tag{6.38}$$

where $G_{PI}^v(s)$ can be determined to suitably limit the closed loop bandwidth. An identical procedure can be performed for the output current regulator for the CC portion of charging, since $i_{dc}(s) = v_{dc}(s)/R_L$. Finally the full bridge phase leg duty cycles are calculated from the α component of the voltage command, as shown in Fig. 6.9.

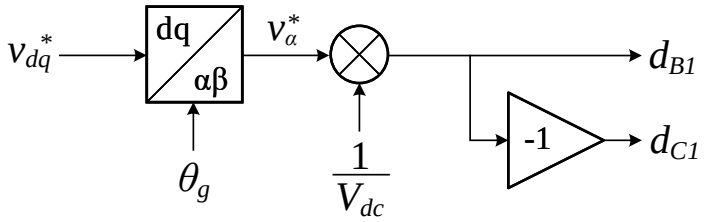

Figure 6.9: Full bridge duty cycle calculation.

6.4.2 DC/DC Control

In the DC fast charging mode, or in the case where the cascaded DC/DC converter is being used with an AC input, a suitable controller for the DC/DC converter structure in Fig. 6.3 must be developed. The four switch topology can operate as either a buck, boost or non-inverting buck-boost converter. Though the buck-boost mode may be necessary should the difference in the input and output voltages be small, the primary focus will be on the buck and boost modes. The buck mode would typically be applied when charging a battery pack with a voltage below the peak AC line input voltage. The boost mode can be used to charge a battery pack with a higher voltage than conventional DC fast chargers can supply (e.g 400 to 800Vdc conversion), or in the case where the conversion ratio for the single stage AC/DC converter would be prohibitively high (e.g 120Vac to 800Vdc).

The control-to-output transfer functions for the buck and boost converter are well known [167] and can be written in the standard second order form

$$G_{vd}(s) = G_{d0}\frac{1-\frac{s}{\omega_z}}{1+\frac{s}{Q\omega_0}+\left(\frac{s}{\omega_0}\right)^2} \tag{6.39}$$

The transfer function is generally stable open loop and can be compensated with conventional techniques. In the case of a battery charging application, adequate

Table 6.1: Experimental setup parameters.

Parameter	Value
Converter	
Switching frequency f_s	10 kHz
Grid frequency f_g	60 Hz
C_{dc1} / C_{dc2}	200 µF / 360 µF
L_{ac} / R_{ac}	4.8 mH / 0.2 Ω
Motor	
Pole pairs P	4
L_d / L_q	250 µH / 600 µH

performance can be achieved with a PI controller to eliminate steady state error.

6.5 Experimental Results

To validate the proposed topology, a prototype is constructed based on a six phase inverter. Phases A_1 and A_2 are permanently paralleled and relays S_1 and S_2 are installed to allow paralleling of phases B_1, B_2 and C_1, C_2 in the motoring mode, resulting in a conventional three-phase inverter. In the charging mode, the DC link can be split with relay S_3, and the phases separated to achieve the described AC and DC charging functionality. An IPMSM from a Chevy Bolt EV is connected to the converter to demonstrate charging operation with a production EV motor. The converter controls are implemented on a PLECS RT Box rapid control prototyping system with the sampling rate set to the switching frequency. The experimental setup is shown in Fig. 6.10 and setup parameters in Table 6.1.

Three distinct charging scenarios are tested to validate the operating modes of the

converter:

1. 120Vac charging of 400Vdc battery pack at 1.9 kW, single stage AC/DC conversion.

2. 240Vac charging of 200Vdc battery pack at 3.2 kW, cascaded DC/DC converter operated in buck mode, with 500V intermediate DC link.

3. 200Vdc charging of 400Vdc battery pack at 6 kW, single stage DC/DC conversion with converter operating in boost mode. Voltages have been scaled down from 400/800Vdc due to motor and power supply voltage limitations.

In each case, two channels of a bidirectional AC/DC power supply, shown in Figure 6.11, are used to source the input AC or DC power and sink the output DC power, emulating a battery pack load. The machine shaft is left unloaded. After a small rotation to reach a zero torque position, the rotor remains stationary during all charging scenarios.

6.5.1 120Vac to 400Vdc Charging

To achieve 120Vac to 400Vdc charging, only the boost PFC stage is required and no current flows in the motor windings. Relay S_3 remains closed and the entire DC bus capacitance is available ($C_{dc1} + C_{dc2}$). Despite this, as shown in Fig. 6.12, a significant 120Hz component exists in the DC output current. This is typical of single phase battery chargers and has been shown to have a negligible effect on battery cycle life and charging efficiency [197]. The input grid current shows good power factor. A harmonics analysis of the grid current up to the 40th harmonic is shown in

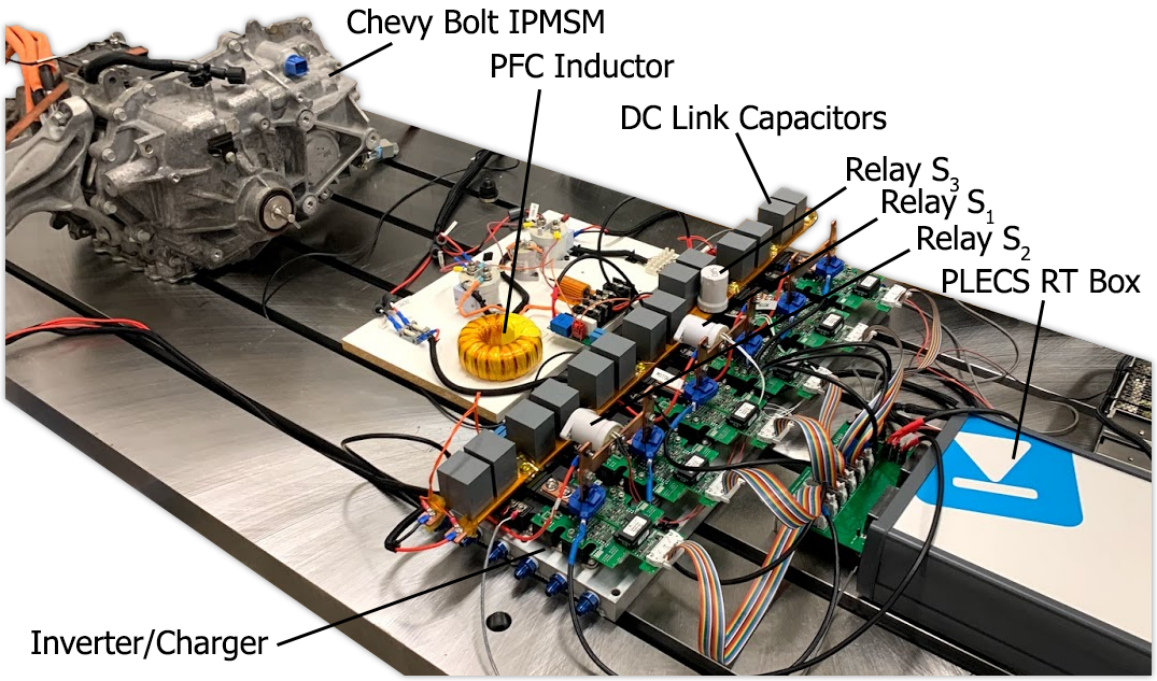

Figure 6.10: Experimental setup.

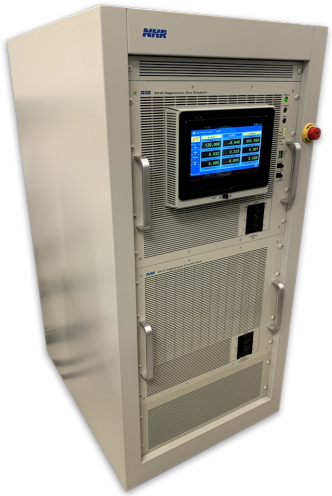

Figure 6.11: NHR 9410 bidirectional AC/DC supply and grid simulator.

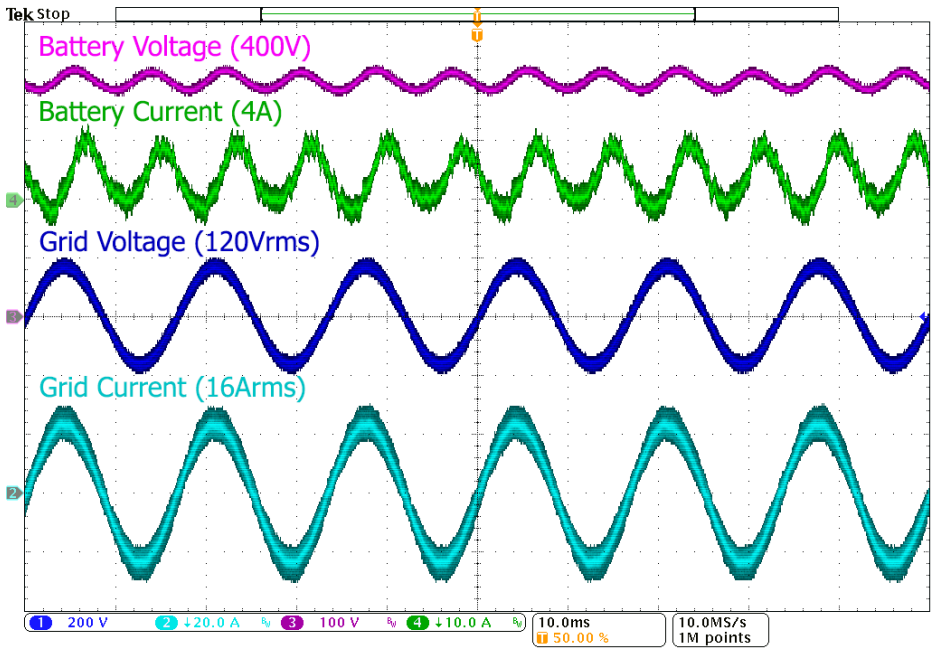

Figure 6.12: 120Vac to 400Vdc charging.

6.14. Additional harmonic content exists around the effective switching frequency and multiples thereof. Including the switching frequency harmonics, THD is measured to be 6%. All lower order harmonics are below 2% of the fundamental. Some additional current appears at the 13th harmonic due to the bandwidth of the PFC current loop, which could be improved with further tuning or filtering.

The PFC stage PWM voltage v_{pwm} is shown in Figure 6.13.

As expected, v_{pwm} lags the grid voltage such that the resultant current is in phase with the grid voltage according to:

$$i_{ac} = \frac{v_{ac} - v_{pwm}}{j\omega L_{ac} + R_{ac}} \tag{6.40}$$

To demonstrate the functionality benefits of the proposed IBC topology, V2G operation

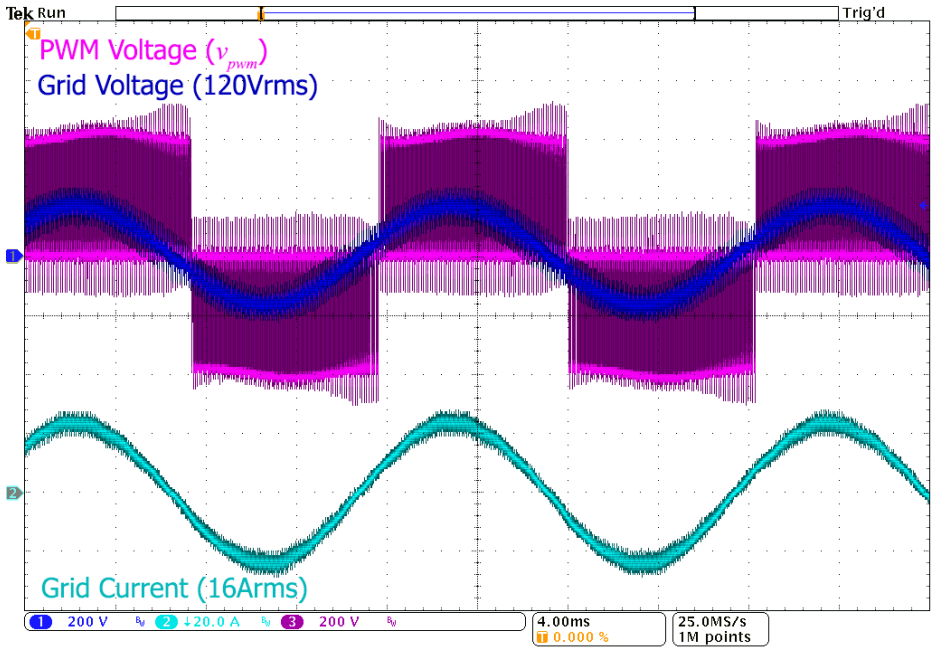

Figure 6.13: 120Vac to 400Vdc charging.

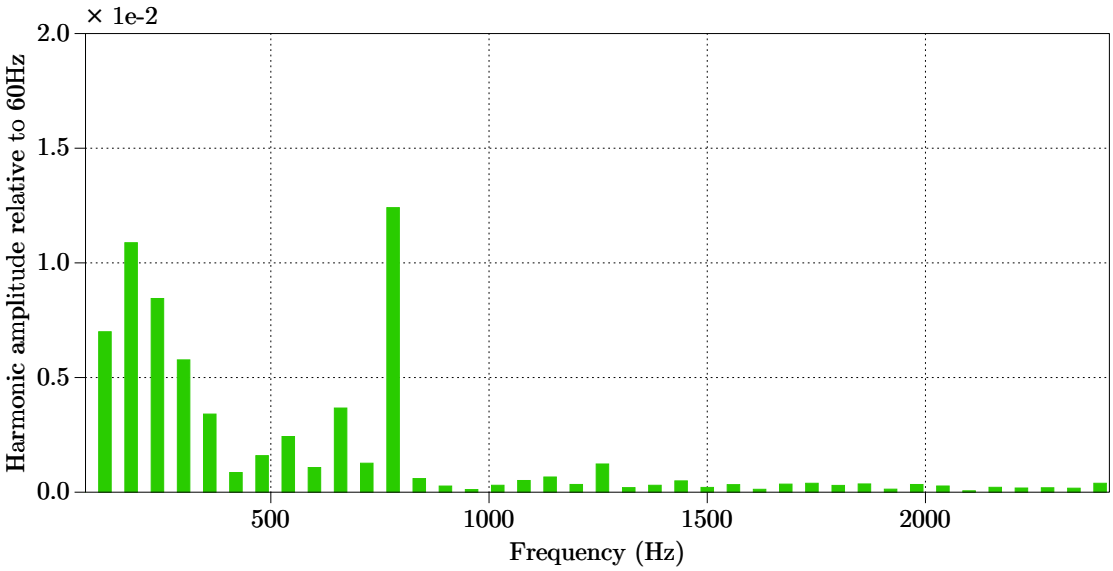

Figure 6.14: 120Vac charging grid current harmonic spectrum from 2nd to 40th harmonic.

is implemented and experimentally validated. Figure 6.15 shows supplying 1.9kW to the grid from the 400Vdc battery. The grid current is 180 degrees out of phase with the grid voltage and v_{pwm} now leads the grid voltage. This is achieved by simply changing the sign of i_d^* current reference in the decoupled DQ current controller shown in Figure 6.8.

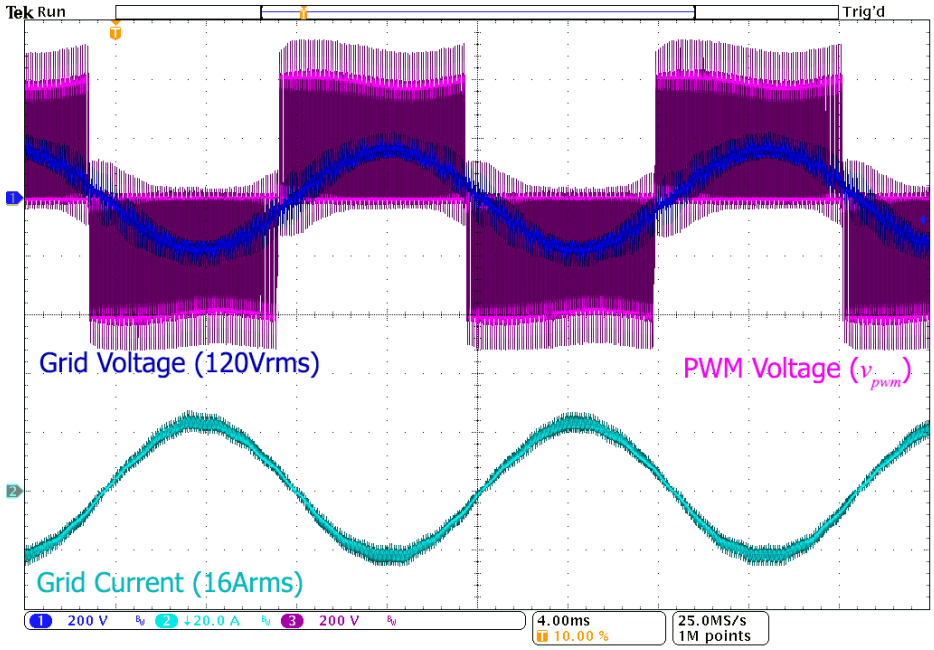

Figure 6.15: 400Vdc to 120Vac V2G operation.

6.5.2 240Vac to 200Vdc Charging

Buck operation is demonstrated with 240Vac to 200Vdc charging. The peak grid voltage is $240\sqrt{2}$ or 339V which is significantly higher than the 200Vdc bus, representative of a battery pack at low SoC. The boost PFC stage first rectifies the 240Vac to a 500Vdc intermediate bus on the phase B and C side of relay S_3, which is open. The 500Vdc bus is then stepped down to 200Vdc with the cascaded DC/DC converter

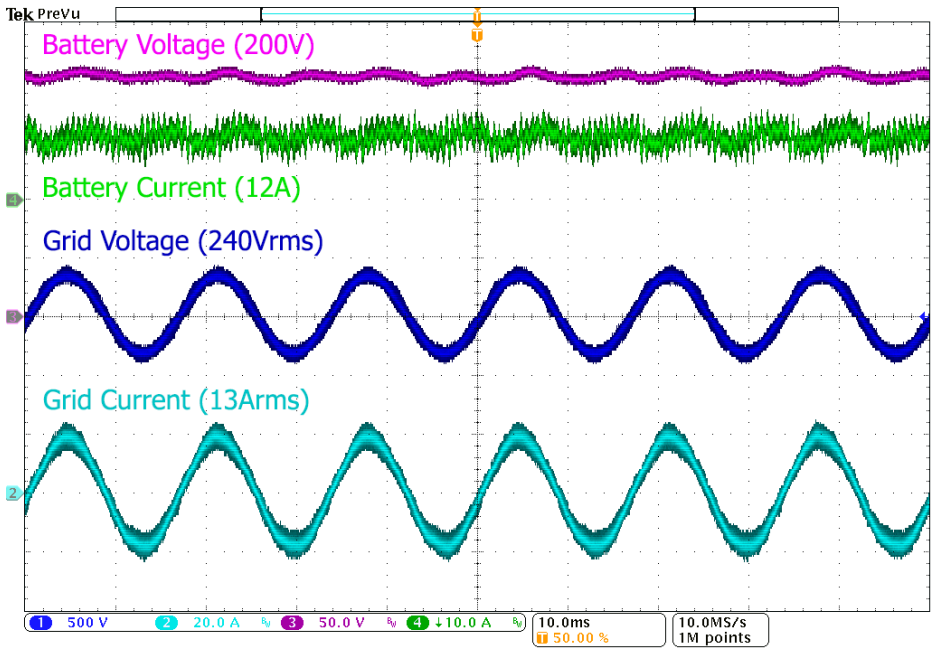

Figure 6.16: 240Vac to 200Vdc charging.

formed with the motor winding inductance and phases B_2 and A_2. Fig. 6.16 shows the buck mode of operation, again indicating good power factor. The 120Hz ripple component of the output current is significantly attenuated by the DC/DC converter action. A harmonics analysis of the grid current up to the 40th harmonic is shown in 6.19. Additional harmonic content exists at the effective switching frequency and multiples thereof. Including the switching frequency harmonics, THD is measured to be 10%. All lower order harmonics are below 2% of the fundamental.

The PFC stage PWM voltage v_{pwm} is shown in Figure 6.17. Additionally, the intermediate 500V DC link voltage is shown in Figure 6.18, which exhibits 120Hz ripple.

The motor winding currents are shown in Figure 6.20. Positive current is defined as flowing into the motor. Phases B and A conduct the expected inductor current for the

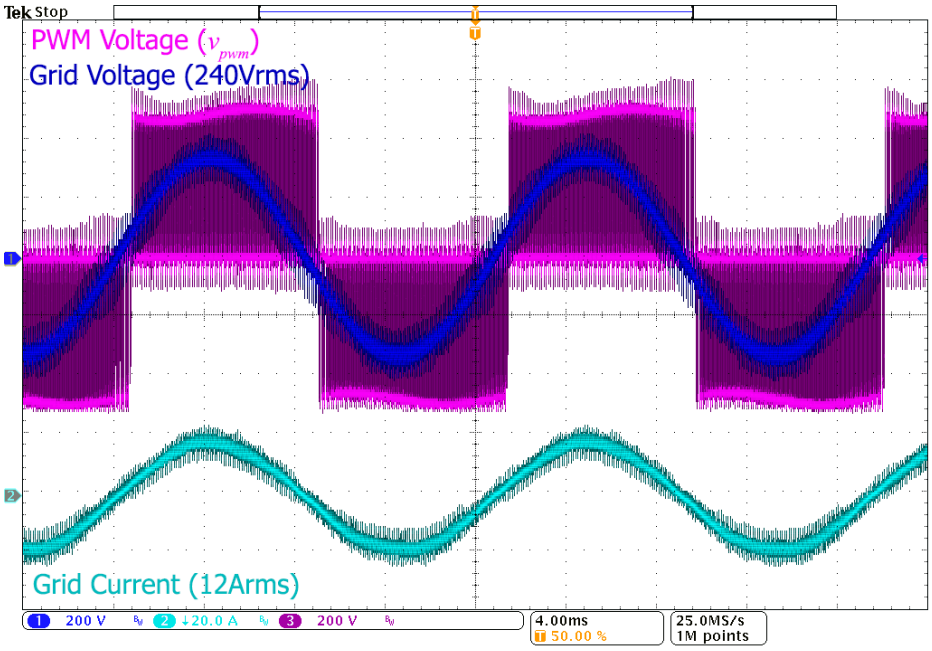

Figure 6.17: 240Vac to 200Vdc charging.

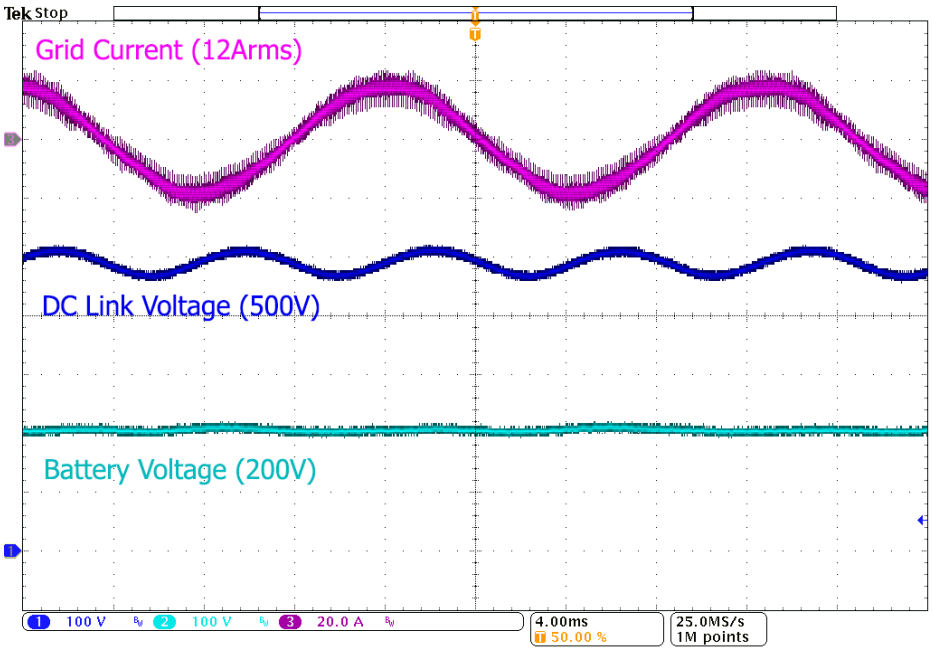

Figure 6.18: 240Vac to 200Vdc charging, 500V intermediate DC link exhibits 120Hz ripple

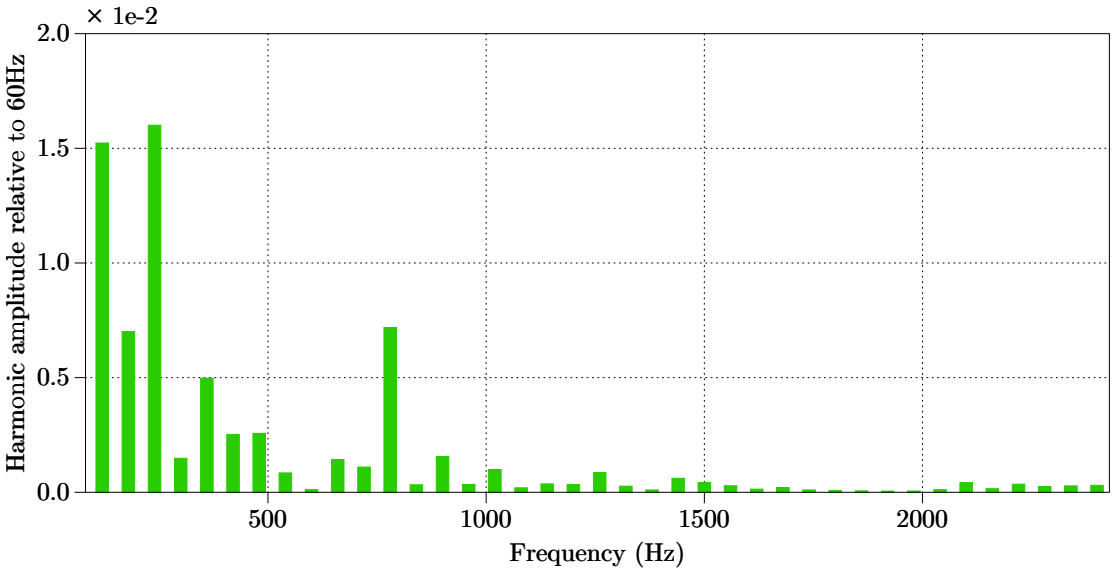

Figure 6.19: 240Vac charging grid current harmonic spectrum from 2nd to 40th harmonic.

DC/DC buck converter, while no current flows in Phase C.

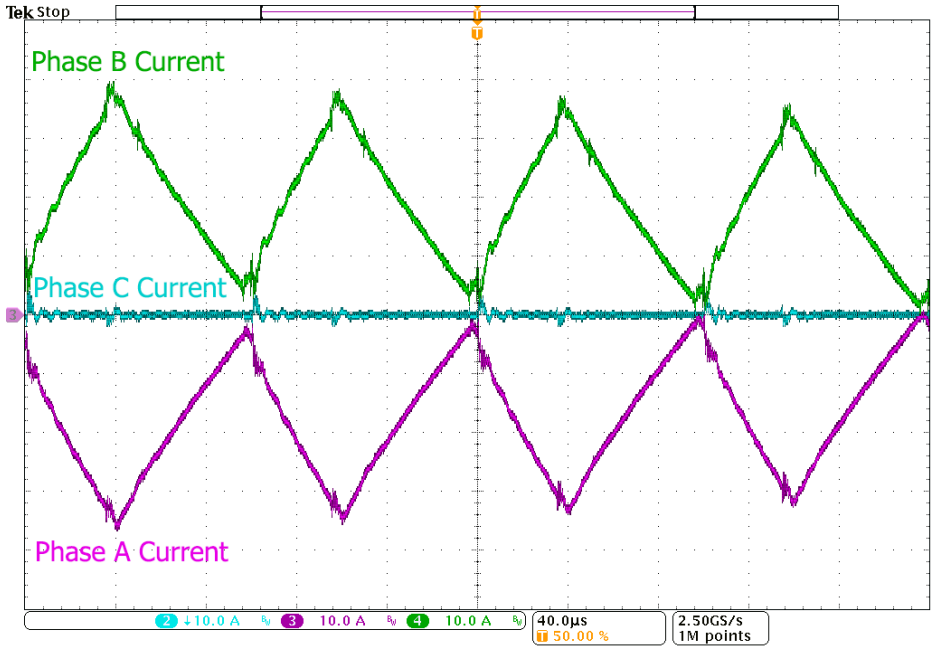

Figure 6.20: Motor phase currents during 240Vac to 200Vdc charging

V2G operation supplying a 240Vac grid from a 200Vdc battery is shown in Figure

6.21.

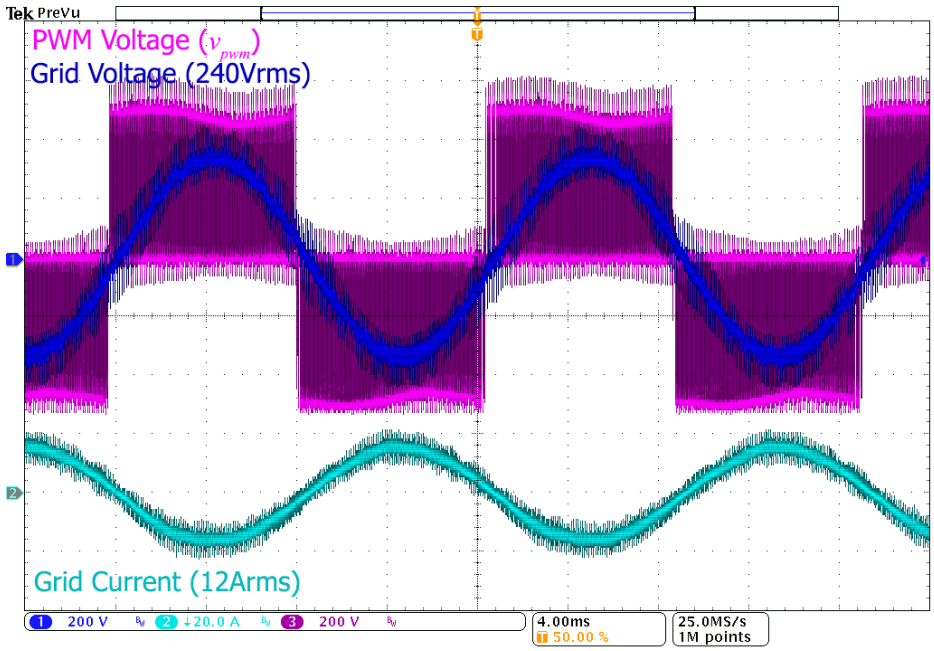

Figure 6.21: 200Vdc to 240Vac V2G operation.

The 200Vdc supply is boosted to a 500Vdc intermediate DC link voltage, which is then inverted to supply the AC grid. The DC/DC boost converter allows V2G operation over the range of battery pack voltages. For example, a fully charged battery pack may start at 400Vdc and discharge towards 200Vdc as the SOC declines. The boost converter maintains a constant intermediate bus such that the grid voltage can be maintained even as the battery pack voltage declines below the peak grid voltage.

6.5.3 200Vdc to 400Vdc Charging

In this configuration, the boost PFC stage in unused, and the battery is charged from a DC source such as a DC fast charger, in the case where the output voltage range of the DC fast charger is incompatible with the voltage range of the battery. Fig.

6.22 illustrates charging of a 400V battery from a 200Vdc source using the DC/DC converter. The inductor (motor winding) current indicates the converter is operating in continuous conduction mode, while the output battery current exhibits low ripple.

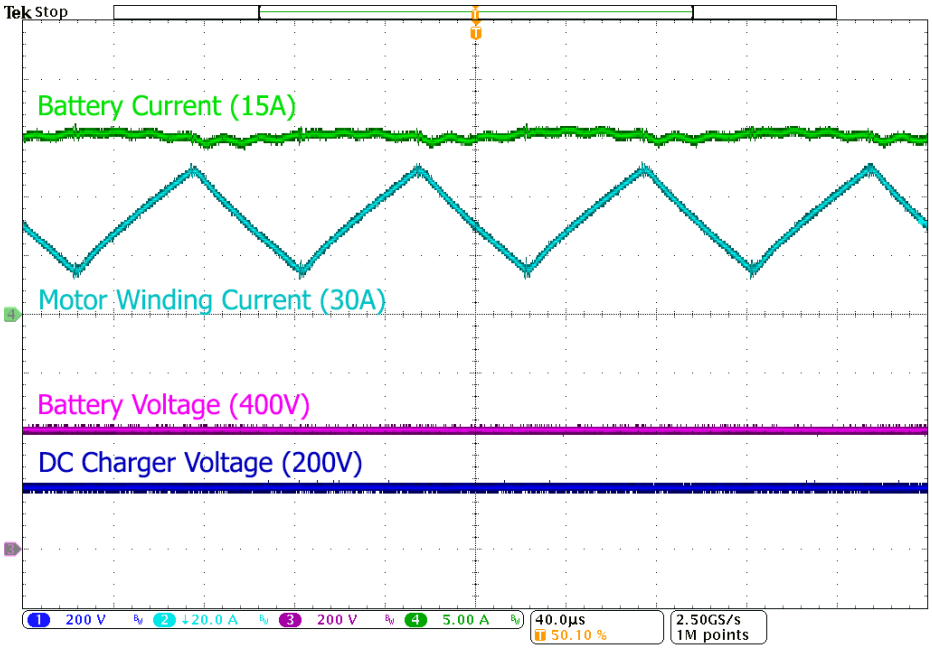

Figure 6.22: 200Vdc to 400Vdc charging.

The motor phase currents are shown in Figure 6.23. Phase B and C conduct the same average current, with the current ripple determined by the magnitudes of the individual inductances. Phase A conducts the sum of the phase B and C currents.

The input current (supplied by the DC fast charger) in conjunction with the DC/DC converter switching waveforms is shown in Figure 6.24. The input current exhibits 4A peak-to-peak ripple at the switching frequency when operating at 6kW.

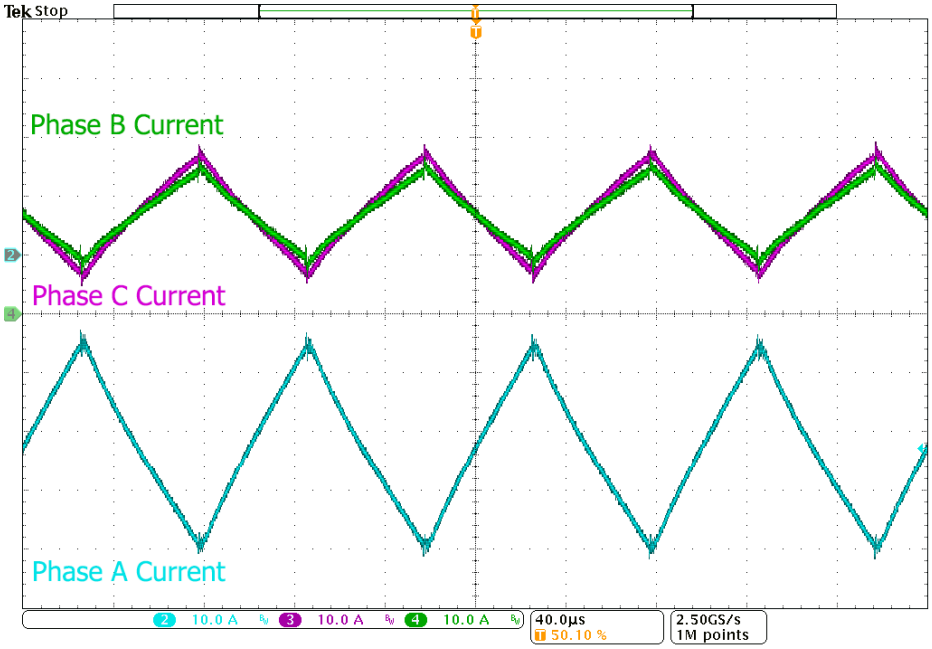

Figure 6.23: Motor phase currents in DC/DC operation.

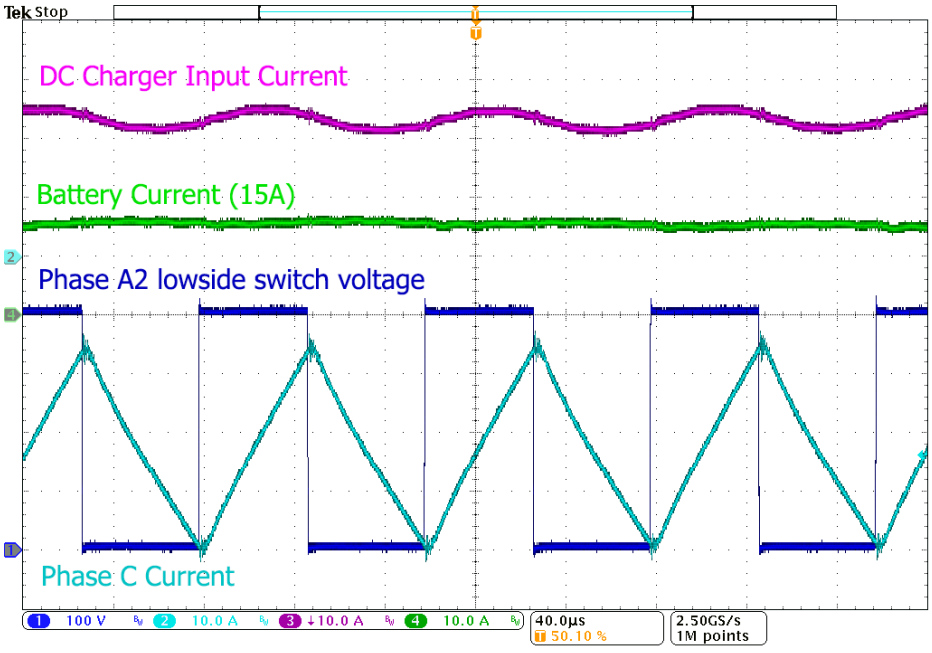

Figure 6.24: Input Current Ripple in DC/DC operation.

6.5.4 Motoring Mode

In the motoring mode, all relays S_1, S_2 and S_3 are closed and the converter is operated as a conventional three phase VSI. Phase currents are shown in Figure 6.25 indicating proper VSI operation.

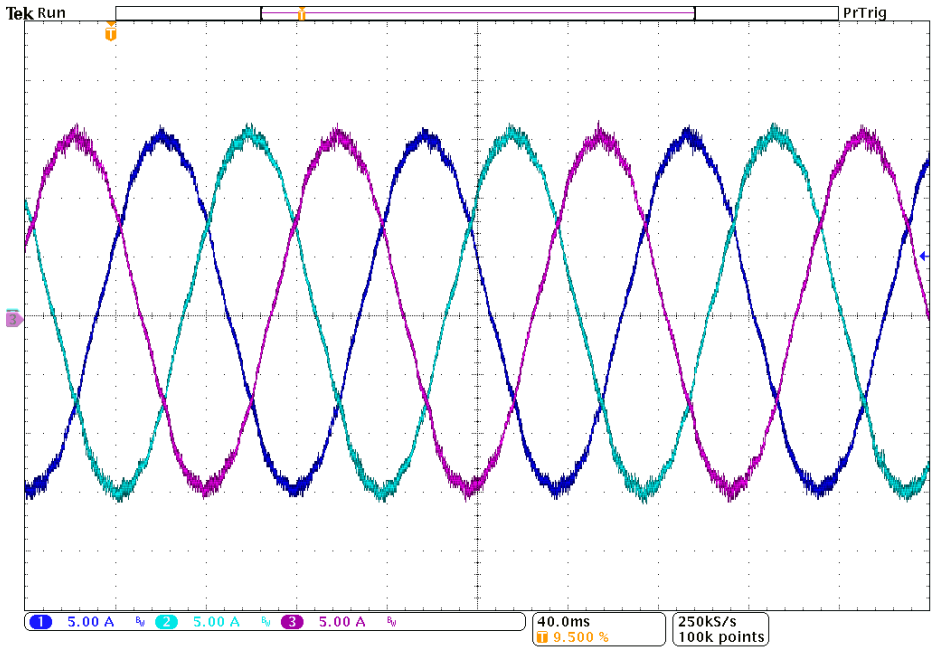

Figure 6.25: Phase A, B, and C motor currents, i_q^* =15A.

While the aggregate phase currents are as expected, it is also important to consider the current sharing between individual paralleled phases. Figure 6.26 shows the total phase B current and the individual phase B_1 and B_2 currents, indicating B_1 and B_2 share the total current equally.

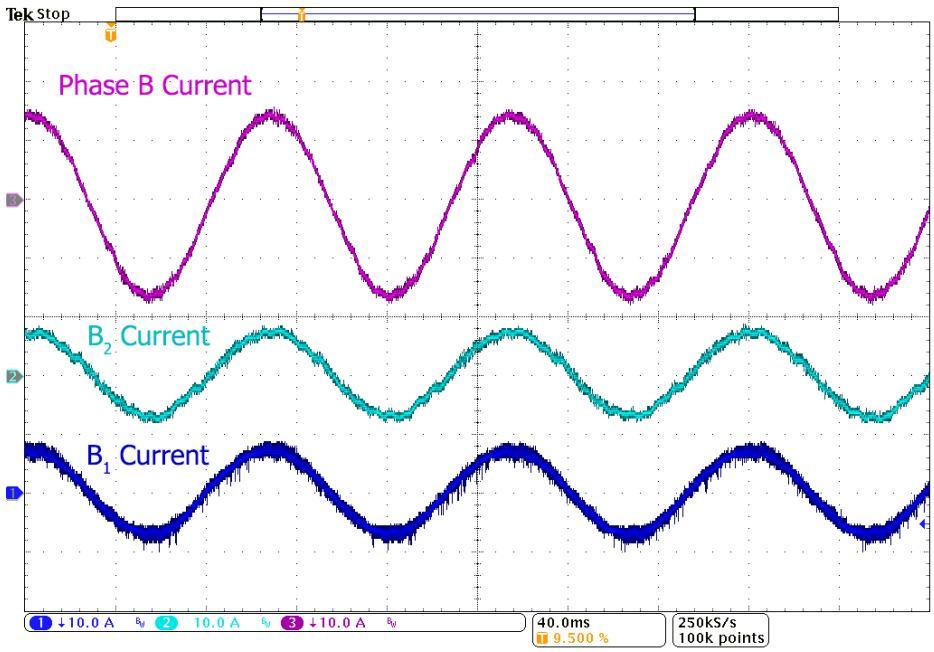

Figure 6.26: Phase B current sharing: phases B_1 and B_2 evenly share the total phase B current.

6.6 Practical Considerations

The experimental results presented in Section 6.5 demonstrate the various operating modes of the converter. In this section, some additional practical considerations for the implementation of the integrated converter are discussed. Waveforms captured from the prototype implementation are used to demonstrate the considered effects.

6.6.1 Relay Parasitics

To implement the proposed IBC topology, the addition of three relays to the base inverter is required. In the prototype implementation, high voltage, high current DC contactors are used. Contactors typically have contact resistances less than 1 mΩ, as

low as 0.1 mΩ. Therefore any I^2R losses in the contactor can be considered fairly negligible at typical phase currents. As shown in Figure 6.26, the small additional resistance of the contactor connecting the paralleled phases also has negligible effect on the current sharing.

Of greater concern is the potential parasitic inductance introduced by integrating a contactor into the DC bus structure, as is required for relay S_3. The large di/dt that occurs during device turn off induces a voltage across any parasitic inductance in the commutation loop which sums with the DC link voltage, such that the voltage across the device "overshoots". This is of even greater concern with WBG devices which have di/dt rates many times higher than silicon IGBTs. A planar busbar structure is typically used to minimize the commutation loop area, thus minimizing the parasitic inductance. The introduction of a series relay in the DC link interrupts the planar structure, introducing undesirable parasitic inductance in addition to any partial inductance resulting from relay construction itself.

Most traction inverters, as shown in Chapter 2, use either a single bulk DC link capacitor, or three DC link capacitors with connections for each phase. To negate the effect of any parasitic inductance introduced by S_3, a distributed DC link capacitor scheme is used in the experimental converter implementation. The capacitor, power module, and contactor arrangement is shown in Figure 6.27. By placing DC link capacitance between the power module terminals and the contactor, the contactor is effective removed from the commutation loop and the effect of any parasitic inductance negated. This is verified by measurements of the high side IGBT collector-emitter voltages V_{ce}, shown in Figure 6.28. The phases directly on either side of the contactor, B_1 and A_2 both exhibit acceptable overshoot voltage during turnoff, at 13% and 16%

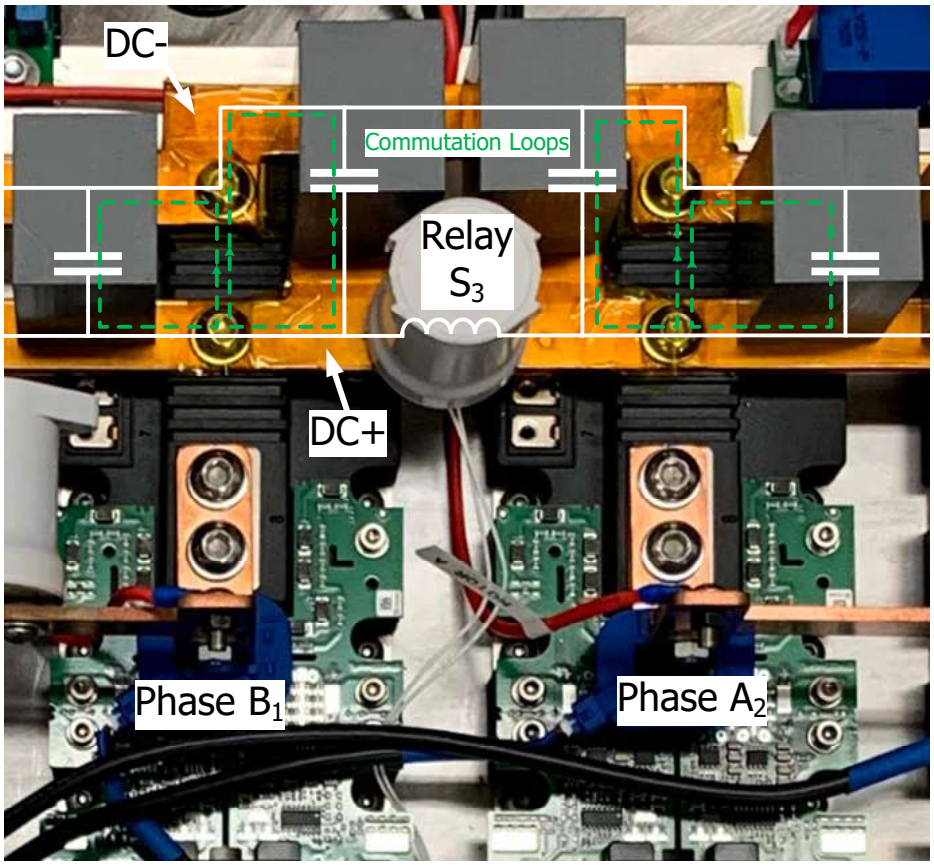

Figure 6.27: Relay S_3 physical layout with distributed DC link capacitors and commutation loops.

respectively, with a 200V DC link.

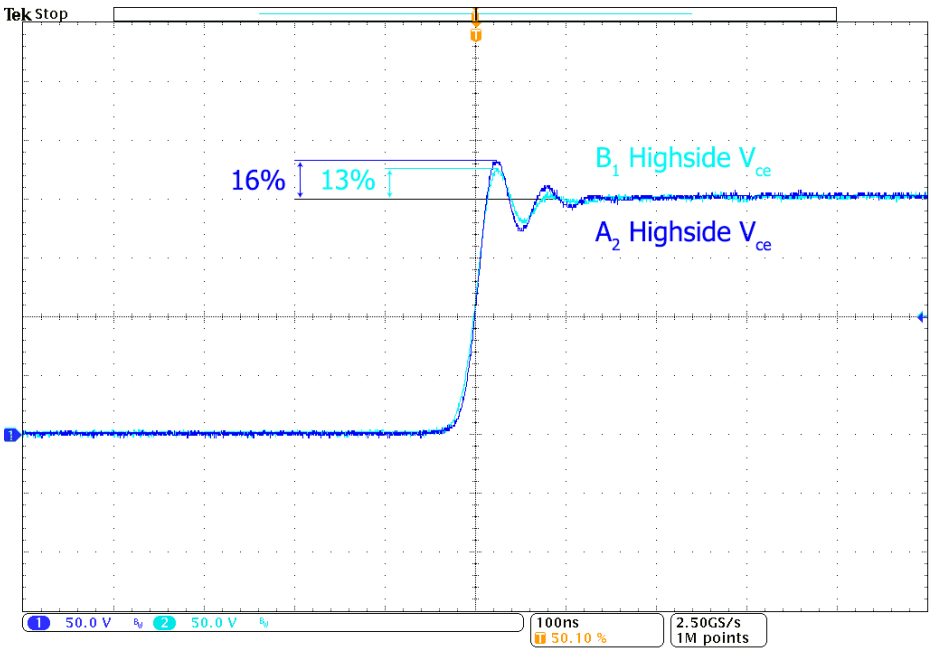

Figure 6.28: Phase A2 and B2 turn off overshoot voltages switching $I = 15$A.

6.6.2 Capacitor Voltage Balancing

Due to the distributed DC link capacitor arrangement, the voltages of capacitors C_{dc1} and C_{dc2} may need to be equalized before S_3 can be safely closed. This can be achieved without any additional hardware due to the bidirectional capability of the integrated DC/DC converter. The converter can be operated briefly after having removed the external AC or DC supply to bring C_{dc2} to the battery voltage, allowing S_3 to be closed.

6.6.3 Common Mode Voltages

Alternating common mode voltages in power converters tend to result in common mode current flow. Parasitic capacitances, particularly between power semiconductor devices

and their heatsinks, will conduct current induced by the common mode voltage dv/dt. As discussed in Chapter 3, common mode leakage currents are a potential safety issue if they are large enough in magnitude. Additionally, high frequency common mode currents tend to radiate significantly more than differential mode currents, resulting in radiated EMI challenges [198]. In the experimental implementation, the DC side Y-capacitors are disconnected during the charging operation to prevent leakage current flow.

For an AC rectifier the common mode voltage V_{cm} can be defined as

$$V_{cm} = \frac{V_{DC+N} + V_{DC-N}}{2} \tag{6.41}$$

where V_{DC+N} and V_{DC-N} are the voltages between the DC poles and AC neutral conductor. The neutral conductor is assumed to be at the same potential as the heatsink, as they are both connected to earth ground.

The full bridge boost rectifier exhibits a common mode voltage which swings between $+V_{dc}/2$ and $-V_{dc}/2$ at the switching frequency, as measured in Figure 6.29. As discussed in Chapter 3, if the DC side Y-capacitors connected, a leakage current would flow due to the alternating CM voltage at the switching frequency.

Totem Pole Bridgeless PFC

To reduce the common mode current flow, either the dv/dt itself or the frequency of the V_{cm} dv/dt swings must be reduced. Reducing the dv/dt is undesirable as this increases the switching losses in the converter. Therefore to reduce the frequency of the V_{cm} dv/dt swings, alternative rectification techniques should be considered. One

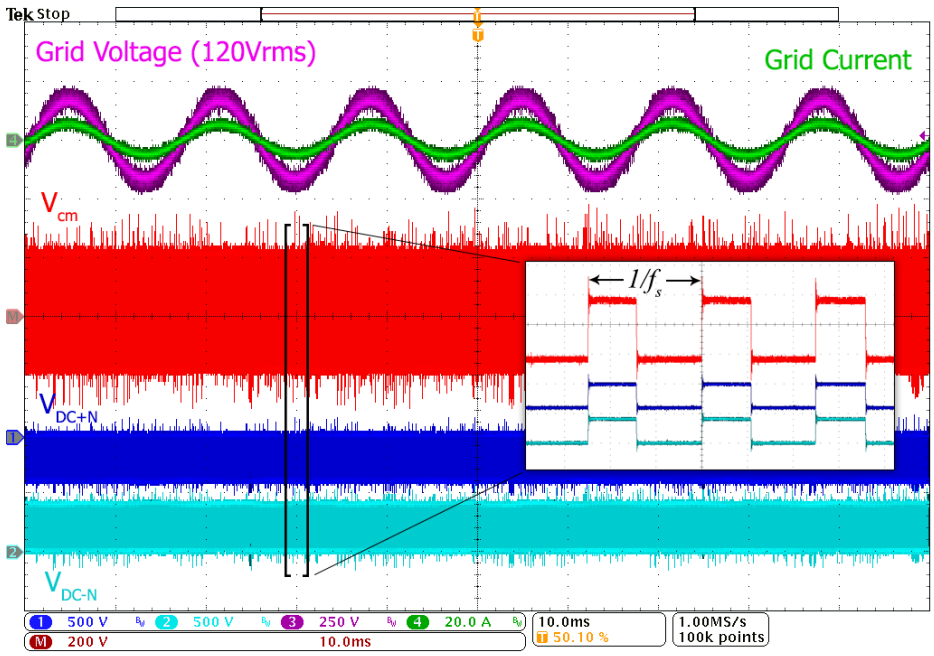

Figure 6.29: Full bridge boost rectifier common mode voltage.

such alternative is the totem pole bridgeless PFC, shown in Figure 6.30

The totem pole PFC converter effectively operates as two distinct boost converters, one operating during the positive half cycle, and one during the negative half cycle. The diode leg only commutates at each half cycle, such that the common mode voltage swings occur at the line frequency. This significantly reduces the common mode current compared to the full bridge boost rectifier. The experimental setup controller was modified to operate the AC frontend as a totem pole PFC. In the diode leg, the IGBT switches are turned off and only the antiparallel diodes conduct. The common mode voltage is measured and shown in Figure 6.31.

Indeed the radiated EMI caused by the CM current is noticeably reduced in the measured signals. The totem pole PFC does have some disadvantages when compared to the full bridge boost rectifier however:

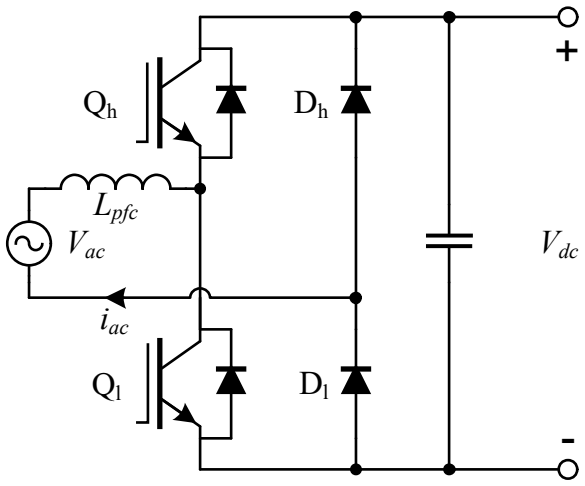

Figure 6.30: Totem pole bridgeless PFC

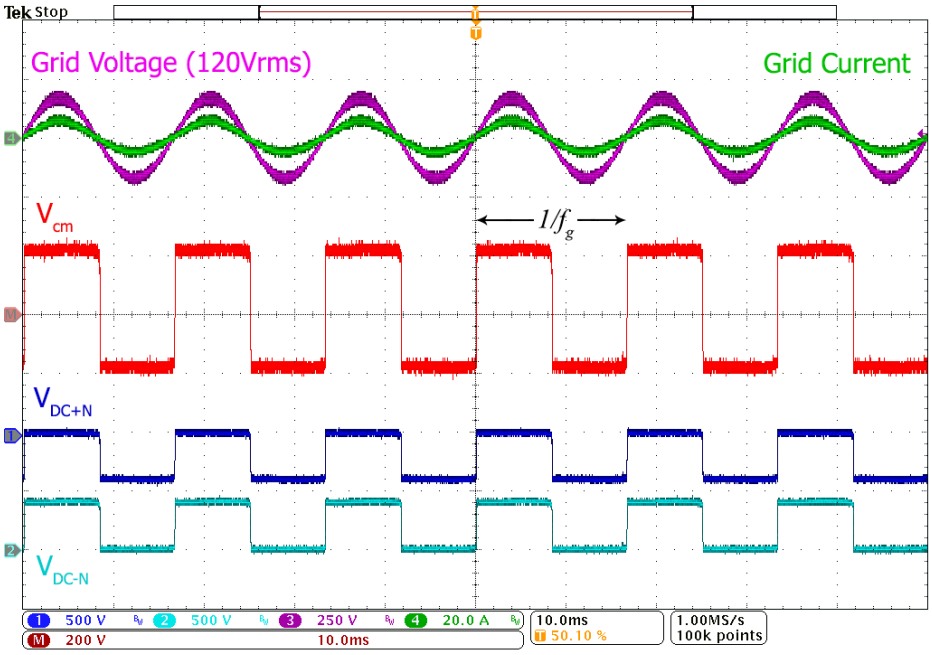

Figure 6.31: Totem pole PFC common mode voltage.

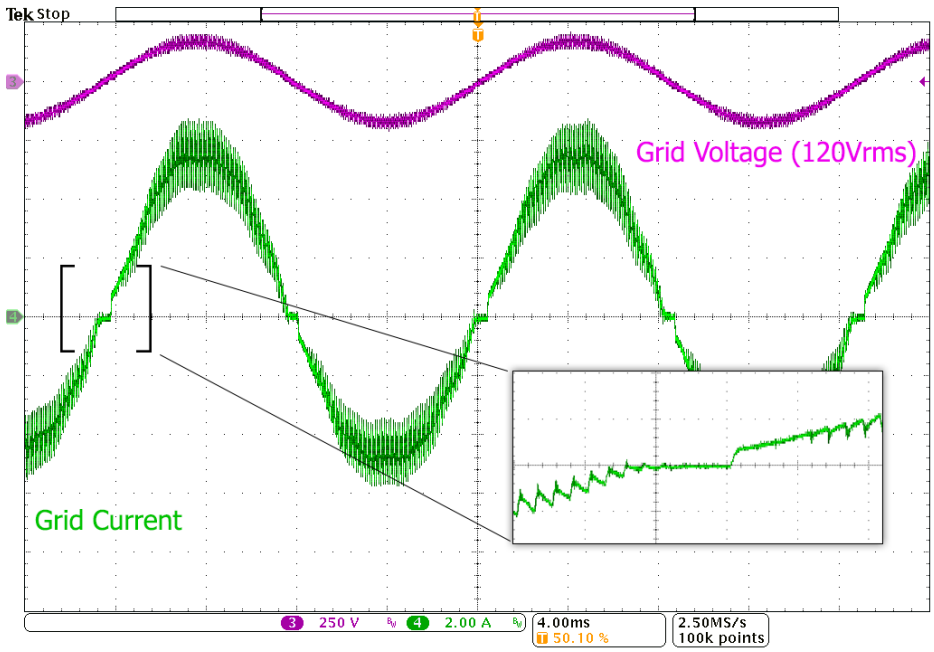

Figure 6.32: Totem pole PFC zero crossing distortion.

1. The diode leg requires diodes with negligible reverse recovery charge, and is therefore not suitable for integration with silicon based traction inverters.

2. The effective switching frequency is half that of the full bridge boost rectifier, requiring additional filtering and a larger boost inductor to achieve the same current ripple and conducted EMI performance

3. As the boost converter duty cycle saturates near the voltage zero crossings, zero crossing distortions appear in the grid current, shown in Figure 6.32.

The first two disadvantages can be fairly easily remedied with SiC devices, which have already been established as the technology of choice for future traction inverters in Chapter 2. Indeed the diode leg can be implemented through synchronous rectification with SiC MOSFET devices. The zero crossing distortion can also be resolved through controls also enabled by the higher switching frequency capabilities of WBG devices

[199].

Though additional work is required to address all of the practical considerations in implementing this IBC topology, solutions or potential solutions for the following primary challenges have been presented:

1. Torque production and requirements for reaching a zero torque rotor position
2. Electrical considerations for introduction of relay or contactor devices into the traction inverter
3. Potential solutions for reducing the CM leakage current

6.7 Conclusions

A new IBC topology with universal (AC/DC) charging input capabilities is proposed. The single-phase AC charging mode can achieve the functionality of a typical OBC, while the DC charging mode can enable compatibility between current generation 400V DC fast chargers, and emerging 800V powertrains. The charging modes are achieved through the addition of three relays and one inductor to an inverter constructed from at least two paralleled phase legs per phase. The inverter is operated as a conventional three-phase VSI during the driving mode, with no modifications required to the machine or motor control strategy. The machine winding inductance is used to form a DC/DC converter which allows charging any voltage battery pack from any AC or DC source regardless of their relative voltages.

A decoupled model of the phase inductances and torque production for a standard

three-phase IPMSM is used to predict the available winding inductance for the DC/DC converter, and the existence of certain rotor positions in which no torque is produced during charging. Control strategies for single-phase PFC and DC/DC converter operation are described. Experimental results validate AC charging modes in which the peak grid voltage is both higher and lower than the battery voltage, showing good power factor of the AC input current. DC charging is demonstrated with a step up scenario, charging a higher voltage battery pack from a lower voltage DC source.

The L_d and L_q parameters of the motor used in the experimental setup were calculated from measured line-to-line inductances over a range of rotor positions. These parameters can vary with phase current and temperature, among other conditions, so care must be taken in ensuring controller stability over the range of potential values. For a battery charging application, the transient response requirements are relatively minimal, allowing the controllers to be conservatively tuned ensuring stability over a the range of plant transfer functions.

It should also be noted that wye-connected machines are considered as they are prevalent in traction applications over delta-connected machines. In the case of a delta-connected machine, a similar topology may be applied, however the windings would be configured as two in parallel with the third unused. This would present a lower equivalent inductance than the parallel wye-connected configuration, which is undesirable for DC/DC converter operation.

The proposed topology may also be generalized to three phase charging, with the addition of more paralleled inverter legs. This is not unreasonable, as current production traction inverters may use four, six or more paralleled discrete devices per switch [10].

Additional experimental results demonstrate the practical considerations with respect to integrating relays in the DC bus. A totem pole PFC AC front end is also implemented and common mode voltage characteristics compared against the full bridge boost rectifier. Overall, the limited number of additional required components in the proposed topology and compatibility with existing machine designs result in a potentially practical solution suitable for general automotive applications.

Chapter 7

Conclusions and Future Work

7.1 Conclusions

This thesis presents the context, conceptual development, and validation of new integrated traction inverter and battery charger topologies.

The motivation for IBC topologies is presented, particularly the potential benefits in terms of cost, weight and volume for the overall power electronics system in EVs. The need for further development of integrated solutions that minimize the impact on existing powertrain designs is identified. To maximize the benefits and applicability of an integrated solution, the topology should work with standard electric machine configurations and require no external interface converters or DC/DC converters.

To establish a basis for new integrated designs, a detailed analysis of several conventional production traction inverters is presented based on publications and reverse engineering efforts, including designs from recent model year GM, Toyota, Nissan,

BMW, Audi, and Tesla vehicles. Based on the surveyed production inverters and ongoing industry and academic research, future trends in traction inverter design are identified. One such trend is the integration of the vehicle power electronics at a mechanical level, which is beginning to be implemented by several manufacturers.

It is proposed that future traction inverter designs may pursue integration further at the electrical level. Integration can therefore be seen as a system level alternative to increasing the power density of individual converters directly. Integration of the battery charger and traction inverter to form an IBC is identified as having the most potential benefit in terms of system level power density. Common challenges for IBCs are presented, including galvanic isolation, which is discussed along with possible solutions. A review of existing IBC topologies in the literature is presented. Additional challenges are identified in many of the proposed topologies, including the use of nonstandard machine designs and requirements for non-integrated power electronics components.

A theoretical basis for the development of integrated charger topologies is established. By breaking down any converter circuit into its fundamental three-terminal cells, it becomes apparent how converters can be transformed and cascaded to achieve new conversion functionality. While the functionality of the semiconductor switches remains essentially unchanged between the driving and charging modes, the role of the electric machine is entirely different. To predict the available winding inductance and torque production in the electric machine during charging, a decoupled stator reference frame model of an IPMSM is developed from first principles. The winding inductance and torque production during charging are quantified through application of the model. The existence of zero torque conditions is established for two possible

winding configurations, indicating the suitability of the machine to be used as an inductor in the integrated converter circuit.

A new IBC topology for four-phase SRM based powertrains is proposed. In the motoring mode, the topology operates as a conventional asymmetric bridge converter. In the charging mode, three phases are used to form a boost rectifier while the last phase forms a non-inverting buck-boost converter. A control scheme is developed to achieve power factor correction of the input grid current under the inherently unbalanced input impedance conditions presented by the topology. Buck and boost mode operation of the DC/DC converter stage is demonstrated at 32 and 16 kW respectively. Output voltage ripple was found to be below 1%, making the topology suitable for constant voltage charging. Compared to a standard four-phase asymmetric bridge converter, the proposed A+HB converter requires three additional IGBT switches, three additional diodes and two relays. This represents a significant improvement in power over typical existing dedicated OBC systems with a minimal number of additional required components.

A second new IBC topology with universal (AC/DC) charging input capabilities is proposed. The single-phase AC charging mode can achieve the functionality of a typical OBC, while the DC charging mode can enable compatibility between current generation 400V DC fast chargers, and emerging 800V powertrains. The charging modes are achieved through the addition of three relays and one inductor to an inverter constructed from at least two paralleled phase legs per phase. The inverter is operated as a conventional three-phase VSI during the driving mode, with no modifications required to the machine or motor control strategy. The machine winding inductance is used to form a DC/DC converter which allows charging any voltage battery pack

from any AC or DC source regardless of their relative voltages. Experimental results validate AC charging modes in which the peak grid voltage is both higher and lower than the battery voltage. DC charging is demonstrated with a step up scenario, charging a higher voltage battery pack from a lower voltage DC source. Additional results demonstrate the functionality benefits of the IBC topology through V2G operation. A distributed DC link capacitor arrangement is experimentally shown to mitigate the potential impacts of integrating a relay into the DC bus. The totem pole boost rectifier is proposed as a means to reduce the potential for CM leakage current and experimentally shown to reduce the CM voltage fundamental from the switching frequency to the grid frequency. The proposed topology implements both the functionality of a conventional OBC and that of new DC/DC converters for 400V fast charger compatibility, while adding V2G capabilities. No special requirements on the machine design results in a practical solution suitable for general automotive applications.

In Chapter 3, motivations for integration are presented and a comparison of a discrete and mechanically integrated OBC conducted. To demonstrate the benefits of going beyond mechanical integration and electrically integrating the charger at the topology level, a final comparison is conducted based on the integrated charger for conventional machines proposed in Chapter 6. Since it is difficult to compare the costs of a production part with a prototype implementation, an approximate comparison is done by removing costs from the mechanically integrated charger which are eliminated by the proposed integrated topology. When compared with the mechanically integrated OBC:

1. EMI filter cost remains the same.

2. Power magnetics cost remains the same. The isolation transformer is in fact eliminated, however this is the result of implementing a non-isolated charger topology, rather than specifically due to the electrical integration, so it will not be counted here.

3. Power semiconductor costs are eliminated, as all power semiconductors are already required for the traction inverter.

4. DC link capacitor costs are eliminated, as the DC link capacitors are already required for the traction inverter.

5. Control board cost is assumed to be reduced by 50%, as the inverter control board can be used for the charger. The remaining cost accounts for the doubled gate driver and current sensing circuitry now required in the inverter.

6. Enclosure/heatsink cost is assumed to be reduced by 50%, as the heatsink for the charger power semiconductors is eliminated.

7. The additional relays added to the converter are assumed to add 10% to the total cost.

Based on these assumptions, the IBC is expected to cost approximately 43% of a discrete charger, or a further 27% reduction to the cost of a mechanically integrated charger. The cost breakdown comparison for the discrete charger, mechanically integrated charger, and electrically integrated charger (IBC) is shown in Figure 7.1.

New IBC topologies represent an opportunity to facilitate wider adoption of electric vehicles though reduced costs and improved functionality. Potential topologies should be carefully considered to ensure they maximize the benefits of integration while

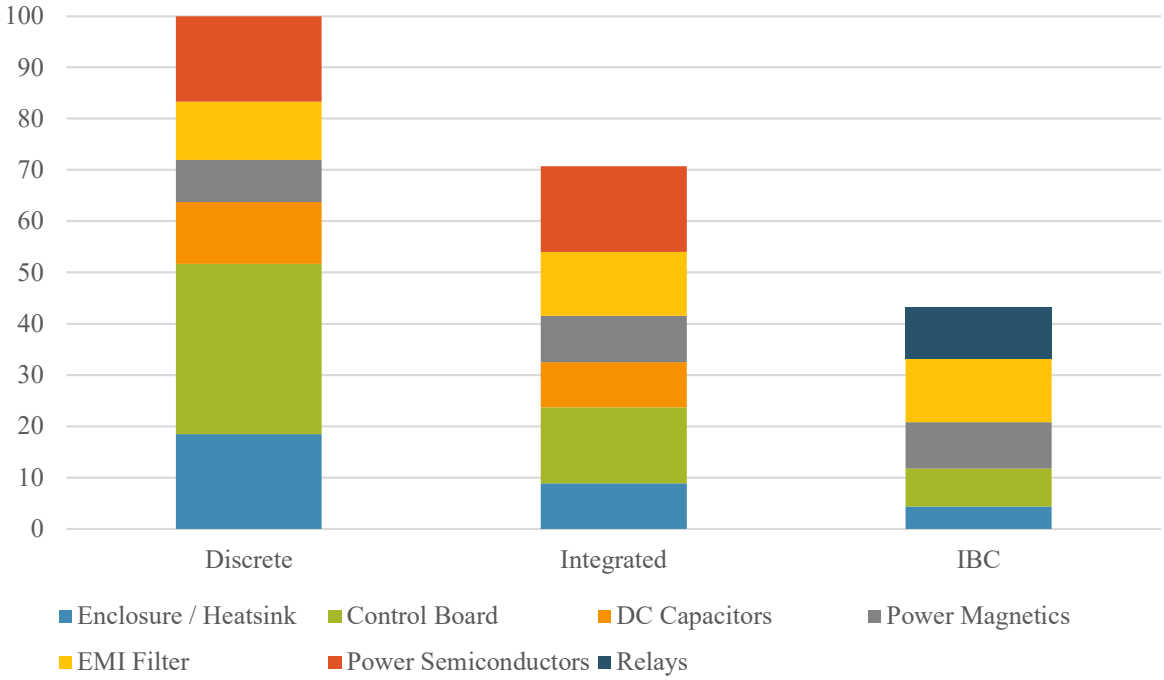

Figure 7.1: Comparison of discrete, mechanically integrated and electrically integrated (IBC) cost breakdown.

avoiding the identified challenges. By breaking down the traction inverter into its fundamental elements, new integrated converters can be realized for battery charging functionality. Two new IBC topologies have been proposed and analyzed. Experimental validation and cost analysis of the IBC for conventional machines demonstrates the benefits of the proposed topology.

7.2 Future Work

The following future work is suggested to further develop the proposed IBC topologies:

1. Implementation of the IBC topology for conventional machines with discrete SiC devices. The higher switching frequency capabilities of SiC can enable a

reduction in the PFC inductor size and allow a higher efficiency totem pole PFC frontend to be implemented. Finally, the DC/DC converter operation switching frequency can be increased, reducing the current ripple in the machine windings which results in AC copper losses. The increased switching frequency can also help reduce acoustic noise in the machine during charging, which is important for consumer automotive applications.

2. In addition to characterization of the machine losses, the inverter losses in the charging modes can be further characterized to determine the thermal management requirements relative to the inverter mode. Requirements for operation of liquid cooling systems for both the inverter and machine during charging can be established.

3. Evaluation of CM leakage currents and resulting touch currents as described in [129]. For a commercial implementation of the proposed topology, the lack of galvanic isolation must be demonstrated to be safe.

4. Implementation of the AC line EMI filter to meet required harmonic standards. The measured THD indicates additional filtering on the AC front end is needed.

5. Experimental validation of the proposed IBC topology for SR machines, with a four phase SRM. Implementation of a more robust negative sequence controller.

6. Investigation into the implementation of normally closed (NC) relays for integrated converters. The contactors used in the experimental implementation described in Chapter 6 are designed to reliably interrupt DC currents of hundreds of amps for many cycles. This design requirement increases the cost and size of the implementation. In an integrated charger application, the relays are

only actuated under zero current, zero voltage conditions, which can greatly simplify their design. Additionally, solid state reconfiguration mechanisms implemented with conduction loss optimized (low $R_{ds(on)}$) MOSFET devices can be investigated.

References

[1] T. Trigg, P. Telleen, R. Boyd, F. Cuenot, D. DAmbrosio, R. Gaghen, J. Gagné, A. Hardcastle, D. Houssin, A. Jones *et al.*, "Global EV outlook: understanding the electric vehicle landscape to 2020," *Int. Energy Agency*, vol. 1, pp. 1–40, 2020.

[2] R. K. Pachauri, M. R. Allen, V. R. Barros, J. Broome, W. Cramer, R. Christ, J. A. Church, L. Clarke, Q. Dahe, P. Dasgupta *et al.*, *Climate change 2014: synthesis report. Contribution of Working Groups I, II and III to the fifth assessment report of the Intergovernmental Panel on Climate Change.* Geneva, Switzerland: IPCC, 2014.

[3] F. Ackerman, E. A. Stanton *et al.*, *The cost of climate change: what we'll pay if global warming continues unchecked.* New York, NY, USA: Natural Resources Defense Council, 2007.

[4] M. A. Ross, "Integrated science assessment for particulate matter," *US Environmental Protection Agency*, pp. 61–161, 2009.

[5] W.-Y. Lin, M.-C. Hsiao, P.-C. Wu, J. S. Fu, L.-W. Lai, and H.-C. Lai, "Analysis of air quality and health co-benefits regarding electric vehicle promotion coupled

with power plant emissions," *Journal of Cleaner Production*, vol. 247, p. 119152, 2020.

[6] Y. Ding, Z. P. Cano, A. Yu, J. Lu, and Z. Chen, "Automotive li-ion batteries: current status and future perspectives," *Electrochemical Energy Reviews*, vol. 2, no. 1, pp. 1–28, 2019.

[7] R. Van Haaren, "Assessment of electric cars range requirements and usage patterns based on driving behavior recorded in the national household travel survey of 2009," *Earth and Environmental Engineering Department, Columbia University, Fu Foundation School of Engineering and Applied Science, New York*, vol. 51, p. 53, 2011.

[8] A. Emadi, *Advanced electric drive vehicles*. Boca Raton, FL, USA: CRC Press, 2014.

[9] W. E. Rippel, "Open delta motor drive with integrated recharge," U.S. Patent US 8,415,904, 1994.

[10] J. Reimers, L. Dorn-Gomba, C. Mak, and A. Emadi, "Automotive Traction Inverters: Current Status and Future Trends," *IEEE Transactions on Vehicular Technology*, vol. 68, no. 4, pp. 3337–3350, Apr. 2019.

[11] J. Reimers and A. Emadi, "Switched reluctance motor drive with three-phase integrated battery charger for electric vehicle applications," in *2019 IEEE 28th International Symposium on Industrial Electronics (ISIE)*, 2019, pp. 2097–2102.

[12] B. Bilgin, P. Magne, P. Malysz, Y. Yang, V. Pantelic, M. Preindl, A. Korobkine,

W. Jiang, M. Lawford, and A. Emadi, "Making the case for electrified transportation," *IEEE Transactions on Transportation Electrification*, vol. 1, no. 7, pp. 4–17, June 2015.

[13] K. Rajashekara, "Present status and future trends in electric vehicle propulsion technologies," *IEEE Journal of Emerging and Selected Topics in Power Electronics*, vol. 1, no. 1, pp. 3–10, 2013.

[14] H. Ye, Y. Yang, and A. Emadi, "Traction inverters in hybrid electric vehicles," in *2012 IEEE Transportation Electrification Conference and Expo (ITEC)*, June 2012, pp. 1–6.

[15] M. H. Rashid, *Power electronics handbook*. Oxford, United Kingdom: Butterworth-Heinemann, 2017.

[16] F. Z. Peng, "Z-source inverter," *IEEE Transactions on industry applications*, vol. 39, no. 2, pp. 504–510, 2003.

[17] E. P. Wiechmann, P. Aqueveque, R. Burgos, and J. Rodríguez, "On the efficiency of voltage source and current source inverters for high-power drives," *IEEE Transactions on Industrial Electronics*, vol. 55, no. 4, pp. 1771–1782, 2008.

[18] J. Rodriguez, J.-S. Lai, and F. Z. Peng, "Multilevel inverters: a survey of topologies, controls, and applications," *IEEE Transactions on Industrial Electronics*, vol. 49, no. 4, pp. 724–738, Aug. 2002.

[19] J. Rodriguez, S. Bernet, P. K. Steimer, and I. E. Lizama, "A survey on neutral-point-clamped inverters," *IEEE Transactions on Industrial Electronics*, vol. 57, no. 7, pp. 2219–2230, July 2010.

[20] M. Schweizer and J. W. Kolar, "Design and implementation of a highly efficient three-level T-type converter for low-voltage applications," *IEEE Transactions on Power Electronics*, vol. 28, no. 2, pp. 899–907, 2013.

[21] D. G. Holmes and T. A. Lipo, *Pulse width modulation for power converters: principles and practice*. John Wiley & Sons, 2003.

[22] A. Andersson, D. Lennström, and A. Nykänen, "Influence of inverter modulation strategy on electric drive efficiency and perceived sound quality," *IEEE Transactions on Transportation Electrification*, vol. 2, no. 1, pp. 24–35, 2016.

[23] I. P. Tsoumas and H. Tischmacher, "Influence of the inverter's modulation technique on the audible noise of electric motors," *IEEE Transactions on Industry Applications*, vol. 50, no. 1, pp. 269–278, 2014.

[24] A. Mehrizi-Sani and S. Filizadeh, "An optimized space vector modulation sequence for improved harmonic performance," *IEEE Transactions on Industrial Electronics*, vol. 56, no. 8, pp. 2894–2903, 2009.

[25] H. W. Van Der Broeck, H.-C. Skudelny, and G. V. Stanke, "Analysis and realization of a pulsewidth modulator based on voltage space vectors," *IEEE transactions on industry applications*, vol. 24, no. 1, pp. 142–150, 1988.

[26] A. Cataliotti, F. Genduso, A. Raciti, and G. R. Galluzzo, "Generalized PWM-VSI control algorithm based on a universal duty-cycle expression: Theoretical analysis, simulation results, and experimental validations," *IEEE Transactions on Industrial Electronics*, vol. 54, no. 3, pp. 1569–1580, 2007.

[27] S. Jurkovic, K. Rahman, B. Bae, N. Patel, and P. Savagian, "Next generation Chevy Volt electric machines; design, optimization and control for performance

and rare-earth mitigation," in *2015 IEEE Energy Conversion Congress and Exposition (ECCE)*, Sept. 2015, pp. 5219–5226.

[28] F. Momen, K. Rahman, Y. Son, and P. Savagian, "Electrical propulsion system design of Chevrolet Bolt battery electric vehicle," in *2016 IEEE Energy Conversion Congress and Exposition (ECCE)*, Sept. 2016, pp. 1–8.

[29] J. Holtz, W. Lotzkat, and A. Khambadkone, "On continuous control of pwm inverters in the overmodulation range including the six-step mode," in *Proceedings of the 1992 International Conference on Industrial Electronics, Control, Instrumentation, and Automation*, Nov. 1992, pp. 307–312 vol.1.

[30] N. Iwamuro and T. Laska, "IGBT history, state-of-the-art, and future prospects," *IEEE Transactions on Electron Devices*, vol. 64, no. 3, pp. 741–752, 2017.

[31] D. H. Ward, C. Iqbal, A. Carlos Volke, and M. Hornkamp, *Fundamentals of Semiconductors for Hybrid-Electric Powertrain.* Infineon Technologies North America Corp, 2013.

[32] L. Diao, J. Tang, P. C. Loh, S. Yin, L. Wang, and Z. Liu, "An efficient DSPFPGA-based implementation of hybrid PWM for electric rail traction induction motor control," *IEEE Transactions on Power Electronics*, vol. 33, no. 4, pp. 3276–3288, Apr. 2018.

[33] M. Lakka, E. Koutroulis, and A. Dollas, "Development of an FPGA-based SPWM generator for high switching frequency DC/AC inverters," *IEEE Transactions on Power Electronics*, vol. 29, no. 1, pp. 356–365, 2014.

[34] V. Smet, F. Forest, J. Huselstein, F. Richardeau, Z. Khatir, S. Lefebvre, and M. Berkani, "Ageing and failure modes of IGBT modules in high-temperature

power cycling," *IEEE Transactions on Industrial Electronics*, vol. 58, no. 10, pp. 4931–4941, Oct. 2011.

[35] Y. Yamada, Y. Takaku, Y. Yagi, I. Nakagawa, T. Atsumi, M. Shirai, I. Ohnuma, and K. Ishida, "Reliability of wire-bonding and solder joint for high temperature operation of power semiconductor device," *Microelectronics Reliability*, vol. 47, no. 12, pp. 2147–2151, 2007.

[36] A. D. Callegaro, J. Guo, M. Eull, B. Danen, J. Gibson, M. Preindl, B. Bilgin, and A. Emadi, "Bus bar design for high-power inverters," *IEEE Transactions on Power Electronics*, vol. 33, no. 3, pp. 2354–2367, 2018.

[37] M. Anwar, M. Hayes, A. Tata, M. Teimorzadeh, and T. Achatz, "Power dense and robust traction power inverter for the second-generation Chevrolet Volt extended-range EV," *SAE International Journal of Alternative Powertrains*, vol. 4, no. 2015-01-1201, pp. 145–152, 2015.

[38] M. Anwar, S. M. N. Hasan, M. Teimor, M. Korich, and M. B. Hayes, "Development of a power dense and environmentally robust traction power inverter for the second-generation Chevrolet VOLT extended-range EV," in *2015 IEEE Energy Conversion Congress and Exposition (ECCE)*, Sept. 2015, pp. 6006–6013.

[39] M. Anwar, M. Teimor, P. Savagian, R. Saito, and T. Matsuo, "Compact and high power inverter for the Cadillac CT6 rear wheel drive PHEV," in *2016 IEEE Energy Conversion Congress and Exposition (ECCE)*, Sept. 2016, pp. 1–7.

[40] A. Khan, T. Grewe, J. Liu, M. Anwar, A. Holmes, and R. Balsley, "The GM RWD PHEV propulsion system for the Cadillac CT6 luxury sedan," in *SAE 2016 World Congress and Exhibition*. SAE International, Apr. 2016.

[41] T. A. Burress, S. L. Campbell, C. L. Coomer, C. W. Ayers, A. A. Wereszczak, J. P. Cunningham, L. D. Marlino, L. E. Seiber, and H. T. Lin, "Evaluation of the 2010 Prius hybrid synergy drive system," Oak Ridge National Laboratory, Tech. Rep. ORNL/TM-2010/253, Jan. 2008.

[42] O. Kitazawa, T. Kikuchi, M. Nakashima, Y. Tomita, H. Kosugi, and T. Kaneko, "Development of power control unit for compact-class vehicle," *SAE International Journal of Alternative Powertrains*, vol. 5, pp. 278–285, 04 2016.

[43] Y. Sato, S. Ishikawa, T. Okubo, M. Abe, and K. Tamai, "Development of high response motor and inverter system for the Nissan LEAF electric vehicle," in *SAE 2011 World Congress & Exhibition*. SAE International, 04 2011.

[44] T. Burress. (2013) Benchmarking state-of-the-art technologies. Oak Ridge National Laboratory. [Online]. Available: http://energy.gov/sites/prod/files/2014/03/f13/ape006_burress_2013_o.pdf

[45] G. Moreno, K. Bennion, C. King, and S. Narumanchi, "Evaluation of performance and opportunities for improvements in automotive power electronics systems," in *2016 15th IEEE Intersociety Conference on Thermal and Thermomechanical Phenomena in Electronic Systems (ITherm)*, May 2016, pp. 185–192.

[46] M. Olszewski, "Oak ridge national laboratory annual progress report for the power electronics and electric machinery program," Oak Ridge National Laboratory (ORNL), Oak Ridge, TN, Tech. Rep., 2016.

[47] Roadmap E: full of energy! Volkswagen Group. [Online]. Available: https://www.volkswagenag.com/en/news/stories/2018/04/roadmap-e-full-of-energy.html

[48] R. Taylor, "Advanced strong hybrid and plug-in hybrid engineering evaluation and cost analysis," Munro and Associates Inc., Ricardo Strategic Consulting and ZMassociates Environmental Corp, Tech. Rep., Apr. 2017.

[49] R. J. Ramm, W. Liu, and C. Campbell, "Welding and soldering of transistor leads," U.S. Patent US14 557 381, 2014.

[50] R. J. Ramm, D. Sasaridis, C. Campbell, and W. Liu, "Busbar locating component," U.S. Patent US14 557 398, 2014.

[51] R. J. Ramm, W. Liu, and C. Campbell, "Heatsink with internal cavity for liquid cooling," U.S. Patent US14 286 670, 2014.

[52] R. J. Ramm, D. Sasaridis, C. Campbell, and W. Liu, "Planar capacitor terminals," U.S. Patent US14 557 256, 2014.

[53] E. Loveday. (2015) Tesla Modifies Horsepower Ratings For Dual Motor Model S. Inside EVs. [Online]. Available: https://insideevs.com/tesla-modifies-horsepower-ratings-dual-motor-model-s/

[54] "U.S. DRIVE Electrical and Electronics Technical Team Roadmap," U.S. Department of Energy, Oct. 2017.

[55] K. Hamada, "Present status and future prospects for electronics in EVs/HEVs and expectations for wide bandgap semiconductor devices," in *Materials Science Forum*, vol. 600. Trans Tech Publ, 2009, pp. 889–893.

[56] (2018) TM4 SUMO product brochure. TM4. [Online]. Available: https://www.tm4.com/wp-content/uploads/2018/08/TM4-SUMO-Product-Brochure.pdf

[57] Z. Wang, M. H. Mahmud, M. H. Uddin, B. McPherson, B. Sparkman, Y. Zhao, H. A. Mantooth, and J. R. Fraley, "A compact 250 kW silicon carbide MOSFET based three-level traction inverter for heavy equipment applications," *2018 IEEE Transportation Electrification Conference and Expo (ITEC)*, pp. 1129–1134, 2018.

[58] S. Bhattacharya, D. Mascarella, G. Joos, J.-M. Cyr, and J. Xu, "A dual three-level T-NPC inverter for high-power traction applications," *IEEE Journal of Emerging and Selected Topics in Power Electronics*, vol. 4, no. 2, pp. 668–678, June 2016.

[59] B. Singh, "Novel and ruggedized power electronics for off-highway vehicles," *IEEE Electrification Magazine*, vol. 2, no. 2, pp. 31–41, June 2014.

[60] US Department of Energy, "Wide bandgap semiconductors for power electronics technology assessment," *Quadrennial Technology Review*, 2015.

[61] J. Millan, P. Godignon, X. Perpina, A. Perez-Tomas, and J. Rebollo, "A survey of wide bandgap power semiconductor devices," *IEEE Transactions on Power Electronics*, vol. 29, no. 5, pp. 2155–2163, May 2014.

[62] A. Antonopoulos, H. Bangtsson, M. Alakula, and S. Manias, "Introducing a silicon carbide inverter for hybrid electric vehicles," in *2008 IEEE Power Electronics Specialists Conference*. IEEE, June 2008, pp. 1321–1325.

[63] V. Reber, "E-power: New possibilities with 800-volt charging," *Porsche Engineering Magazine*, no. 1, pp. 10–15, 2016. [Online]. Available: https://www.porscheengineering.com/peg/en/about/magazine/

[64] (2017, Oct.) Fisker Inc. chooses Ricardo to support integration of state-of-the-art 800V electric powertrain. [Online]. Available: https://d1v9sz08rbysvx.cloudfront.net/ricardo/media/media/other%20download%20files/fisker-ricardo-release-final-draft.pdf

[65] T. Ogawa, A. Tanida, T. Yamakawa, and M. Okamura, "Verification of fuel efficiency improvement by application of highly effective silicon carbide power semiconductor to HV inverter," in *SAE 2016 World Congress and Exhibition*, Apr. 2016.

[66] S. Yano, Y. Nakayama, H. Kobayashi, S. Hiramatsu, M. Yoshida, K. Onda, K. Hayashi, and K. Yamazaki, "Development of compact power control unit for HEVs," in *2017 IEEE Energy Conversion Congress and Exposition (ECCE)*, Oct. 2017, pp. 584–588.

[67] M. Eull, M. Preindl, and A. Emadi, "Analysis and design of a high efficiency, high power density three-phase silicon carbide inverter," in *2016 IEEE Transportation Electrification Conference and Expo (ITEC)*. IEEE, June 2016, pp. 1–6.

[68] J. Colmenares, D. Peftitsis, J. Rabkowski, D.-P. Sadik, G. Tolstoy, and H.-P. Nee, "High-efficiency 312-kVA three-phase inverter using parallel connection of silicon carbide MOSFET power modules," *IEEE Transactions on Industry Applications*, vol. 51, no. 6, pp. 4664–4676, Nov. 2015.

[69] J. Zhu, H. Kim, H. Chen, R. Erickson, and D. Maksimovi, "High efficiency sic traction inverter for electric vehicle applications," in *2018 IEEE Applied Power Electronics Conference and Exposition (APEC)*, Mar. 2018, pp. 1428–1433.

[70] J. Casady, K. Olejniczak, T. McNutt, D. Simco, B. Passmore, R. Shaw, D. Martin,

A. Curbow, B. Hull, and J. Palmour, "88 kilowatt automotive inverter with new 900 volt silicon carbide MOSFET technology," Cree, Inc., Fayetteville, AR (United States), Tech. Rep. DOE-Cree-0006920, Oct. 2017.

[71] F. Shang, A. P. Arribas, and M. Krishnamurthy, "A comprehensive evaluation of SiC devices in traction applications," *2014 IEEE Transportation Electrification Conference and Expo (ITEC)*, pp. 1–5, 2014.

[72] A. Morya, M. Moosavi, M. C. Gardner, and H. A. Toliyat, "Applications of wide bandgap (WBG) devices in AC electric drives: A technology status review," *2017 IEEE International Electric Machines and Drives Conference, IEMDC 2017*, 2017.

[73] D. Han, S. Li, W. Lee, and B. Sarlioglu, "Adoption of wide bandgap technology in hybrid/electric vehicles-opportunities and challenges," in *2017 IEEE Transportation Electrification Conference and Expo (ITEC)*, vol. 3. IEEE, June 2017, pp. 561–566.

[74] H. Zhang, L. M. Tolbert, and B. Ozpineci, "Impact of SiC devices on hybrid electric and plug-in hybrid electric vehicles," *IEEE Transactions on Industry Applications*, vol. 47, no. 2, pp. 912–921, March 2011.

[75] S. Das, L. D. Marlino, and K. O. Armstrong, "Wide bandgap semiconductor opportunities in power electronics," Oak Ridge National Lab.(ORNL), Oak Ridge, TN (United States), Tech. Rep. ORNL/TM-2017/702, 2018.

[76] M. Su, C. Chen, S. Sharma, and J. Kikuchi, "Performance and cost considerations for sic-based hev traction inverter systems," in *2015 IEEE 3rd Workshop on Wide Bandgap Power Devices and Applications (WiPDA)*, Nov. 2015, pp. 347–350.

[77] B. Ozpineci, M. S. Chinthavali, L. M. Tolbert, A. S. Kashyap, and H. A. Mantooth, "A 55-kw three-phase inverter with Si IGBTs and SiC schottky diodes," *IEEE Transactions on Industry Applications*, vol. 45, no. 1, pp. 278–285, 2009.

[78] L. Amber and K. Haddad, "Hybrid Si IGBT-SiC Schottky diode modules for medium to high power applications," in *2017 IEEE Applied Power Electronics Conference and Exposition (APEC)*, Mar. 2017, pp. 3027–3032.

[79] (2018) Tesla model 3 inverter with SiC power module from ST Microelectronics. SYSTEMPlus Consulting. [Online]. Available: http://www.systemplus.fr/wp-content/uploads/2018/06/SP18413-STMicroelectronics-SiC-Module-Tesla-Model3-Inverter_flyer-1.pdf

[80] K. Ohara, H. Masumoto, T. Takahashi, M. Matsumoto, and Y. Otsubo, "A new IGBT module with insulated metal baseplate (IMB) and 7th generation chips," in *Proceedings of PCIM Europe 2015; International Exhibition and Conference for Power Electronics, Intelligent Motion, Renewable Energy and Energy Management*, May 2015, pp. 1–4.

[81] Z. Liang, "Status and trend of automotive power packaging," in *2012 24th International Symposium on Power Semiconductor Devices and ICs*, June 2012, pp. 325–331.

[82] M. R. Atelge, "Power module packaging in automotive applications," Master's thesis, University of Waterloo, 2016.

[83] J. Steger, "A new generation of power modules with sinter-technology for the

automotive industry," in *2011 1st International Electric Drives Production Conference*, 2011, pp. 60–62.

[84] T. Geinzer, A. Schwarz, and M. Gleich, "Innovations for IGBT based power modules in HEV drivetrain applications," in *PCIM Europe 2017; International Exhibition and Conference for Power Electronics, Intelligent Motion, Renewable Energy and Energy Management; Proceedings of*, Nuremberg, Germany, May 2017, pp. 1–3.

[85] Y. Wang, Y. Li, X. Dai, S. Zhu, S. Jones, and G. Liu, "Thermal design of a dual sided cooled power semiconductor module for hybrid and electric vehicles," in *2017 IEEE Applied Power Electronics Conference and Exposition (APEC)*, 2017, pp. 3068–3071.

[86] T. Kimura, R. Saitou, K. Kubo, K. Nakatsu, H. Ishikawa, and K. Sasaki, "High-power-density inverter technology for hybrid and electric vehicle applications," *Hitachi Review*, vol. 63, no. 2, pp. 96–102, 2014.

[87] T. Tokuyama, K. Nakatsu, A. Nishihara, K. Sasaki, and R. Saito, "A novel direct water and double-sided cooled power module for HEV/EV inverter," *2014 International Conference on Electronics Packaging, ICEP 2014*, pp. 6–9, 2014.

[88] S. A. Rogers, "Annual progress report for the advanced power electronics and electric motors program," U.S. Department of Energy, Tech. Rep. DOE/EE-1040, Dec. 2013.

[89] M. Brubaker, D. El Hage, T. Hosking, E. Sawyer, and W. T. Franke, "Integrated DC link capacitor/bus enables a 20% increase in inverter efficiency," *PCIM Europe Conference Proceedings*, no. May, pp. 501–508, 2014.

[90] E. Sawyer, M. Brubaker, and T. Hosking, "Understanding the contribution of switch input connection geometry to overall DC link inductance," in *2015 17th European Conference on Power Electronics and Applications (EPE'15 ECCE-Europe)*, 2015, pp. 1–8.

[91] M. A. Brubaker, T. A. Hosking, T. Reiter, L. D. Marlino, and M. S. Chinthavali, "Optimized DC link for next generation power modules," in *PCIM Europe 2016; International Exhibition and Conference for Power Electronics, Intelligent Motion, Renewable Energy and Energy Management*, 2016, pp. 1–9.

[92] C. M. Barnes and P. E. Tuma, "Practical considerations relating to immersion cooling of power electronics in traction systems," *IEEE Transactions on Power Electronics*, vol. 25, no. 9, pp. 2478–2485, Sept. 2010.

[93] J. Broughton, V. Smet, R. R. Tummala, and Y. K. Joshi, "Review of thermal packaging technologies for automotive power electronics for traction purposes," *Journal of Electronic Packaging*, vol. 140, no. 4, p. 040801, 2018.

[94] Y. Lobsiger and J. W. Kolar, "Closed-loop di/ dt and dv/dt IGBT gate driver," *IEEE Transactions on Power Electronics*, vol. 30, no. 6, pp. 3402–3417, 2015.

[95] J. Chen and W. Ng, "Design trends in smart gate driver ICs for power MOSFETs and IGBTs," in *2017 IEEE 12th International Conference on ASIC (ASICON)*, 2017, pp. 112–115.

[96] N. Idir, R. Bausiere, and J. J. Franchaud, "Active gate voltage control of turn-on di/dt and turn-off dv/dt in insulated gate transistors," *IEEE Transactions on Power Electronics*, vol. 21, no. 4, pp. 849–855, 2006.

[97] Y. Zhou, L. Chen, S. Yang, F. Xu, and A. Khorshed, "A low cost gate driver with dynamic turn-off transient control for HEV/EV traction inverter application," *Conference Proceedings - IEEE Applied Power Electronics Conference and Exposition - APEC*, pp. 3200–3204, 2017.

[98] Y. Osanai, M. Wasekura, H. Yamawaki, and Y. Shindo, "IGBT gate control methods to reduce electrical power losses of hybrid vehicles," in *SAE 2016 World Congress and Exhibition*. SAE International, Apr. 2016.

[99] J.-M. Cyr, "Optimisation of IGBTs during the commutation process," TM4, Tech. Rep., 2015.

[100] H. Niu and R. D. Lorenz, "Sensing IGBT junction temperature using gate drive output transient properties," in *2015 IEEE Applied Power Electronics Conference and Exposition (APEC)*, 2015, pp. 2492–2499.

[101] D. Bortis, J. Biela, and J. W. Kolar, "Active gate control for current balancing of parallel-connected IGBT modules in solid-state modulators," *IEEE Transactions on Plasma Science*, vol. 36, no. 5, pp. 2632–2637, 2008.

[102] N. Sakurai and K. Yahata, "Gate driver integrated circuit for high-current and high-speed insulated-gate bipolar transistors used in hybrid electric vehicle and electric vehicle inverters," in *2017 IEEE 3rd International Future Energy Electronics Conference and ECCE Asia (IFEEC 2017 - ECCE Asia)*, 2017, pp. 947–952.

[103] B. Wang, M. Riva, J. D. Bakos, and A. Monti, "Integrated circuit implementation for a GaN HFET driver circuit," *IEEE Transactions on Industry Applications*, vol. 46, no. 5, pp. 2056–2067, 2010.

[104] Z. Wang, X. Shi, Y. Xue, L. M. Tolbert, F. Wang, and B. J. Blalock, "Design and performance evaluation of over current protection schemes for silicon carbide (SiC) power MOSFETs," *IEEE Transactions on Industrial Electronics*, vol. 61, no. 10, pp. 5570–5581, 2014.

[105] A. Rujas, V. López-Martín, L. Mir, and T. Nieva, "Gate driver for high power SiC modules. design considerations, development and experimental validation." *IET Power Electronics*, 2017.

[106] G. S. Inc., "Application brief:how to drive GaN enhancement mode HEMT," GaN Systems Inc., Tech. Rep. GN001, Apr. 2016.

[107] N. Fichtenbaum, M. Giandalia, S. Sharma, and J. Zhang, "Half-bridge gan power ICs: Performance and application," *IEEE Power Electronics Magazine*, vol. 4, no. 3, pp. 33–40, 2017.

[108] T. M. Jahns, "The past, present, and future of power electronics integration technology in motor drives," *CPSS Transactions on Power Electronics and Applications*, vol. 2, no. 3, pp. 197–216, Sept. 2017.

[109] Y. Burkhardt, A. Spagnolo, P. Lucas, M. Zavesky, and P. Brockerhoff, "Design and analysis of a highly integrated 9-phase drivetrain for EV applications," in *2014 International Conference on Electrical Machines (ICEM)*. IEEE, Sept. 2014, pp. 450–456.

[110] P. Brockerhoff, W. Schon, P. Blaha, P. Vaclavek, and Y. Burkhardt, "Disc inverter in highly integrated 9-phase drivetrain for E-mobility," in *2015 17th European Conference on Power Electronics and Applications (EPE'15 ECCE-Europe)*. IEEE, Sept. 2015, pp. 1–9.

[111] N. R. Brown, T. M. Jahns, and R. D. Lorenz, "Power converter design for an integrated modular motor drive," in *2007 IEEE Industry Applications Annual Meeting*. IEEE, Sept. 2007, pp. 1322–1328.

[112] J. Wang, Y. Li, and Y. Han, "Integrated modular motor drive design with GaN power FETs," *IEEE Transactions on Industry Applications*, vol. 51, no. 4, pp. 3198–3207, 2015.

[113] N. Sakr, D. Sadarnac, and A. Gascher, "A review of on-board integrated chargers for electric vehicles," in *2014 16th European Conference on Power Electronics and Applications*. IEEE, Aug. 2014, pp. 1–10.

[114] I. Subotic, N. Bodo, and E. Levi, "An EV drive-train with integrated fast charging capability," *IEEE Transactions on Power Electronics*, vol. 31, no. 2, pp. 1461–1471, Feb. 2016.

[115] S. Loudot, B. Briane, O. Ploix, and A. Villeneuve, "Fast charging device for an electric vehicle," U.S. Patent US12 919 396, 2010.

[116] A. Steier and A. Munday, "Advanced strong hybrid and plug-in hybrid engineering evaluation and cost analysis," California Air Resources Board, Tech. Rep., 2017.

[117] S. Das, "Life cycle assessment of carbon fiber-reinforced polymer composites," *The International Journal of Life Cycle Assessment*, vol. 16, no. 3, pp. 268–282, Mar. 2011.

[118] M. Pervaiz, S. Panthapulakkal, B. KC, M. Sain, and J. Tjong, "Emerging trends in automotive lightweighting through novel composite materials," *Materials Sciences and Applications*, vol. 07, no. 01, pp. 26–38, 2016.

[119] J. OKeeffe. (2012) Composite enclosures combine light weight with shielding effectiveness. TE Connectivity. [Online]. Available: http://www.te.com/content/dam/te-com/documents/aerospace-defense-and-marine/white-papers/okeefe-composite-enclosures-combine-light-weight-shielding.pdf

[120] I. Christou, A. Nelms, I. Cotton, and M. Husband, "Choice of optimal voltage for more electric aircraft wiring systems," *IET electrical systems in transportation*, vol. 1, no. 1, pp. 24–30, 2011.

[121] K. Olejniczak, T. McNutt, D. Simco, A. Wijenayake, T. Flint, B. Passmore, R. Shaw, D. Martin, A. Curbow, J. Casady *et al.*, "A 200 kVA electric vehicle traction drive inverter having enhanced performance over its entire operating region," in *2017 IEEE 5th Workshop on Wide Bandgap Power Devices and Applications (WiPDA)*. IEEE, 2017, pp. 335–341.

[122] A. D. Callegaro, B. Bilgin, and A. Emadi, "Radial force shaping for acoustic noise reduction in switched reluctance machines," *IEEE Transactions on Power Electronics*, vol. 34, no. 10, pp. 9866–9878, 2019.

[123] H. Li, B. Bilgin, and A. Emadi, "An improved torque sharing function for torque ripple reduction in switched reluctance machines," *IEEE Transactions on Power Electronics*, vol. 34, no. 2, pp. 1635–1644, 2018.

[124] E. W. Fairall, B. Bilgin, and A. Emadi, "State-of-the-art high-speed switched reluctance machines," in *2015 IEEE International Electric Machines & Drives Conference (IEMDC)*. IEEE, 2015, pp. 1621–1627.

[125] B. Burkhart, A. Klein-Hessling, I. Ralev, C. P. Weiss, and R. W. De Doncker, "Technology, research and applications of switched reluctance drives," *CPSS*

Transactions on Power Electronics and Applications, vol. 2, no. 1, pp. 12–27, 2017.

[126] B. Bilgin, B. Howey, A. D. Callegaro, J. Liang, M. Kordic, J. Taylor, and A. Emadi, "Making the case for switched reluctance motors for propulsion applications," *IEEE Transactions on Vehicular Technology*, 2020.

[127] M. Yilmaz and P. T. Krein, "Review of battery charger topologies, charging power levels, and infrastructure for plug-in electric and hybrid vehicles," *IEEE transactions on Power Electronics*, vol. 28, no. 5, pp. 2151–2169, 2012.

[128] A. Khaligh and M. D'Antonio, "Global trends in high-power on-board chargers for electric vehicles," *IEEE Transactions on Vehicular Technology*, vol. 68, no. 4, pp. 3306–3324, 2019.

[129] Y. Zhang, G. Yang, X. He, M. Elshaer, W. Perdikakis, H. Li, C. Yao, J. Wang, K. Zou, Z. Xu *et al.*, "Leakage current issue of non-isolated integrated chargers for electric vehicles," in *2018 IEEE Energy Conversion Congress and Exposition (ECCE)*. IEEE, 2018, pp. 1221–1227.

[130] S. Jeschke, M. Maarleveld, J. Bärenfänger, H. Hirsch, S. Tsiapenko, C. Waldera, and M. Obholz, "Development of a passive impedance network for modeling electric vehicle traction batteries for EMI measurements," in *2017 International Symposium on Electromagnetic Compatibility-EMC EUROPE*. IEEE, 2017, pp. 1–6.

[131] A. M. Hava and E. Ün, "Performance analysis of reduced common-mode voltage PWM methods and comparison with standard PWM methods for three-phase

voltage-source inverters," *IEEE Transactions on Power Electronics*, vol. 24, no. 1, pp. 241–252, 2009.

[132] F. Stubenrauch, N. Seliger, and D. Schmitt-Landsiedel, "Design and performance of a 200 kHz GaN motor inverter with sine wave filter," in *PCIM Europe 2017; International Exhibition and Conference for Power Electronics, Intelligent Motion, Renewable Energy and Energy Management*. VDE, 2017, pp. 1–9.

[133] F. Maislinger, H. Ertl, G. Stojcic, C. Lagler, and F. Holzner, "Design of a 100 kHz wide bandgap inverter for motor applications with active damped sine wave filter," *The Journal of Engineering*, vol. 2019, no. 17, pp. 3766–3771, 2019.

[134] I. Grobler and M. N. Gitau, "Analysis, modelling and measurement of the effects of aluminium and polymer heatsinks on conducted electromagnetic compatibility in DC-DC converters," *IET Science, Measurement & Technology*, vol. 11, no. 4, pp. 414–422, 2017.

[135] S. Wang, Y. Y. Maillet, F. Wang, D. Boroyevich, and R. Burgos, "Investigation of hybrid EMI filters for common-mode EMI suppression in a motor drive system," *IEEE Transactions on Power Electronics*, vol. 25, no. 4, pp. 1034–1045, 2009.

[136] Y. Zhang, W. Perdikakis, Y. Cong, X. Li, M. Elshaer, Y. Abdullah, J. Wang, K. Zou, Z. Xu, and C. Chen, "Leakage current mitigation of non-isolated integrated chargers for electric vehicles," in *2019 IEEE Energy Conversion Congress and Exposition (ECCE)*. IEEE, 2019, pp. 1195–1201.

[137] S. Haghbin, S. Lundmark, M. Alakula, and O. Carlson, "An isolated high-power integrated charger in electrified-vehicle applications," *IEEE Transactions on Vehicular Technology*, vol. 60, no. 9, pp. 4115–4126, 2011.

[138] "BMW i3 Cost Analysis Zone 4: Battery System," Munro & Associates, Nov. 2015.

[139] S. Q. Ali, D. Mascarella, and G. Joos, "Three Phase High Power Integrated Battery Charger for Plugin Electric Vehicles," *2015 IEEE Vehicle Power and Propulsion Conference (VPPC)*, no. October, pp. 1–6, 2015.

[140] L. De Sousa, B. Silvestre, and B. Bouchez, "A combined multiphase electric drive and fast battery charger for electric vehicles: Topology and electric propulsion efficency analysis," *2010 IEEE Vehicle Power and Propulsion Conference, VPPC 2010*, 2010.

[141] P. Dupuy, "Electric traction chain for an automobile," U.S. Patent US20 110 187 185A1, 2011.

[142] S. Haghbin and I. S. Guillen, "Integrated motor drive and non-isolated battery charger based on the torque cancelation in the motor," in *2013 IEEE 10th International Conference on Power Electronics and Drive Systems (PEDS)*. IEEE, apr 2013, pp. 824–829.

[143] C. Shi, Y. Tang, and A. Khaligh, "A three-phase integrated onboard charger for plug-in electric vehicles," *IEEE Transactions on Power Electronics*, vol. 33, no. 6, pp. 4716–4725, Jun. 2017.

[144] ——, "A single-phase integrated onboard battery charger using propulsion system for plug-in electric vehicles," *IEEE Transactions on Vehicular Technology*, vol. 66, no. 12, pp. 10 899–10 910, 2017.

[145] "Allcharge technology from continental makes evs fit for any type of

charging station," https://www.continental-corporation.com/en/press/press-releases/allcharge-technology-from-continental-makes-evs-fit-for-any-type-of-charging-station-63864, 2018, accessed: 2018-02-25.

[146] S. Lacroix, E. Laboure, and M. Hilairet, "An integrated fast battery charger for Electric Vehicle," in *2010 IEEE Vehicle Power and Propulsion Conference*. IEEE, sep 2010, pp. 1–6.

[147] A. P. Sandulescu, F. Meinguet, X. Kestelyn, E. Semail, and A. Bruyere, "Flux-weakening operation of open-end winding drive integrating a cost-effective high-power charger," *IET Electrical Systems in Transportation*, vol. 3, no. 1, pp. 10–21, March 2013.

[148] B. A. Welchko, T. A. Lipo, T. M. Jahns, and S. E. Schulz, "Fault tolerant three-phase ac motor drive topologies: a comparison of features, cost, and limitations," *IEEE Transactions on power electronics*, vol. 19, no. 4, pp. 1108–1116, 2004.

[149] S. Q. Ali, D. Mascarella, G. Joos, and L. Tan, "Torque elimination for integrated battery charger based on two permanent magnet synchronous motor drives for electric vehicles," *IET Electric Power Applications*, vol. 11, no. 9, pp. 1627–1635, 2017. [Online]. Available: http://digital-library.theiet.org/content/journals/10.1049/iet-epa.2017.0302

[150] I. Subotic, M. Jones, and E. Levi, "A fast on-board integrated battery charger for four-motor EVs," *Proceedings - 2014 International Conference on Electrical Machines, ICEM 2014*, pp. 2066–2072, 2014.

[151] "TM4 SUMO HD," https://www.tm4.com/products/direct-drive-electric-powertrain/sumo-hd/, 2018, accessed: 2018-02-25.

[152] I. Subotic, E. Levi, M. Jones, and D. Graovac, "Multiphase integrated on-board battery chargers for electrical vehicles," in *2013 15th European Conference on Power Electronics and Applications (EPE)*. IEEE, sep 2013, pp. 1–10.

[153] I. Subotic, N. Bodo, E. Levi, M. Jones, and V. Levi, "Isolated chargers for EVs incorporating six-phase machines," *IEEE Transactions on Industrial Electronics*, vol. 63, no. 1, pp. 653–664, 2016.

[154] M. S. Diab, A. A. Elserougi, A. S. Abdel-Khalik, A. M. Massoud, and S. Ahmed, "A Nine-Switch-Converter-Based Integrated Motor Drive and Battery Charger System for EVs Using Symmetrical Six-Phase Machines," *IEEE Transactions on Industrial Electronics*, vol. 63, no. 9, pp. 5326–5335, sep 2016. [Online]. Available: http://ieeexplore.ieee.org/document/7454736/

[155] I. Subotic, E. Levi, M. Jones, and D. Graovac, "On-board integrated battery chargers for electric vehicles using nine-phase machines," *Proceedings of the 2013 IEEE International Electric Machines and Drives Conference, IEMDC 2013*, no. May, pp. 226–233, 2013.

[156] I. Subotic, N. Bodo, E. Levi, and M. Jones, "Onboard Integrated Battery Charger for EVs Using an Asymmetrical Nine-Phase Machine," *IEEE Transactions on Industrial Electronics*, vol. 62, no. 5, pp. 3285–3295, may 2015.

[157] N. Bodo, E. Levi, I. Subotic, J. Espina, L. Empringham, and C. M. Johnson, "Efficiency Evaluation of Fully Integrated On-Board EV Battery Chargers With Nine-Phase Machines," *IEEE Transactions on Energy Conversion*, vol. 32, no. 1, pp. 257–266, 2017.

[158] V. Katic, I. Subotic, N. Bodo, E. Levi, B. Dumnic, and D. Milicevic, "Overview of

fast on-board integrated battery chargers for electric vehicles based on multiphase machines and power electronics," *IET Electric Power Applications*, vol. 10, no. 3, pp. 217–229, mar 2016.

[159] Hung-Chun Chang and Chang-Ming Liaw, "Development of a Compact Switched-Reluctance Motor Drive for EV Propulsion With Voltage-Boosting and PFC Charging Capabilities," *IEEE Transactions on Vehicular Technology*, vol. 58, no. 7, pp. 3198–3215, sep 2009. [Online]. Available: http://ieeexplore.ieee.org/document/4801662/

[160] Y. Hu, C. Gan, W. Cao, C. Li, and S. Finney, "Split Converter-Fed SRM Drive for Flexible Charging in EV/HEV Applications," *IEEE Transactions on Industrial Electronics*, vol. 62, no. 10, pp. 6085–6095, Apr. 2015.

[161] N. Hatti, S. Nuilers, N. Chayopitak, and P. Somsiri, "An integrated battery charger configuration for SRM drive in electric motorcycles," *IEEJ Transactions on Electrical and Electronic Engineering*, vol. 13, no. 2, pp. 295–302, feb 2018. [Online]. Available: http://doi.wiley.com/10.1002/tee.22526

[162] Y. Hu, C. Gan, W. Cao, C. Li, and S. Finney, "Split Converter-Fed SRM Drive for Flexible Charging in EV/HEV Applications," *IEEE Transactions on Industrial Electronics*, vol. 62, no. 10, pp. 6085–6095, 2015.

[163] Yihua Hu, Xueguan Song, Wenping Cao, and Bing Ji, "New SR Drive With Integrated Charging Capacity for Plug-In Hybrid Electric Vehicles (PHEVs)," *IEEE Transactions on Industrial Electronics*, vol. 61, no. 10, pp. 5722–5731, oct 2014. [Online]. Available: http://ieeexplore.ieee.org/document/6732911/

[164] A. Deriszadeh and R. Bojoi, "An integrated battery-charger for switched reluctance motor drives," in *2017 6th International Conference on Clean Electrical Power (ICCEP)*. IEEE, jun 2017, pp. 446–451.

[165] A. Rashidi, M. M. Namazi, S. Saghaian-nezhad, D. Lee, and J. Ahn, "Zero torque control of switched reluctance motors for charging reactor of electric vehicles," in *2015 IEEE International Conference on Advanced Intelligent Mechatronics (AIM)*, vol. 2. IEEE, jul 2015, pp. 990–995.

[166] N. Sakr, A. Fernandez Sanchez, D. Sadarnac, and A. Gascher, "A combined switched reluctance motor drive and battery charger for electric vehicles," in *IECON 2015 - 41st Annual Conference of the IEEE Industrial Electronics Society*, Nov. 2015.

[167] R. W. Erickson and D. Maksimovic, *Fundamentals of power electronics*. Springer Science & Business Media, 2007.

[168] P. C. Krause, O. Wasynczuk, S. D. Sudhoff, and S. Pekarek, *Analysis of electric machinery and drive systems*. Wiley Online Library, 2002, vol. 2.

[169] Plexim GmbH. Zürich, Switzerland, "PLECS User Manual," 2019.

[170] L. De Sousa and H. Dogan, "Method of evaluating the zero-sequence inductance ratio for electrical machines," in *Proceedings of the 2011 14th European Conference on Power Electronics and Applications*. IEEE, 2011, pp. 1–10.

[171] B. Bilgin, J. W. Jiang, and A. Emadi, *Switched Reluctance Motor Drives: Fundamentals to Applications*. CRC Press, 2018.

[172] A. Rashidi, M. M. Namazi, S. M. Saghaian-Nezhad, D. H. Lee, and J.-W. Ahn, "PFC and zero torque control of SRM drive for EV battery charging," in *2016 IEEE Transportation Electrification Conference and Expo, Asia-Pacific (ITEC Asia-Pacific)*, June 2016.

[173] A. Rashidi, M. M. Namazi, S. M. Saghaian-Nezhad, D. H. Lee, and J.-W. Ahn, "An optimized simple current sharing function of SRM with intrgrated battery charger for EV drive," in *2016 IEEE Transportation Electrification Conference and Expo, Asia-Pacific (ITEC Asia-Pacific)*, June 2016.

[174] J. Liang, G. Xu, B. Wang, J. Bao, and H. Wang, "A novel integrated switched reluctance motor drive with bi-directional inverter," in *2014 IEEE International Conference on Industrial Technology (ICIT)*, Feb. 2014.

[175] Y. Hu, C. Gan, Q. Sun, P. Li, J. Wu, and H. Wen, "Modular Tri-Port High-Power Converter for SRM Based Plug-in Hybrid Electrical Trucks," *IEEE Transactions on Power Electronics*, vol. 33, no. 4, pp. 3247–3257, Apr. 2018.

[176] S. Nikam and B. Fernandes, "Design of soft magnetic composite based modular four phase SRM for electric vehicle application," in *2014 International Conference on Electrical Machines (ICEM)*. IEEE, 2014, pp. 112–116.

[177] C. Chan, K. Chau *et al.*, *Modern electric vehicle technology*. Oxford University Press on Demand, 2001, no. 47.

[178] S. Wang, Q. Zhan, Z. Ma, and L. Zhou, "Implementation of a 50-kW four-phase switched reluctance motor drive system for hybrid electric vehicle," *IEEE Transactions on Magnetics*, vol. 41, no. 1, pp. 501–504, 2005.

[179] R. Krishnan, *Switched reluctance motor drives: modeling, simulation, analysis, design, and applications*. CRC press, 2001.

[180] "IEEE Recommended Practice and Requirements for Harmonic Control in Electric Power Systems," *IEEE Std 519-2014 (Revision of IEEE Std 519-1992)*, pp. 1–29, June 2014.

[181] C. L. Fortescue, "Method of symmetrical co-ordinates applied to the solution of polyphase networks," *Transactions of the American Institute of Electrical Engineers*, vol. 37, no. 2, pp. 1027–1140, 1918.

[182] C. B. Jacobina, M. B. De Rossiter Corrêa, T. M. Oliveira, A. M. N. Lima, and E. R. C. Da Silva, "Current control of unbalanced electrical systems," *IEEE Transactions on Industrial Electronics*, vol. 48, no. 3, pp. 517–525, 2001.

[183] Yongsug Suh, V. Tijeras, and T. Lipo, "A control method in dq synchronous frame for PWM boost rectifier under generalized unbalanced operating conditions," in *2002 IEEE 33rd Annual IEEE Power Electronics Specialists Conference. Proceedings (Cat. No.02CH37289)*. IEEE, 2002, pp. 1425–1430.

[184] O. Ojo and Zhiqiao Wu, "A new controller for three-phase boost rectifiers lacking balance in source voltages and impedances," in *Twentieth Annual IEEE Applied Power Electronics Conference and Exposition, 2005. APEC 2005.*, vol. 1. IEEE, 2005, pp. 508–514.

[185] P. Xiao, K. A. Corzine, and G. K. Venayagamoorthy, "Cancellation predictive control for three-phase pwm rectifiers under harmonic and unbalanced input conditions," in *IECON 2006 - 32nd Annual Conference on IEEE Industrial Electronics*, 2006, pp. 1816–1821.

[186] Y. Suh and T. A. Lipo, "Control scheme in hybrid synchronous stationary frame for PWM ac/dc converter under generalized unbalanced operating conditions," *IEEE Transactions on Industry Applications*, vol. 42, no. 3, pp. 825–835, 2006.

[187] A. V. Stankovic and K. Chen, "A new control method for input-output harmonic elimination of the PWM boost-type rectifier under extreme unbalanced operating conditions," *IEEE Transactions on Industrial Electronics*, vol. 56, no. 7, pp. 2420–2430, 2009.

[188] Z. Li, Y. Li, P. Wang, H. Zhu, C. Liu, and W. Xu, "Control of three-phase boost-type pwm rectifier in stationary frame under unbalanced input voltage," *IEEE Transactions on Power Electronics*, vol. 25, no. 10, pp. 2521–2530, 2010.

[189] M. Mirhosseini, J. Pou, B. Karanayil, and V. G. Agelidis, "Positive- and negative-sequence control of grid-connected photovoltaic systems under unbalanced voltage conditions," in *2013 Australasian Universities Power Engineering Conference (AUPEC)*, vol. 32, no. 9. IEEE, sep 2013, pp. 1–6.

[190] D. Perez-Estevez, J. Doval-Gandoy, A. G. Yepes, and O. Lopez, "Positive- and Negative-Sequence Current Controller With Direct Discrete-Time Pole Placement for Grid-Tied Converters With LCL Filter," *IEEE Transactions on Power Electronics*, vol. 32, no. 9, pp. 7207–7221, sep 2017.

[191] M. Mirhosseini, J. Pou, and V. G. Agelidis, "Current improvement of a grid-connected photovoltaic system under unbalanced voltage conditions," in *2013 IEEE ECCE Asia Downunder*, June 2013, pp. 66–72.

[192] D. Tracy. (2019) An Extremely Detailed Look At The Porsche Taycan's Engineering Designed To Take On Tesla. Jalopnik. [Online]. Available: https://jalopnik.com/an-extremely-detailed-look-at-the-porsche-taycans-engin-1837802533

[193] I. Subotic, N. Bodo, E. Levi, and M. Jones, "Onboard Integrated Battery Charger for EVs Using an Asymmetrical Nine-Phase Machine," *IEEE Transactions on Industrial Electronics*, vol. 62, no. 5, pp. 3285–3295, May 2015.

[194] I. Subotic, N. Bodo, and E. Levi, "Integration of Six-Phase EV Drivetrains Into Battery Charging Process With Direct Grid Connection," *IEEE Transactions on Energy Conversion*, vol. 32, no. 3, pp. 1012–1022, Sep. 2017.

[195] B. Bahrani, A. Rufer, S. Kenzelmann, and L. A. Lopes, "Vector control of single-phase voltage-source converters based on fictive-axis emulation," *IEEE Transactions on Industry Applications*, vol. 47, no. 2, pp. 831–840, Mar./Apr. 2010.

[196] F. Blaabjerg, *Control of Power Electronic Converters and Systems: Volume 2*. Academic Press, 2018, vol. 2.

[197] R. Prasad, C. Namuduri, and P. Kollmeyer, "Onboard unidirectional automotive G2V battery charger using sine charging and its effect on li-ion batteries," in *2015 IEEE Energy Conversion Congress and Exposition (ECCE)*, Sep. 2015, pp. 6299–6305.

[198] E. B. Joffe and K.-S. Lock, *Grounds for grounding: A circuit to system handbook*. John Wiley & Sons, 2011.

[199] J. W.-T. Fan, R. S.-C. Yeung, and H. S.-H. Chung, "Optimized hybrid PWM

scheme for mitigating zero-crossing distortion in totem-pole bridgeless PFC," *IEEE Transactions on Power Electronics*, vol. 34, no. 1, pp. 928–942, 2018.